AGU PUBLICATIONS

JGR

Journal of Geophysical Research: Space Physics

RESEARCH ARTICLE
10.1002/2013JA019748

This article is a companion to *Manchester et al.* [2014] doi:10.1002/2014JA019882.

Key Points:
- The interactions are studied between geospace and a solar filament
- Cold dense plasma sheet forms from filament material stretching magnetotail
- Creates anomalous features including superfountain and expanded auroral oval

Correspondence to:
J. U. Kozyra,
jukozyra@umich.edu

Citation:
Kozyra, J. U., et al. (2014), Solar filament impact on 21 January 2005: Geospace consequences, *J. Geophys. Res. Space Physics*, *119*, 5401–5448, doi:10.1002/2013JA019748.

Received 3 JAN 2014
Accepted 5 MAY 2014
Accepted article online 7 JUN 2014
Published online 9 JUL 2014

Solar filament impact on 21 January 2005: Geospace consequences

J. U. Kozyra[1], M. W. Liemohn[1], C. Cattell[2], D. De Zeeuw[1], C. P. Escoubet[3], D. S. Evans[4], X. Fang[5], M.-C. Fok[6], H. U. Frey[7], W. D. Gonzalez[8], M. Hairston[9], R. Heelis[9], G. Lu[10], W. B. Manchester IV[1], S. Mende[7], L. J. Paxton[11], L. Rastaetter[12], A. Ridley[1], M. Sandanger[13], F. Soraas[13], T. Sotirelis[11], M. W. Thomsen[14], B. T. Tsurutani[15], and O. Verkhoglyadova[15]

[1]AOSS Department, University of Michigan, Ann Arbor, Michigan, USA, [2]School of Physics and Astronomy, University of Minnesota, Minneapolis, Minnesota, USA, [3]ESA, Noordwijk, Netherlands, [4]Boulder, Colorado, USA, [5]LASP, University of Colorado Boulder, Boulder, Colorado, USA, [6]NASA Goddard Space Flight Center, Greenbelt, Maryland, USA, [7]Space Sciences Laboratory, University of California, Berkeley, California, USA, [8]INPE, Sao Jose Dos Campos, Brazil, [9]William B. Hanson Center for Space Sciences, University of Texas at Dallas, Richardson, Texas, USA, [10]High Altitude Observatory, Boulder, Colorado, USA, [11]Applied Physics Laboratory, Johns Hopkins University, Laurel, Maryland, USA, [12]Community Coordinated Modeling Center, GSFC, Greenbelt, Maryland, USA, [13]Birkeland Centre for Space Science, Department of Physics and Technology, University of Bergen, Bergen, Norway, [14]Los Alamos National Laboratory, Los Alamos, New Mexico, USA, [15]Jet Propulsion Laboratory, Pasadena, California, USA

Abstract On 21 January 2005, a moderate magnetic storm produced a number of anomalous features, some seen more typically during superstorms. The aim of this study is to establish the differences in the space environment from what we expect (and normally observe) for a storm of this intensity, which make it behave in some ways like a superstorm. The storm was driven by one of the fastest interplanetary coronal mass ejections in solar cycle 23, containing a piece of the dense erupting solar filament material. The momentum of the massive solar filament caused it to push its way through the flux rope as the interplanetary coronal mass ejection decelerated moving toward 1 AU creating the appearance of an eroded flux rope (see companion paper by Manchester et al. (2014)) and, in this case, limiting the intensity of the resulting geomagnetic storm. On impact, the solar filament further disrupted the partial ring current shielding in existence at the time, creating a brief superfountain in the equatorial ionosphere—an unusual occurrence for a moderate storm. Within 1 h after impact, a cold dense plasma sheet (CDPS) formed out of the filament material. As the interplanetary magnetic field (IMF) rotated from obliquely to more purely northward, the magnetotail transformed from an open to a closed configuration and the CDPS evolved from warmer to cooler temperatures. Plasma sheet densities reached tens per cubic centimeter along the flanks—high enough to inflate the magnetotail in the simulation under northward IMF conditions despite the cool temperatures. Observational evidence for this stretching was provided by a corresponding expansion and intensification of both the auroral oval and ring current precipitation zones linked to magnetotail stretching by field line curvature scattering. Strong Joule heating in the cusps, a by-product of the CDPS formation process, contributed to an equatorward neutral wind surge that reached low latitudes within 1–2 h and intensified the equatorial ionization anomaly. Understanding the geospace consequences of extremes in density and pressure is important because some of the largest and most damaging space weather events ever observed contained similar intervals of dense solar material.

1. Introduction

On 21 January 2005, one of the fastest interplanetary coronal mass ejections (ICMEs) of solar cycle 23 containing dense plasma directly behind the sheath region struck the Earth and produced a variety of unusual effects in the Earth's magnetosphere and ionosphere, some seen previously only during superstorms. The January 2005 storm was a relatively modest event with minimum $Dst \sim -100$ nT, whereas superstorms are the most extreme of geomagnetic disturbances with $Dst \leq -240$ nT [*Tsurutani et al.*, 1992; *Mac-Mahon and Gonzalez*, 1997; *Bell et al.*, 1997; *Echer et al.*, 2008]. The major challenge for the present investigation is to establish the differences in the space environment between this storm and other moderate storms, which make this storm behave in some ways like a superstorm and in other ways like a moderate event. What do these departures from what we expect (and normally observe) tell us about the way the geospace system works? Following the trail required to find the answers to these questions led to the investigation of the linked effects of extreme dynamic pressure (and density) from the Sun to the Earth.

As we will show, the dense material following immediately behind the sheath in the ICME was directly or indirectly responsible for most of the unusual features in the storm. This dense material was a piece of the erupting solar filament identified on the basis of its enhanced He^{+}/He^{2+} composition ratio and cool temperatures [*Kozyra et al.*, 2013] and was in an unexpected position in the ICME following directly behind the sheath, a position different from its location when it lifted off the Sun. The remarkable processes responsible for the redistribution of the filament material within the ICME are outlined in *Kozyra et al.* [2013] and presented in detail in a companion to the present paper by *Manchester et al.* [2014].

To briefly summarize, the dense material of the solar filament produced significant changes in the ICME structure before arrival at Earth. In the simulation, as the ICME decelerated moving toward Earth, the momentum of the dense filament material, originally at the back (sunward edge) of the flux rope, caused it to push its way forward toward the nose. A portion of the filament material pushed so far forward that it came into direct contact with the sheath material leading the ICME. Diverging nonradial flows developed around the filament, which transported azimuthal flux from the front of the filament to the sides of the ICME. At the same time, magnetic field lines at the nose of the ICME reconnected with the interplanetary magnetic field (IMF), peeling away the outer layer and creating a region of opened field lines trailing behind. However, during the short propagation time, only 7% of the azimuthal magnetic flux was lost by reconnection, so the vast majority of the flux imbalance in front of the filament was due to divergent flows. This transport process offers an additional mechanism to explain flux rope erosion, which is particularly applicable to fast CMEs.

Observations at 1 AU provide compelling evidence that the processes in the simulation of the fast ICME actually occurred during the 21 January 2005 event [*Manchester et al.*, 2014]. The reconnection between northward IMF in the sheath and the southward IMF in the ICME predicted by the simulation was, in fact, observed by the Cluster satellite on 21 January 2005 in the solar wind upstream of the Earth [*Munoz et al.*, 2010]. Dense filament material was found directly behind the sheath region, and the azimuthal flux was entirely unbalanced in the flux rope with a much shorter interval of southward IMF at the leading edge than northward IMF in the remaining portion of the flux rope. Evidence in the strahl electrons indicates a topological change in the flux rope consistent with a remnant flux rope followed by opened field lines. This imbalance in the direction of the azimuthal flux was likely responsible for limiting the intensity of the magnetic storm that developed.

In this paper, we explore the linkages between the eroded flux rope, the dense filament material, and the unusual features in geospace that developed. Even before its arrival, the solar filament drove changes in the space environment that would not be expected in association with a moderate magnetic storm. The interplanetary (IP) shock at the leading edge of the ICME was exceptionally strong. It reached magnetosonic Mach 5.4 [*Du et al.*, 2008] when even values above Mach 4.0 are rare, and typical values at 1 AU are 1.0–3.0 [cf. *Tsurutani and Lin*, 1985]. High velocities are required at 1 AU to produce such strong shocks. In this case, based on the simulation described in *Manchester et al.* [2014], the high initial velocity of the ICME was almost certainly sustained by the momentum of the massive solar filament as it moved through the background heliosphere. Such a scenario is also consistent with the diverging flows ahead of the filament material.

The strong shock initiated exceptionally intense auroral activity in which *AL* dropped below −2000 nT, eventually reaching −3200 nT before recovering (see Figure 3h). In 3.5 years of uncalibrated *AE* data from 2002 to the middle of 2005, there were only 11 cases of *AL* below −2000 nT [*Yamauchi et al.*, 2006]. Nine of these events were preceded by >15 min of southward IMF during which presumably energy was stored in the magnetotail to later power the intense substorm. In the remaining two, there was no apparent preconditioning of the magnetotail. The 21 January 2005 activity was one of these two events. Auroral activity of this intensity is extremely rare with characteristics that differ significantly from typical substorms [*Miyashita et al.*, 2005; *Rosenqvist et al.*, 2005; *Yamauchi et al.*, 2006]. *Du et al.* [2011] focused on a particular auroral feature during this extreme auroral activity (a dawn-dusk aligned polar cap arc at ~85°–90° magnetic latitude (MLAT)), which they propose to be associated with activity at the distant X line in the magnetotail.

An exceptionally strong spectral peak was reported in the IMF at ultra low frequencies (3–4 mHz) [*Potapov and Polyushkina*, 2010]. The direct entry of these ULF waves into the magnetosphere was inferred from the simultaneous presence of 1–5 mHz discrete spectral peaks in the geosynchronous magnetic field. ULF waves

are known to interact with radiation belt electrons enhancing radial diffusion and thus contributing to adiabatic acceleration as well as to losses at the dayside magnetopause [*Schulz and Lanzerotti*, 1974; *Hudson et al.*, 2000; *Elkington et al.*, 2003].

In the hour following the strong IP shock, detached auroras were observed in the dayside, duskside, and nightside subauroral regions attributed to high-energy ion precipitation [*Zhang et al.*, 2008]. The IMF was northward at the time of shock arrival but rapidly rotated southward initiating a relativistic electron flux dropout event. Within less than an hour, >2 MeV electron fluxes at GOES 10 and GOES 12 had decreased by 3 orders of magnitude [*Clilverd et al.*, 2006, 2007]. An integrated view of precipitation observed by ground-based instruments and on balloons presented by these authors suggests that approximately 10% of the drop in the geosynchronous flux in the first 10 min resulted from precipitation into the atmosphere. Over the course of the next 2.7 h, an estimated half of the > 2 MeV outer belt electrons were lost to the atmosphere. This event was one of the first to offer compelling evidence that a significant fraction of radiation belt particles are actually lost to the atmosphere during a flux dropout event. Bursts of high-energy precipitation associated with both the IP shock impact and the filament arrival created enhancements in electrical conductivity and associated weakening of the electric fields in the stratosphere observed by MINIS balloons [*Kokorowski et al.*, 2008] demonstrating direct linkages between the solar filament and regions as low in altitude as the middle atmosphere.

Intervals of extreme downward Poynting flux in the cusp region were reported in observations by the DMSP satellites during this event, physically linked to high-latitude reconnection under conditions of strong IMF B_y in *Li et al.* [2011] and *Knipp et al.* [2011]. These fluxes (and simulated Joule heating rates at the same locations) reached more than 100 mW/m^2 at the time of the extreme auroral activity mentioned previously and again during the interaction with the dense filament under northward IMF conditions. These are comparable to rates found in superstorms, where for reference, typical values during moderate magnetic storms reach only 50 mW/m^2 [*Gary et al.*, 1995]. However, as we will show in section 5.2.1, the maximum Joule heating rates in the simulation occurred during the short interval of southward IMF and strong IMF B_y at the leading edge of the solar filament, reaching values as high as 174 mW/m^2. No DMSP satellites were traversing the cusp regions at this time [*Li et al.*, 2011] and so they missed observing the peak values predicted by the simulation. The strong IMF B_y, high solar wind speed, and large dynamic pressures of the solar filament combined to amplify Joule heating rates to these extreme levels. We will show that the ~2 h spike in Joule heating associated with the shock, sheath, and leading edge of the solar filament triggered a massive equatorward neutral wind surge with effects on equatorial electrodynamics discussed in section 6.2.2.

The expansion of the neutral upper atmosphere was also exceptional compared to other magnetic storms. The 21 January 2005 storm contained several examples of a recently identified class of unpredicted satellite drag events associated with regions near the dayside cusp [*Lühr et al.*, 2004; *Rentz and Lühr*, 2008]. However, even among events of this nature, the 21 January 2005 magnetic storm was unusual. The neutral thermosphere at middle-to-low latitudes expanded more relative to the strength of the merging electric field (storm energy input) than during any other storm in 2001–2005, an interval which included a number of superstorms [*Liu et al.*, 2011]. Questions have been raised about the relative roles of Joule heating and low-energy electron precipitation in producing the unexpected level of thermospheric expansion in these types of events [*Lühr et al.*, 2004; *Schlegel et al.*, 2005; *Liu et al.*, 2005a; *Clemmons et al.*, 2008; *Sadler et al.*, 2012]. In the present study, we find an extended region of soft electron precipitation just equatorward of the cusp and spanning from dawn to dusk during the northward IMF interval of the solar filament discussed in section 5.2.2. The origins of this region are not investigated here but its presence may explain the unusual efficiency of the atmospheric expansion relative to the strength of the merging electric field in this event.

Finally, the interaction with the shock and driving solar filament had a significant effect on the equatorial ionosphere. Prompt penetration electric fields (PPEF) began to lift the equatorial *F*2 layer immediately at the first shock impact, and an *F*3 layer developed rising to more than 1200 km altitude [*Zong et al.*, 2010; *Sahai et al.*, 2011; *Santos et al.*, 2012] (an indicator of an enhanced equatorial fountain [*Paznukhov et al.*, 2007]). Later in the storm, an unusual intensification of the equatorial ionization anomaly (EIA) was reported by *Santos et al.* [2012] in observations from the Latin American sector and by *Sahai et al.* [2011] in observations from the South American sector and global total electron content (TEC). We will show that despite equal or higher levels of magnetic activity, similar development of the EIA crests was not observed in the few days prior to 21 January but only developed in concert with the solar filament. We explore the underlying mechanisms.

The ring current continued to grow during the northward IMF interval following the arrival of the solar filament [*Du et al.*, 2008]. Ring current growth has so far not been associated with northward IMF conditions. Lack of space does not permit a discussion of our investigation into the mechanisms responsible here, but this issue is treated along with a larger set of unusual signatures associated with the development of the ring current, plasma convection, ionospheric outflows, cusp ion recirculation, the delayed build up of the ring current oxygen component, and a strong low-latitude ion-atom aurora in a separate paper.

In this paper, we focus on a set of phenomena linked directly to the high pressures (and densities) in the solar filament, including an equatorial superfountain, a cold dense plasma sheet (CDPS) in the magnetosphere formed from the dense filament material, strong magnetotail stretching due to the diamagnetism of the CDPS, a persistent expansion of the discrete auroral regions to as far equatorward as 55° MLAT, and an intensification and equatorward movement of the ring current precipitation regions. Interestingly enough, the last four of these phenomena occurred during northward IMF conditions usually associated with magnetic quieting.

The aims of this paper are several. The first is to examine in detail the development of a CDPS under extremes in solar wind density and speed by combining observations with a fully coupled global modeling suite including MHD magnetosphere, inner magnetosphere, and ionospheric electrodynamics models. This represents an enhancement over recent simulations of the CDPS development [*Li et al.*, 2005, 2008, 2011] which did not include self-consistent calculation of the inner magnetospheric drift physics. The second is to combine all of these observations with those already reported and with the global models to investigate the features in geospace that developed, the linkages between them, and their connections to the solar filament.

To explore the coupling within the system, we follow the chain of events from Sun to geospace, tracing the effects of events in one sphere (heliosphere, magnetosphere, ionosphere, and atmosphere) on the other spheres. Following the linkages throughout the system is dependent on detailed knowledge of the individual components. This synoptic approach rather than being independent of focused process studies actually completes them by demonstrating how these processes interact within the global system, and feeds back to ask new questions that further increase our knowledge about the components that compose the interconnections. The synoptic investigation of extreme events has emerged as an important research area in other scientific disciplines, most notably meteorology and climate sciences, leading to new insights into global conditions that produce extreme weather and climate [cf. *Peterson et al.*, 2012, 2013]. A similar need to understand extreme space weather drives the selection of methodologies here. There is developing recognition that an integrated approach involving multiple discipline areas is required for progress.

The study reported here involves multiple instruments on 18 different satellites, ground-based instruments, and three interlinked global models. The location and orbits of satellites and the portions of the Sun-Earth system covered by ground-based instruments represent a particular configuration of the Heliophysics System Observatory, which will be described in section 2. Details of the instruments and observations will be given as data sets are introduced in the discussion of specific features. Section 3 provides details of the global models and inputs. Section 4 gives an integrated view of the solar wind and geospace conditions on 21–22 January 2005 by combining observations and model outputs and identifies some of the key coupling issues. Section 5 goes into more detail to understand the formation of two intervals of CDPS—one warm and the other cooler—the configuration of the magnetotail in each case, and the magnetotail stretching that accompanied their formation. Section 6 examines the processes responsible for the unusual features observed during this storm and the connections between them. Section 7 provides a summary and conclusions and briefly explores implications.

2. The Configuration of the Heliophysics System Observatory and Collaborating Programs

Twelve magnetospheric and interplanetary satellites contributed information on the solar wind inputs and the magnetospheric responses. These include (1) the Advanced Composition Explorer (ACE) [*Gloeckler et al.*, 1998; *Stone et al.*, 1998], (2) the four Cluster satellites [*Escoubet et al.*, 2001], (3) the Chinese Double Star TC-1 satellite [*Liu et al.*, 2005b; *Reme et al.*, 2005], (4) the Imager for Magnetopause-to-Aurora Global Exploration (IMAGE) satellite [*Burch*, 2000; *Mitchell et al.*, 2000; *Mende et al.*, 2000], and (5) five geosynchronous satellites from Los Alamos National Laboratory (LANL-94, 97A, 90, 01A, and 02A) in different local time planes [*Bame et al.*,

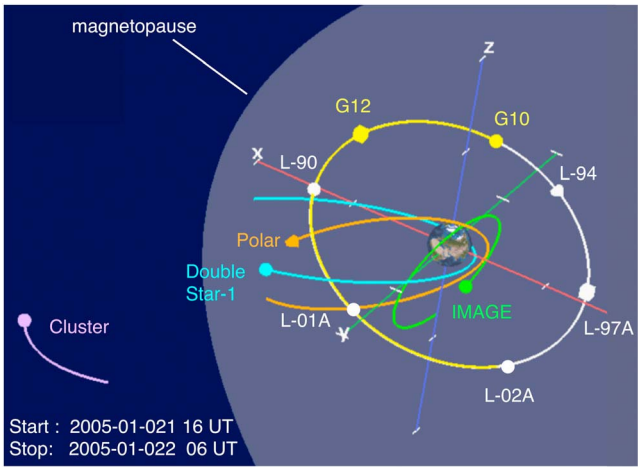

Figure 1. The configuration of the magnetospheric satellites in the Heliophysics System Observatory during the time interval from 16 UT on 21 January to 06 UT on 22 January 2005 is given in GSE coordinates. The symbols mark the start of the time interval.

1993; *Thomsen et al.*, 1997]. The ACE satellite was located at an (*X*, *Y*, *Z*) of (221.96 R_E, −35.02 R_E, 21.52 R_E) GSE and (221.96 R_E, −38.29 R_E, 14.97 R_E) GSM upstream of the Earth at the Lagrangian L1 point monitoring solar wind conditions. The Cluster satellites were just upstream of the Earth's bow shock at $X \sim 14.7$ R_E acting as very close solar wind monitors as the interplanetary shock leading the ICME struck the Earth. Figure 1 shows the configuration of magnetospheric satellites in the Heliophysics System Observatory with the addition of the Chinese Double Star TC-1 satellite. Solid lines show the orbit of each satellite from 21 January 16:00 UT to 22 January 06:00 UT while the symbol indicates the position of each satellite at the start of this interval. Though Polar observations are not used in this paper, they were utilized as part of the broader study of this unusual event and so the Polar orbit is included in the plot for completeness.

Nine low-altitude satellites contributed information on the propagation of effects into the ionosphere and atmosphere. These include (1) the Thermosphere, Ionosphere, Mesosphere Energetics and Dynamics (TIMED) mission [*Paxton et al.*, 1999, 2004; *Christensen et al.*, 2003], (2) the Defense Meteorological Satellites Program (DMSP) satellites F13, F14, F15, F16 [*Hardy et al.*, 1984; *Rich and Hairston*, 1994; *Hairston et al.*, 1998], (3) the NOAA Polar Orbiting Environment Sensors (POES) (N15, N16, N17) [*Evans and Greer*, 2000], and (4) the Fast Auroral Snapshot Explorer (FAST) [*Carlson et al.*, 1998, 2001]. Figure 2 shows the magnetic local time planes of each of these satellite orbits. More details about the instruments will be presented as the data sets are introduced below.

3. Global Models

The suite of global models being used in this effort was developed at the Center for Space Environment Modeling (CSEM) at the University of Michigan and was run for this study both at the University of Michigan and at the Community Coordinated Modeling Center (CCMC) at Goddard Space Flight Center. The Space Weather Modeling Framework (SWMF) [*Tóth et al.*, 2005, 2012] links these large-scale models together and, in doing so, enables exploration of coupling and feedback processes that are multiscale and nonlinear.

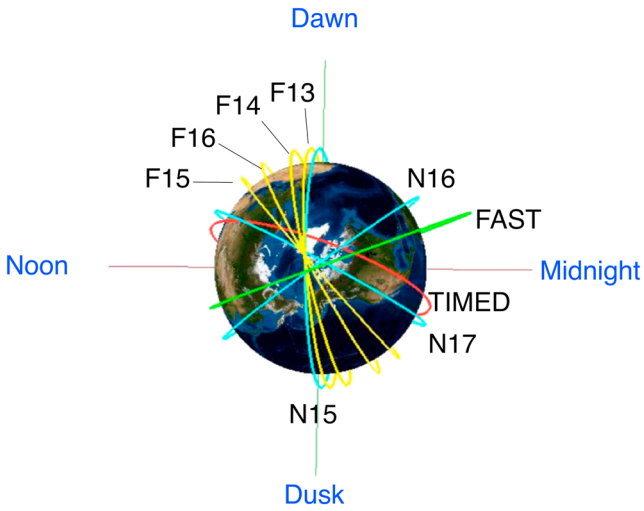

Figure 2. Local time planes of low-altitude polar-orbiting satellites on 21 January 2005. These include DMSP F13, F14, F15, and F16 (yellow lines), NOAA-N15, N16, and N17 (blue lines), FAST (green), and TIMED (red).

The three models used in the study are the Block-Adaptive-Tree Solar-Wind Roe-Type Upwind Scheme (BATS-R-US) MHD model of the global magnetosphere, an inner magnetosphere model based on the Rice Convection Model (RCM), and an Ionospheric Electrodynamics (IE) solver. The version of the BATS-R-US model used here treats the plasma as a single fluid transported in the cross-*B* direction by

$E \times B$ drift [*Powell et al.*, 1999; *De Zeeuw et al.*, 2000; *Gombosi et al.*, 2002]. The plasma is described as an ideal gas with infinite electrical conductivity, which means that the plasma is in effect stuck to individual magnetic field lines. Since gradient and curvature drifts in the inner magnetosphere are energy and velocity dependent and can be faster than the $E \times B$ drifts in this region, the 1–200 keV ions and electrons that are the main pressure-bearing populations in this region are not well described in global MHD models.

To remedy this, the drift physics of the energetic particles in the inner magnetosphere is added using a module based on the RCM [*De Zeeuw et al.*, 2004]. The RCM solves the equations of motion for plasma in the inner and middle magnetosphere coupled with current conservation in the ionosphere [cf. *Wolf*, 1983; *Toffoletto et al.*, 2003]. The particle distribution is represented by a large number (~100) of isotropic "fluids" that are each advected by a combination of gradient, curvature, and $E \times B$ drifts. Because the gradient and curvature drifts are divergent, currents develop that flow along magnetic fields lines into and out of the ionosphere. Ionospheric conductance, which is a combination of a time-dependent solar EUV-produced component and an auroral enhancement that varies directly with precipitation and field-aligned currents (FACs), is supplied to the RCM by the Ionospheric Electrodynamics (IE) module [*Ridley and Liemohn*, 2002; *Ridley et al.*, 2004]. As FACs close through the ionosphere, electric fields are produced that map back into the inner magnetosphere along field lines assumed to be equipotentials. The electric fields self-consistently modify the particle drifts to include an additional $E \times B$ component in the hot plasma transport equations.

The technical details of the coupling between the BATS-R-US and RCM are described by *De Zeeuw et al.* [2004]. In brief, the BATS-R-US model supplies the RCM with bulk plasma parameters and the potential distribution at the outer edge of the RCM domain along with the magnetic field configuration inside. The RCM returns a "corrected" plasma pressure within the inner magnetosphere, which is used to nudge the MHD solution with a relaxation time that is typically set to 100 s.

The ionosphere is represented by a two-dimensional layer with prescribed finite Pedersen (ΣP) and Hall (ΣH) conductances. Electrodynamic coupling to the ionosphere is added by the IE module, which solves for the two-dimensional electrostatic potential using FACs from the BATS-R-US model. The IE module passes electric potentials back to BATS-R-US, which are applied as the transverse $E \times B$ drift at the inner boundary.

With the combination of all three models, the physical processes of interest in this study are well represented. For example, studies have confirmed that global MHD models reproduce well the magnetic field configuration and its dynamical response to solar wind conditions, the position of boundaries, plasma regions like the lobes and plasma sheet, the strength of magnetopause, cross-tail, region 1, and NBZ currents, convection patterns under northward and southward IMF conditions, and the open-closed field line boundary projected to the ionosphere [cf. *Janhunen and Palmroth*, 2001]. The formations of cold dense plasma sheets under northward IMF conditions have been represented in MHD simulations with timing and duration in agreement with observations [cf. *Li et al.*, 2005, 2008]. The RCM enables a realistic simulation of region 2 currents, undershielding, and overshielding of the inner magnetosphere from convection electric fields and of self-consistent potential patterns in the inner magnetosphere. The coupled RCM and MHD codes produce observational features not well represented in the MHD model alone, including stronger region 2 currents, partial shielding of the inner magnetosphere from convection electric fields during southward IMF conditions [*De Zeeuw et al.*, 2004], and the location and evolution of the open-closed magnetic field line boundary [*Rae et al.*, 2010].

The simulations used in the present study were downloaded directly from CCMC's model archive. They were originally run for an ionospheric study and are here integrated with observations into a synoptic analysis of the entire geospace response to the solar filament impact. Simulations used two different configurations of the SWMF. The first included the drift physics of the inner magnetosphere by coupling the BATS-R-US MHD model with the RCM, the second used the BATS-R-US MHD model alone, all else being the same (both runs included IE coupling). For ease of discussion, these will be referred to as the MHD + RCM and MHD-only simulations, respectively. A comparison of these two simulations gives information on the ring current contribution to the magnetospheric response and the effects of drift physics in the inner magnetosphere on the development and characteristics of the CDPS. Simulation outputs at a 10 min cadence in the magnetosphere and a 1 min cadence in the ionosphere are stored in the CCMC archive under the identifiers Derek_Andeweg_111608_1 and Derek_Andeweg_111608_2, respectively. These simulations were subsequently regenerated with a 1 min cadence in the magnetospheric output files

to examine the rapid variations during the ICME sheath passage. The higher cadence magnetospheric outputs for the MHD + RCM run and the MHD-only run are available upon request from CCMC.

There are two simplifications used in these runs that should be noted. First, the IMF B_x was set to zero. To test the consequences of this assumption, two identical simulations were run using the MHD + RCM configuration in SWMF, one with IMF B_x from ACE and the other with IMF B_x set to zero. Only small differences developed in the simulated *SYM-H* values by the end of the ring current development. Though these small changes are interesting, we conclude that IMF B_x does not have a major effect on the global response.

Second, an underlying assumption in the RCM is that ions have isotropic pitch angle distributions and thus are distributed uniformly along magnetic flux tubes. Because of this assumption, identical ionospheres in the Northern and Southern Hemispheres are required. As a default, CCMC provides the RCM with the Northern Hemisphere ionosphere and the assumption is made that both ionospheres are identical. This will affect the off-equatorial ring current pressure distribution fed into the MHD model. Since the ring current pressure is maximum in the equatorial plane, we assume the off-equatorial effects are small compared to the global-scale behavior and rely on comparison to satellite observations to determine whether or not this assumption is valid after the fact. Note that the ionospheres in the Northern and Southern Hemispheres are not required to be the same in the MHD model and, in fact, include full seasonal effects.

Solar wind conditions were taken from the ACE spacecraft and then propagated in the BATS-R-US MHD model to the magnetopause. At the time of shock arrival, Cluster was located at 14.7 R_E just upstream of the Earth's bow shock. The shock arrived at Cluster at ~17:10 UT and the filament arrived at ~18:44 UT [*Dandouras et al.*, 2009]. The shock in the simulation was delayed approximately 6 min compared to the observed shock at Cluster, arriving at 17:16 UT model time. We shift the model time by 6 min to agree with the shock arrival at Cluster such that $\mathrm{UT} = \mathrm{UT}_{\mathrm{model}} - 6$ min. By using a single time shift, we have an accurate adjustment for the arrival of the shock but subsequent data points may still be displaced in time a small amount. By the time of the largest southward IMF values within the ICME sheath region, no significant shift in model versus actual UT was observed.

4. Overview of Solar Wind Inputs and Global Geospace Responses

On 20 January 2005, one of the fastest coronal mass ejections of solar cycle 23 lifted off the west limb of the Sun and was observed at the ACE spacecraft upstream of Earth just 34 h later [cf. *Pohjolainen et al.*, 2007; *Foullon et al.*, 2007]. As discussed in the introduction, the high-density material entrained in the ICME was subsequently identified as solar filament material [*Kozyra et al.*, 2013; *Manchester et al.*, 2014]. Regions 1–3 in Figure 3 refer to the sheath region, remnant flux rope, and opened outer layer of the initially larger flux rope, respectively (described in *Manchester et al.* [2014]). The vertical dashed line (labeled SA) marks the arrival at Earth of the shock leading the ICME and SB the discontinuity at the leading edge of the filament material. These labels are consistent with *Foullon et al.* [2007] to make it easier to compare to their detailed analysis of the solar wind parameters.

Figure 3 shows 1 min averages of the following solar wind parameters: (a) IMF clock angle, (b) IMF B_y GSM (nT), (c) IMF B_z GSM (nT), and (d) solar wind proton density (cm^{-3}). These quantities were observed by the ACE spacecraft at the L1 position upstream of the Earth and propagated to the calculated position of the Earth's bow shock normal in the OMNI database at http://omniweb.gsfc.nasa.gov/. The ACE observations after 00:40 UT on 22 January were reprocessed to compensate for increased background due to a solar particle event using the search mode data, which has a temporal resolution of 33 min (courtesy of R. Skoug and H. Elliott, 2005). These reprocessed data were propagated from ACE to 10 R_E using the observed solar wind V_x. There are a number of unusual aspects to the solar wind observations that are essential to understanding the geospace conditions that followed.

Between vertical lines SA and SB is a sheath region of compressed and heated solar wind plasma swept up in front of the ICME on its way to Earth, shown in Figure 3d. Figure 3c displays the north–south component of the interplanetary magnetic field (IMF) in the GSM (geocentric solar magnetospheric) coordinate system, which has proven to be the most appropriate for relating IMF components to their magnetospheric and ionospheric effects [*Russell and McPherron*, 1973]. The compressed southward IMF in the sheath region on 21 January reached −28 nT (red shading in Figure 3c). This value is comparable to the southward IMF that drives superstorms but, in this case, it lasted for just 20 min so the storm reached only moderate intensity.

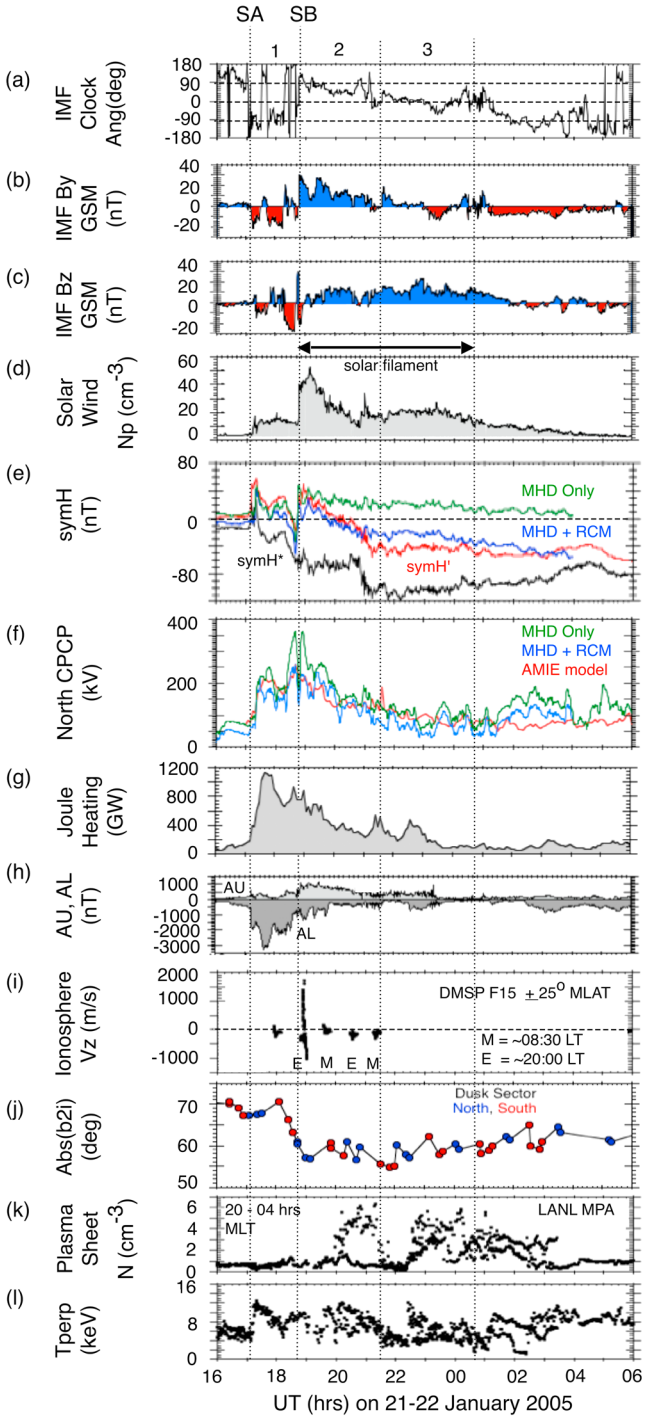

Figure 3. Solar and magnetospheric parameters during the time interval from 16 UT on 21 January to 06 UT on 22 January 2005. Vertical lines SA and SB mark the shock and solar filament arrivals, respectively. Regions 1, 2, and 3 mark the time intervals associated with the sheath region, the remnant flux rope, and the opened outer layer of the flux rope as discussed in a companion paper by *Manchester et al.* [2014].

The vertical dotted line labeled SB at ~ 18:45 UT marks the arrival of the solar filament. Note that the filament material appears directly following the ICME sheath. Densities reached values greater than 50 cm^{-3} and peak dynamic pressure exceeded 60 nPa [*Foullon et al.*, 2007]. The northward IMF interval in the remnant flux rope (region 2) had a substantial IMF B_y component (Figure 3b) but this component became weak or zero in region 3 which marks the opened field lines trailing the remnant flux rope (Figure 3c). In this last region, the plasma still retains the characteristics of the larger coherent flux rope though the filament densities drop substantially as the plasma moves outward to fill the larger accessible volume of space. Figure 3a shows the IMF clock angle $\theta = \text{atan}\,(B_y/B_z)$ in GSM coordinates. Due northward corresponds to $\theta = 0°$, due southward to $\theta = \pm 180°$, due eastward to $\theta = +90°$, and due westward to $\theta = -90°$. As will be shown later, the abrupt transition from obliquely to purely northward IMF between regions 2 and 3 was important to the topology of the magnetotail, driving a transition from an open to closed magnetotail and from a warmer to cooler CDPS.

The solar filament created many unusual features in the ongoing geomagnetic storm. A global overview of geospace conditions is given in Figures 3e–3l. As the solar filament struck the magnetosphere just after 18:45 UT, the strong southward IMF and steep solar wind density rise at its leading edge produced an abrupt change in the flow of energetic particles within the magnetosphere, disrupting further the partial shielding that existed at the time. In this interval, electric fields of solar wind origin (called prompt penetration electric fields [cf. *Kelley et al.*, 1979]) increased in strength, enhancing upward ion drifts in the equatorial ionosphere. Two DMSP satellites reached the equatorial ionosphere just after the solar filament material hit. Figure 3i is a plot of low-latitude vertical ion drifts observed in the ionosphere by DMSP F15 over ± 25° MLAT. At 18:54 UT, DMSP F15 observed strong kilometer/second upward vertical ion drifts. This is a signature of prompt penetration electric fields and marks a further breakdown in shielding of the inner magnetosphere and underlying ionosphere by the ring current.

This breakdown in shielding is usually seen only for major magnetic storms and is surprising in association with the more modest 21 January 2005 storm event.

The cross-polar cap potential (CPCP) in Figure 3f is an important global measure of the energy coupling between the magnetosphere and the solar wind. The observed CPCP was provided by the assimilative mapping of ionospheric electrodynamics (AMIE) technique [*Richmond and Kamide*, 1988] utilizing data from the DMSP F13 and F15 satellites, NOAA-15, 16, and 17 satellites, the SuperDARN radar network, and 188 ground magnetometers. There are two peaks in the CPCP that correspond to the two strong intervals of southward IMF, one in the ICME sheath and one at the leading edge of the solar filament (shown in Panel c). The CPCP drops but remains elevated as the IMF turns obliquely northward in association with the filament. This indicates that, although the IMF is northward, substantial energy is still entering geospace from the solar wind because of the large IMF B_y. The CPCP drops to its lowest values, as one would expect, when the IMF rotates due northward in the trailing portion of the ICME. The calculated CPCP values from the MHD-only (green line) and the MHD + RCM (blue line) simulations are also plotted. The MHD-only simulation overpredicts the CPCP peak values by up to 100 kV, while the MHD + RCM simulation is in remarkable agreement with the observations. This agreement provides confirmation that the MHD + RCM simulation is correctly reproducing the basic energetics of the solar wind-magnetosphere coupling for this event.

Figure 3g displays the Joule heating derived using the AMIE procedure. Joule heating is calculated from $\Sigma_P[E^2 + (\delta e)^2]$, where the height-integrated Pedersen conductance Σ_P is obtained by assimilating precipitating particle data from DMSP and NOAA satellites into the empirical conductance model of *Fuller-Rowell and Evans* [1987], E is the AMIE estimated electric field, and δe is the error associated with the estimated large-scale electric field E from AMIE. More information can be found in *Lu et al.* [1996]. The AMIE procedure does not take into account neutral wind effect, which can increase or decrease the Joule heating rate depending on the orientation between the winds and ion drifts [cf. *Lu et al.*, 1995].

The very large initial peak in Joule heating near 17:40 UT is associated with the extreme auroral activity discussed in the introduction during which the *AL* drops to values more negative than −3000 nT. The second Joule heating peak near 18:40 UT is associated with the strongest southward IMF of the storm in the trailing edge of the ICME sheath. The third peak, which is comparable in magnitude to the second, occurs during the short interval of southward IMF at the leading edge of the solar filament near 19:00 UT as solar wind dynamic pressure rises. Since the DMSP satellites used in the construction of the Joule heating rates did not cross through the cusp region but skirted it on the dawnside or duskside, the contribution of the cusps to the Joule heating rates produced by the AMIE model is likely to be underestimated, which may change the relative strengths of these three peaks. The MHD + RCM simulation discussed in section 5.2.1 below indicates that maximum Joule heating rates actually occurred at the leading edge of the solar filament. The burst of Joule heating represented by the three peaks was responsible for generating a neutral wind surge linked to an intensification of the equatorial anomaly crests later in the storm. The relative contributions of these three Joule heating peaks to the neutral wind surge on the dayside depend on the local time distribution of the Joule heating (examples shown in Figure 7). The connection between this spike in Joule heating and unusual features in the equatorial electrodynamics is discussed further in section 6.2.2.

Figures 3k and 3l give the nightside geosynchronous plasma sheet densities and temperatures, respectively, observed by the Los Alamos Magnetospheric Plasma Analyzers (MPA) [*Bame et al.*, 1993] on satellites L-90, L-94, L-97A, L-01A, and L-02A. Observations from all satellites within the 20:00 to 04:00 magnetic local time (MLT) window are plotted at a given UT. MPA measures ion and electron fluxes from 1 eV/q to 45 keV/q in 40 logarithmically spaced channels. Moments of density and temperature shown here are derived for hot ions (>100 eV) [*Thomsen et al.*, 1997]. Note MPA does not distinguish ion mass so density calculations assume that all ions are protons. This means that the ion density, given in Figure 3k, will be underestimated by a factor of the sqrt(m_i/m_p), where m_p is the proton mass, if a significant fraction of heavy ions with mass m_i are present. Temperatures, given in Figure 3l, will not be affected by the presence of a heavy ion component. As the IMF turned obliquely northward at 19:00 UT (see clock angles in Figure 3a), the capture of solar filament material into the magnetosphere began. Within 1 h by 20:00 UT, a CDPS appeared at geosynchronous orbit on the nightside formed from the filament material.

The CDPS is a different state than the *superdense* plasma sheets originally discovered in observations at geosynchronous orbit [*Borovsky et al.*, 1997, 1998]. The superdense plasma sheet with density in excess of

2 cm^{-3} has a temperature not significantly different from typical values. Its presence is correlated with high density in the solar wind during southward IMF conditions. Increased plasma sheet density reaches the nightside at geosynchronous orbit with a delay of 2 h from the arrival of dense solar wind at the magnetopause and sweeps around the inner magnetosphere to the dayside in about 8 h time.

In contrast, a CDPS builds in the outer magnetosphere during northward IMF conditions [cf. *Fujimoto et al.*, 2000, 2002, 2005; *Phan et al.*, 2000; *Nishino et al.*, 2002; *Welling and Ridley*, 2010]. Densities increase first on the dayside just inside the magnetopause, reaching values approaching the magnetosheath densities within tens of minutes [*Li et al.*, 2005]. The flank low-latitude boundary layer (LLBL) becomes denser and thicker and feeds the plasma sheet on the nightside from the flanks inward, building a magnetotail CDPS on a timescale of ~3 h. The CDPS is not seen at geosynchronous orbit unless the IMF immediately turns strongly southward triggering a magnetic storm or the magnetosphere is compressed by high solar wind dynamic pressure [*Thomsen et al.*, 2003; *Lavraud et al.*, 2005] as is the case during 21 January 2005.

Conditions during the 21 January 2005 magnetic storm allow a detailed examination of the differences between the CDPS during obliquely northward compared to due northward IMF conditions. When the IMF is obliquely northward from 20:00 to 21:30 UT, a warm ($Ti \sim 8.5$ keV) superdense (maximum $n \sim 4.5$–6 cm^{-3}) plasma sheet is seen at geosynchronous orbit. This is still cool compared to typical plasma sheets under southward IMF conditions. However, when the IMF turns more purely northward between 22:40 on 21 January and 01:10 UT the next day, the plasma sheet becomes still cooler (~6 keV or 7×10^7 K) but remains superdense (maximum $n \sim 4$–5.5 cm^{-3}). In contrast, typical temperatures at geosynchronous orbit reach 20 keV and densities are 0.5–1.5 cm^{-3} [*Borovsky et al.*, 1998]. We refer here to the CDPS during obliquely northward conditions as a warm dense plasma sheet (WDPS) and during more purely northward conditions as a CDPS to call attention to this difference in temperature, which is also clearly seen in the simulation (see section 5.5 below).

In between the time of the WDPS and the CDPS, geosynchronous satellites observed a region of extremely low density from ~21:20 UT to ~22:20 UT, which we identify as an excursion into the magnetotail lobe. This entry into the lobes implies that the magnetic field lines have been distorted due to strong stretching of the magnetotail [cf. *Thomsen et al.*, 1994]. One way to test this suggestion is through the time variations in the so-called b2i boundary [*Newell et al.*, 1998] plotted in Figure 3j. The b2i boundary is believed to mark the location where the magnetic field topology transitions from dipolar to stretched. In response to this change in magnetic field topology, the tens of keV proton pitch angle distribution observed in low-Earth orbit transitions from isotropic with a filled loss cone (due to scattering in the stretched magnetotail) to anisotropic with a nearly empty loss cone in the more dipolar fields of the inner magnetosphere [*Sergeev et al.*, 1983, 1993]. Just poleward of this boundary, locally mirroring and precipitating ion fluxes reach a peak. The peak in the energy flux of precipitating 3 keV ions observed by DMSP is used in an automated identification of the isotropy boundary (b2i) [*Newell et al.*, 1998].

During the 21 January storm, the b2i boundary moved inward to 55° MLAT, indicative of increased magnetotail stretching, beginning at 21:20 UT at the same time that LANL geosynchronous satellites entered the magnetotail lobe on the nightside. Even though the LANL satellites remained in the lobe until ~22:20 UT, there was an apparent movement of the b2i boundary 5° poleward at 21:05 UT and then an abrupt drop to continue a more gradual recovery to higher MLATs. To understand this behavior, spectrograms of flux versus ion energy and UT were used to manually locate the b2i boundaries during this interval. The three Southern Hemisphere (red) data points after 21:20 UT were taken from different DMSP satellites (F13, F16, and F15, respectively, in order of increasing time) at increasing MLTs from ~18 to 20 h. The same for the three Northern Hemisphere (blue) data points after 22:05. However, during this entire time interval, exceptionally strong precipitating ion fluxes used in calculating b2i were observed with broad flat peaks in intensity covered 5°–6° MLAT. The entire region of intense precipitating ion flux shifted equatorward after 21:20 UT and then began retreating poleward again after 22:04 UT. Changes in the MLAT selected as the peak very likely resulted from variations in the overall shape of the broad flat flux peak rather than a true major poleward shift in the isotropy boundary.

Figure 3h displays the *AU* and *AL* indices, which are a direct measurement of the maximum current in the eastward and westward auroral electrojets, respectively, taken at magnetometer stations between 60° and 70° geomagnetic latitude [cf. *Kamide and Akasofu*, 1983; *Kamide and Rostoker*, 2004]. They are thus representative of the level of activity in the auroral oval when the electrojets are within this band of geomagnetic latitudes. Enhancements in *AL* are generally taken to indicate auroral substorm activity; while enhancements in *AU*

relate to increases in magnetospheric convection. *AL* reached exceptionally high values in association with the interplanetary shock and the sheath region ahead of the ICME. *AU* was relatively weak in this time interval but became elevated in association with the rise in dynamic pressure with the solar filament. However, both *AU* and *AL* reached their lowest absolute values at the time of strong magnetotail stretching indicated by the low-latitude location of the b2i boundary. This is unusual since strong stretching is normally associated with high geomagnetic activity.

Finally, the *SYM-H* index is plotted in Figure 3e. The *SYM-H* index is constructed from the average of the *H* component of the geomagnetic field observed at six midlatitude stations after a quiet time baseline is removed [*Iyemori*, 1990]. *SYM-H* gives information on the energy in the symmetric ring current as does *Dst* [cf. *Dessler and Parker*, 1959; *Sckopke*, 1966] but at a 1 min cadence as opposed to the 1 h resolution of the *Dst* index [cf. *Wanliss and Showalter*, 2006; *Katus and Liemohn*, 2013]. During magnetic storms, the *SYM-H* index is believed to be dominated by the ring current contribution and thus is used to monitor the ring current development and to provide a measure of the severity of a magnetic storm. However, there are also contributions from magnetic fields generated by magnetopause, field-aligned and magnetotail currents, as well as induced currents in the solid Earth. Comprehensive reviews of these other contributions are given by *McPherron* [1997] and *Gonzalez et al.* [1994].

To extract information about the ring current evolution and the storm severity, the *SYM-H* index is typically corrected to remove contributions from other current systems. The *SYM-H* index corrected for only the effects of the induced currents in the solid Earth and for the quiet time ring current is given by *SYM-H*′ (red line in Figure 3e). *SYM-H*′ can be directly compared to simulation outputs which naturally include the complete set of magnetospheric currents. *SYM-H** (black line) is the observed *SYM-H*′ with an additional correction to remove the time-dependent contributions of enhanced magnetopause currents produced by high solar wind dynamic pressure. These two forms of the *SYM-H* index are given by

$$SYM\text{-}H' = (SYM\text{-}H + c)/1.3$$
$$SYM\text{-}H^* = \left(SYM\text{-}H - b^* V_{sw}{}^* \mathrm{sqrt}\left(N_p\right) + c\right)/1.3$$

where N_p is the solar wind proton density in cm^{-3}, V_{sw} is the solar wind speed in km/s, b is a proportionality factor, and c is the contribution of the quiet time ring current. In the present work, we use $b = 0.2\ \mathrm{nT/(eV\,cm^{-3})^{1/2}}$ and $c = 20$ nT [cf. *Burton et al.*, 1975; *Gonzalez et al.*, 1994]. The factor 1.3 removes contributions from the diamagnetic Earth [*Dessler and Parker*, 1959; *Langel and Estes*, 1985].

There are two sudden impulses (SIs) observable in the *SYM-H* indices, the first at the shock arrival (17:11 UT) and the second at the filament arrival (~18:45 UT). The ring current builds during three separate intervals. The first two are associated with strong southward IMF intervals in the sheath region ahead of the ICME and are each followed by partial recoveries of the ring current as the IMF rotates northward. The last is associated with the compression and then expansion of the magnetosphere by a strong spike in dynamic pressure at ~21:00 UT during northward IMF conditions. In all cases, the time lag between the arrival of a discontinuity in the IMF or solar wind and the corresponding discontinuous change in the observed *SYM-H* index was only 10 min or less. This is consistent with the 0 to 4 h time lag in statistical studies that relate the peak in IMF B_z or solar wind electric field with the minimum in *Dst* [*Smith et al.*, 1999; *O'Brien and McPherron*, 2000; *Gonzalez and Echer*, 2005].

The modeled *SYM-H*′ from the MHD-only simulation (green line) and from the MHD + RCM simulation (blue line) is also plotted. Again there is remarkable agreement between the observed values of the *SYM-H*′ and the MHD + RCM simulation. This gives us confidence that the MHD + RCM simulation is reproducing the major features of the event. The *SYM-H*′ from the MHD-only simulation (green line) remains positive throughout, indicating no significant ring current development.

There are two unusual aspects to the *SYM-H* during this event. First, the ring current was powered by intervals of southward IMF lasting less than 30 min each. Statistical studies indicate that strong magnetic storms with minimum $Dst \le -100$ nT require a threshold of IMF $B_z \le -10$ nT for a minimum of 3 h [cf. *Gonzalez et al.*, 1994]. Second, the ring current growth continued reaching minimum *SYM-H** values during northward IMF conditions. This was pointed out by *Du et al.* [2008] and is believed to be the first such reported instance of this kind.

5. The IMF B_y Magnetosphere

5.1. Reconnection Under Strong Versus Weak IMF B_y

The same process that captures solar wind plasma to form a cold dense plasma sheet also produces intense field aligned currents, strong electric fields and high Joule heating rates in the cusp region when significant IMF B_y is also present. In the case of the 21 January storm, the high speed and exceptional dynamic pressure of the solar filament further amplified these effects. Another important factor was the arrival of the filament after a significant ring current had already formed. The formation of the CDPS and related effects are important factors in many of the unusual geospace features observed during the storm.

This paper presents two important advances. First, we expand upon previous MHD simulations of the CDPS [cf. *Li et al.*, 2005, 2008; *Welling and Ridley*, 2010] by including a coupled kinetic model of the ring current so the investigation of this phenomena can be extended farther into the inner magnetosphere. These previous simulations, using only MHD models, underpredicted the temperatures in the inner magnetosphere by an order of magnitude and thus were forced to consider only regions more distant from the Earth in their analysis. Second, a rich data set from the combined LANL geosynchronous satellites and Double Star TC-1 covering all magnetic local times is available to compare with the simulation. The compression of the magnetopause to locations inside geosynchronous orbit on the dayside allowed these satellites to sample conditions in the magnetosheath, low-latitude boundary layer, dayside magnetosphere, and nightside plasma sheet.

The development of the CDPS is the result of a recently appreciated mode of coupling between the solar wind and the magnetosphere as simultaneous or nearly simultaneous lobe (also called poleward-of-cusp) reconnection in both hemispheres converts IMF flux tubes containing solar wind plasma directly into magnetospheric flux tubes [cf. *Song and Russell*, 1992; *Raeder et al.*, 1995, 1997]. The result is a large rate of solar wind mass transfer into the magnetosphere [cf. *Palmroth et al.*, 2006; *Lavraud et al.*, 2006; *Øieroset et al.*, 2005, 2008; *Li et al.*, 2005, 2008, 2011], which is not species or charge-state dependent. Simulations and observations show that this process creates the dayside LLBL in a timescale on the order of 10 min and a nightside CDPS with a time delay of hours. In this case, exceptionally dense solar filament material entered the magnetosphere.

As these studies have demonstrated, in the process of double lobe reconnection, the IMF merges with a lobe field line in one hemisphere creating an open field line that drapes over the dayside magnetopause into the opposite hemisphere. This open field line subsequently recloses at the reconnection site poleward of the cusp in the opposite hemisphere capturing solar wind plasma, which is relatively cold (~1 keV), into the magnetosphere. The closed field line moves sunward under the action of magnetic tension, sinks into the magnetosphere, and then drifts to the nightside in response to pressure gradients, building a dense plasma sheet on the nightside from the flanks inward.

When a significant IMF B_y component is present, the cusp is shifted away from noon in both hemispheres. For positive IMF B_y, the shift is toward the duskside in the Northern Hemisphere and the dawnside in the Southern Hemisphere. For negative IMF B_y, the opposite occurs. As pointed out by *Imber et al.* [2006], because of this displacement, different interplanetary magnetic field lines interact *independently* with reconnection sites in the Northern and Southern Hemispheres. Figure 4 shows the magnetospheric configuration at 20:05 UT in the MHD + RCM simulation under northward IMF conditions with a significant eastward (positive) B_y component that existed during the WDPS interval. The regions of minimum magnetic field strength mark the cusps in the upper panel, which is a magnetospheric cross section at $X = 2\ R_E$. The cusps are shifted to the duskside in the Northern Hemisphere and the dawnside in the Southern Hemisphere as expected. The lines in the figure are magnetic field lines projected into the *YZ* plane. Planes intersecting the two cusps are given in the figure—one intersecting the southern cusp at $Y = -3\ R_E$ and the other the northern cusp at $Y = +2\ R_E$. Reconnection in the Southern Hemisphere between the IMF and a lobe field line creates an open field line that overdrapes into the Northern Hemisphere. In agreement with *Li et al.* [2011], the newly opened field line moves sunward as it straightens out and then moves toward noon and also toward the Northern Hemisphere cusp region under the influence of the solar wind flow. The result is a region of overdraped open field lines just outside the magnetopause on the duskside that are connected to the Southern Hemisphere and on the dawnside that are connected to the Northern Hemisphere. An X line develops in the Northern Hemisphere as the overdraped field line from the Southern Hemisphere reaches the cusp null in the Northern Hemisphere.

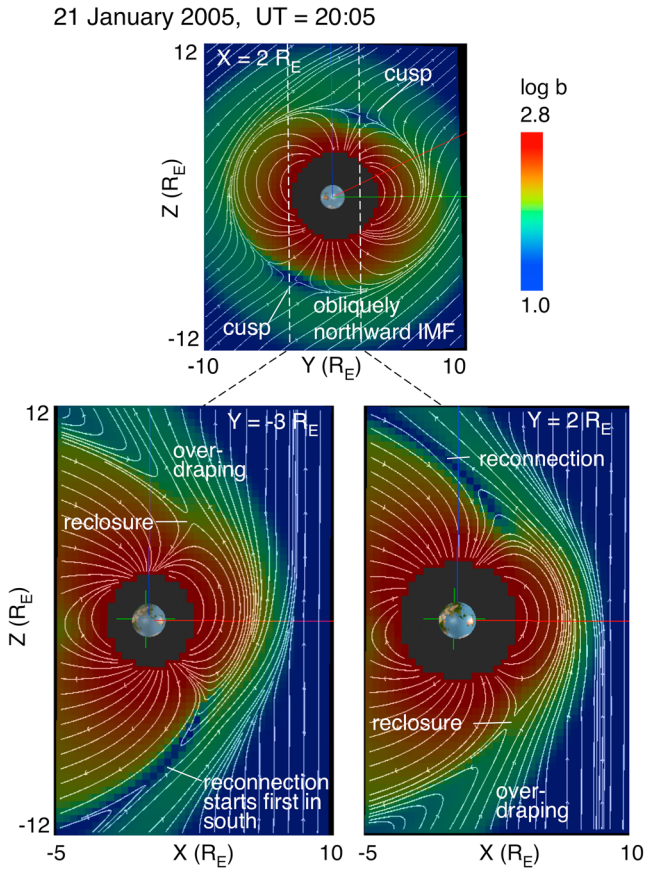

Figure 4. Cross sections of magnetic field strength from the MHD + RCM simulation showing double lobe reconnection during the strong IMF B_y and northward IMF conditions associated with the initial formation of the cold dense plasma sheet at 20:05 UT on 21 January 2005. The top shows the weak magnetic fields (blue) that identify the cusp regions shifted to the duskside in the Northern Hemisphere and the dawnside in the Southern Hemisphere as is expected for positive IMF B_y. The dashed lines indicate the locations of the two *XZ* cross sections shown in the lower part of the figure—the first intersecting the southern cusp and the second the northern cusp. Each cusp reconnects independently with the IMF. Open field lines then overdrape into the opposite hemisphere and move toward noon from either side reclosing poleward of the opposite cusp. The solar wind plasma on the IMF segment of the reclosed field line is captured directly into the magnetosphere.

At this site, Southern Hemisphere open field lines are reclosed and subsequently sink into the magnetosphere. Farther tailward, the reconnection process returns IMF to interplanetary space. As soon as a closed field line is created, solar wind plasma is trapped within the magnetosphere forming a boundary region of magnetosheath-like plasma on closed field lines. A similar process occurs in the Northern Hemisphere on the duskside, shown in Figure 4 in the $Y = 2\ R_E$ plane.

During due northward IMF, both cusps are located close to noon MLT. A single IMF field line can drape over the magnetopause intersecting cusp nulls in both hemispheres and reconnecting poleward of both cusps nearly simultaneously. This process converts an IMF flux tube containing solar wind plasma nearly instantaneously into a magnetospheric flux tube. And, in fact, for IMF clock angles of ±10°, there is evidence for this *dual-lobe* reconnection process [*Imber et al.*, 2006]. However, because of the dipole tilt in January, even for due northward IMF conditions, reconnection occurs at different times in the two hemispheres rather than simultaneously. As a result, the same double high-latitude reconnection process operates in the simulation under due northward IMF conditions as well. This configuration is shown in Figure 5 in the same format as in Figure 4 but at 21:35 UT during due northward IMF conditions associated with the second CDPS interval in the simulation. Figure 5 (top) shows both cusps near noon as expected. Figure 5 (bottom) intersects the two cusps in the $Y = 0$ plane. The direction of the dipole tilt selects the hemisphere where reconnection begins first [*Lavraud et al.*, 2005] and is strongest. Because the southern cusp is shifted closer to the subsolar point, magnetosheath flows are slower there. With slower flows, reconnection rates are larger [cf. *Park et al.*, 2006]. Field lines reconnect there first and the open field line overdrapes directly into the Northern Hemisphere cusp region to reclose. These overdraped field lines from the Southern Hemisphere do not have far to travel before encountering the cusp null in the Northern Hemisphere and reclosing. So the reconnection is nearly simultaneous in both hemispheres, creating a thin layer of open field lines just outside the magnetopause connected to the Southern Hemisphere only.

Figure 6 shows density contours in the equatorial plane and through the northern cusp region near the same times as in Figures 4 and 5 that have been color coded based on the topology of the magnetic field lines crossing these planes. Red indicates closed field lines, blue IMF, green open field lines with footpoints in the Southern Hemisphere, and gold open field lines with footpoints in the Northern Hemisphere. The contours of high density associated with the subsolar LLBL and cusp are marked in these plots. At 20:05 UT, when the IMF

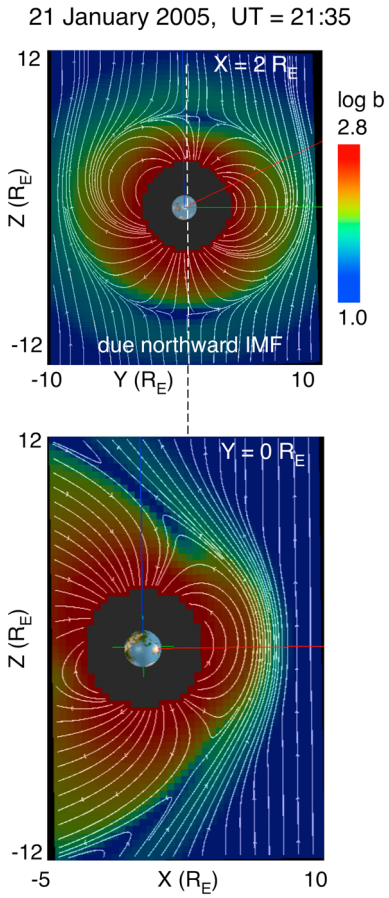

Figure 5. Cross sections of magnetic field strength are presented from the MHD + RCM simulation showing double poleward-of-cusp reconnection during almost purely northward IMF conditions later in the storm at 21:35 UT on 21 January 2005. The top shows the weak magnetic fields (blue) that identify the cusps at noon MLT in both hemispheres. The dashed line indicates the location of the *XZ* cross section shown in the lower part of the figure. Because of the dipole tilt in January, reconnection begins first in the Southern Hemisphere. Open field lines overdrape into the Northern Hemisphere and are rapidly reclosed by a second poleward-of-cusp reconnection capturing solar wind plasma contained on the field line.

is northward but with a significant IMF B_y component, a layer of open field lines appears just outside the magnetopause. These open field lines connect to the Southern Hemisphere on the duskside and the Northern Hemisphere on the dawnside as implied by Figure 4. At 21:35 UT, when the IMF is almost due northward, the shortened time delay between reconnection in the Southern Hemisphere (where it begins first) and reclosure in the Northern Hemisphere produces a thinner layer of open field lines anchored in the Southern Hemisphere (green) only. An important consequence of the double lobe reconnection is that both the northern cusp and the LLBL are on closed field lines (red).

5.2. Energy Inputs in the Cusp Region

5.2.1. Intense Joule Heating

Intense Joule heating in the cusp region is another important consequence of reconnection during significant IMF B_y conditions combined with either northward or southward IMF. As pointed out by *Li et al.* [2011] on the basis of an MHD simulation, the total cusp Joule heating varies with the magnitude of the IMF B_y component, the speed of the solar wind, and the strength of the field aligned currents. All of these elements are enhanced during the time of the filament impact on 21 January 2005 resulting in exceptional levels of Joule heating on the dayside. A detailed description of the processes involved is presented by *Li et al.* [2011], which is briefly summarized here. Focusing for the moment on the case of northward IMF and positive IMF B_y as an example, the cusps are shifted to the duskside in the Northern Hemisphere and the dawnside in the Southern Hemisphere. The reverse is true for negative IMF B_y. Poleward-of-cusp (or lobe) reconnection creates an open field line which is subsequently dragged along by the solar wind flow, first sunward from dusk toward noon to remove the kink in the field line (produced by lobe reconnection) and then along the flanks to the magnetotail. The magnitude of the IMF B_y is important because it essentially controls the length and orientation of the path taken by the field line through the ionosphere through the shift of the reconnection site (cusp) toward dusk. As the field line is pulled through the ionospheric plasma, the collisional friction between the ions moving with the field line and the background neutrals cause intense heating. In another way of looking at this process, the movement of the field line through the ionosphere creates two intense and oppositely directed FACs in the cusp region. As these FACs close through the ionosphere, a fast $E \times B$ flow channel develops between them. This fast flow channel is associated with strong electric fields which produce large Joule heating rates. The stronger the FACs, the stronger the closure currents and Joule heating all else being equal. When the field lines eventually reclose, they are no longer dragged along by the fast solar wind flow, and the Joule heating rate drops. If the variation in the ionospheric electric field with height is neglected, the Joule heating rate for the volume below a satellite in low-Earth orbit is approximately equal to the Poynting flux.

The strong dynamic pressure of the solar filament must also be a factor in amplifying the cusp Joule heating rates during this event. It is known that high dynamic pressure enhances the entire magnetospheric current system within minutes and intensifies particle precipitation [cf. *Zhou and Tsurutani*, 1999, 2003; *Zhou et al.*, 2003; *Liou et al.*, 2007; *Laundal and Østgaard*, 2008]—two important factors in cusp-region energy input. It also dramatically increases the projected area of the cusp in the ionosphere even during northward IMF conditions [*Newell and Meng*, 1994]. All of these factors must increase the integrated Joule heating and

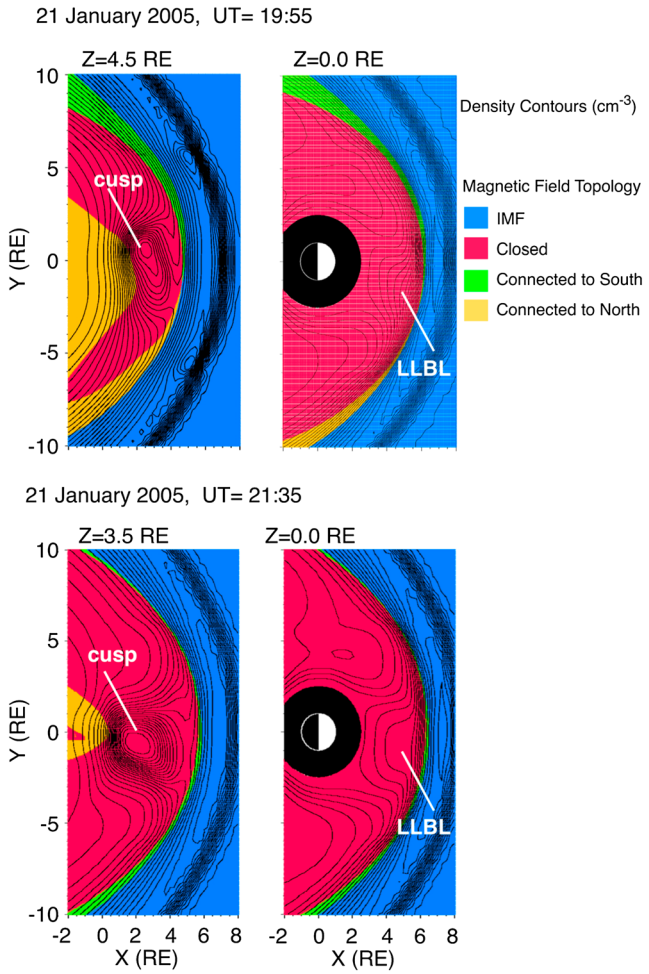

Figure 6. Contours of log *N* on *XY* planes through the cusp and in the equatorial plane are given at two times during the simulation—19:55 UT during comparable IMF B_y and B_z and at 21:35 UT during almost purely northward IMF. The signature of the high densities in the cusp and in the subsolar LLBL is indicated. Magnetic field lines through these planes are color coded by their topology as indicated. In both cases, the cusp and LLBL are on closed field lines.

precipitating particle flux in the cusp and thus amplify the energy input into the atmosphere in this region though the exact nature of this interconnection requires further investigation.

Figure 7 compares the simulated Joule heating rates and their projected area in the ionosphere from the MHD + RCM simulation at selected times before and after the arrival of the solar filament. Since the simulation provides a measure of the magnitude of the total current density, we calculate the Ohmic dissipation rate from the expression, $W_{diss} = E \cdot J = J^2 \Sigma_P / (\Sigma_P^2 + \Sigma_H^2)$, where J is the horizontal current, Σ_P is the Pedersen conductance, and Σ_H is the Hall conductance. As shown in the formula, Joule heating is proportional to horizontal ionospheric Pedersen currents that close between the regions 1 and 2 FACs in the ionosphere and to the electric fields that are generated in this process. Note that these electric fields, in turn, drive Hall currents that are the major contributor to the ionospheric electrojet currents and the ground geomagnetic signatures. Of course, the contributions of neutral winds to the Joule heating rates [cf. *Lu et al.*, 1995] are not included in this calculation. The errors introduced by this approximation during the 21 January 2005 storm, during which significant neutral winds developed in response to the strong Joule heating in the cusp region (discussed in section 6.2.2), require further study.

For each selected time, Figure 7 (top row) displays Joule heating rates in the ionosphere with the maximum value of the Joule heating rate in mW/m^2 indicated in the upper right-hand corner, (middle row) the FACs J_{par}, and (bottom row) the ionospheric electric field. In agreement with *Li et al.* [2011], we find that regions of Joule heating are greatly expanded during intervals of larger clock angle (stronger IMF B_y). It is important to note that even for comparable IMF orientations, there was a dramatic increase in the area of ionospheric cusp signature after the arrival of the high dynamic pressures in the solar filament.

The MLT distribution of the Joule heating varied significantly depending on the IMF orientation. During the strongest southward IMF of the storm at 18:39 UT, Joule heating rates peaked near midnight MLT at 168 mW/m^2 while in the cusp, they reached only 80 mW/m^2. At 18:50 UT, an abrupt and almost step-like increase in cusp region Joule heating to maximum values of 174 mW/m^2 occurred near 18:50 UT in the presence of strong IMF B_y and high dynamic pressure at the leading edge of the solar filament despite the somewhat weaker southward IMF. The arrival of the solar filament greatly expanded the ionospheric area occupied by the strongest cusp Joule heating rates compared to the area at 18:39 UT prior to the filament arrival. Maximum Joule heating rates in the obliquely northward IMF portion of the filament fell to ~ 80 mW/m^2 dropping gradually to tens of mW/m^2 by 20:30 UT and then lower as the IMF turned more purely northward. The result is a large spike in Joule heating from 18:47 to 20:00 UT over the course of a little more than an hour.

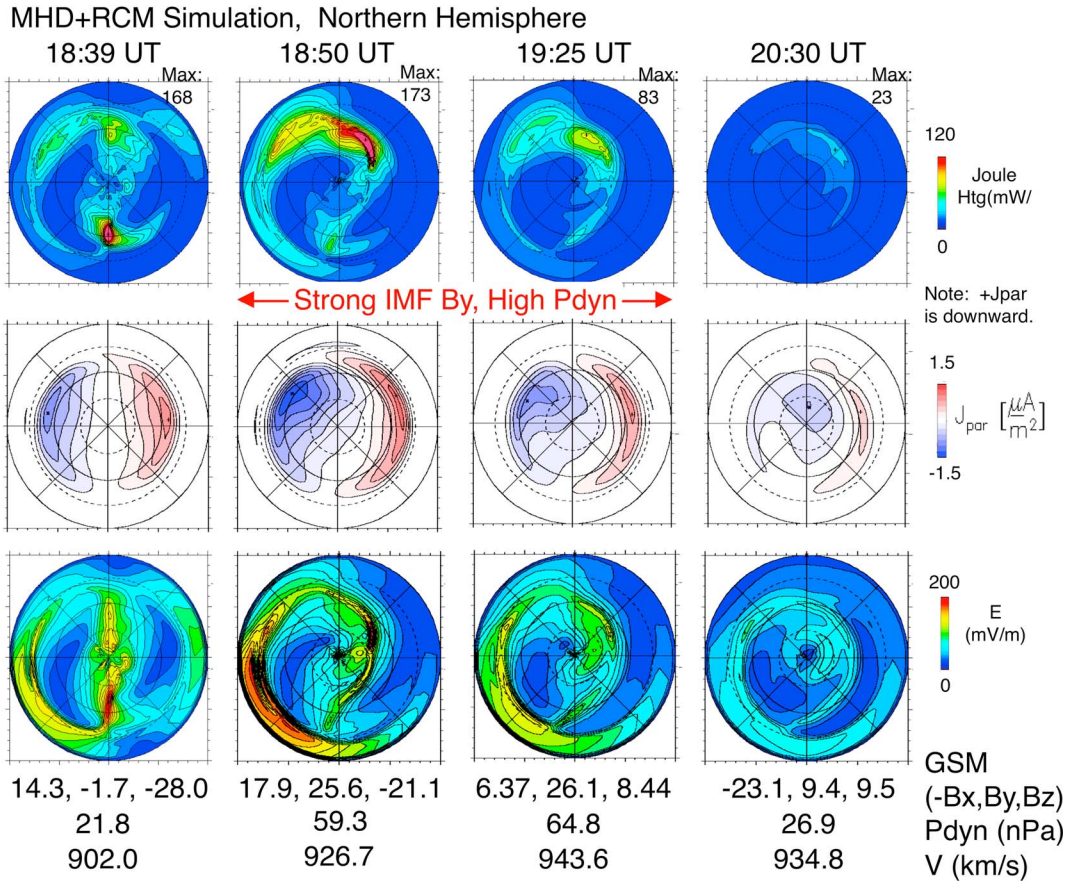

Figure 7. Joule heating rates, field-aligned currents (J_{par}), and electric field (E) in the ionosphere are shown at (1) 18:39 UT the time of strongest southward IMF in the storm, (2) 18:50 UT during the short southward IMF interval at the leading edge of the dense filament, (3) 19:25 UT during northward IMF and strong IMF B_y, and (4) 20:30 UT during comparable northward IMF and IMF B_y and reduced solar wind dynamic pressure. During all times, the solar wind speeds were comparable and over 900 km/s.

For the strong IMF B_y conditions at 18:50 UT, 19:25 UT, and 20:30 UT in the figure, the largest electric fields and Joule heating rates are found in narrow flow channels that develop between large-scale FACs on the dayside in agreement with *Li et al.* [2011]. But strong electric fields also develop on the nightside in association with the partial closure of region 2 FACs through the low conductances equatorward of the auroral oval. These strong electric fields, which maximize during the period of southward IMF and high solar wind density at the leading edge of the solar filament, are associated with the ring current development and are not present in the MHD-only simulation (see Figure 19). However, they produce only weak levels of Joule heating due to the low conductances in this region.

The Joule heating rates in the MHD + RCM simulation are compared to the unusual levels of downward Poynting flux into the cusp region observed during two passes of DMSP F15 on 21 January presented by *Li et al.* [2011]. DMSP 15 did not pass through the cusp itself but clipped the dawnward edge of the region surrounding the cusp on each pass. As a result, it likely missed the region of peak dayside Joule heating predicted by the simulation. This also has consequences for the AMIE-derived total Joule heating rates (shown in Figure 3), which ingested DMSP 15 and DMSP 16 observations and likely also underestimated the contribution of Joule heating in the cusp region and thus the relative strengths of the three peaks in Joule heating driven by the sheath and leading edge of the solar filament. Between 17:30 and 21:30 UT, typical values of the downward Poynting fluxes along the DMSP satellite track on the dayside were 30–50 mW/m^2 but narrow spikes were observed on top of this background to values >100 mW/m^2 at ~17:40 UT and just after 20:00 UT. Poynting fluxes dropped to values ≤ 20 mW/m^2 just before 21:00 UT with the rotation of the IMF to a more purely northward direction.

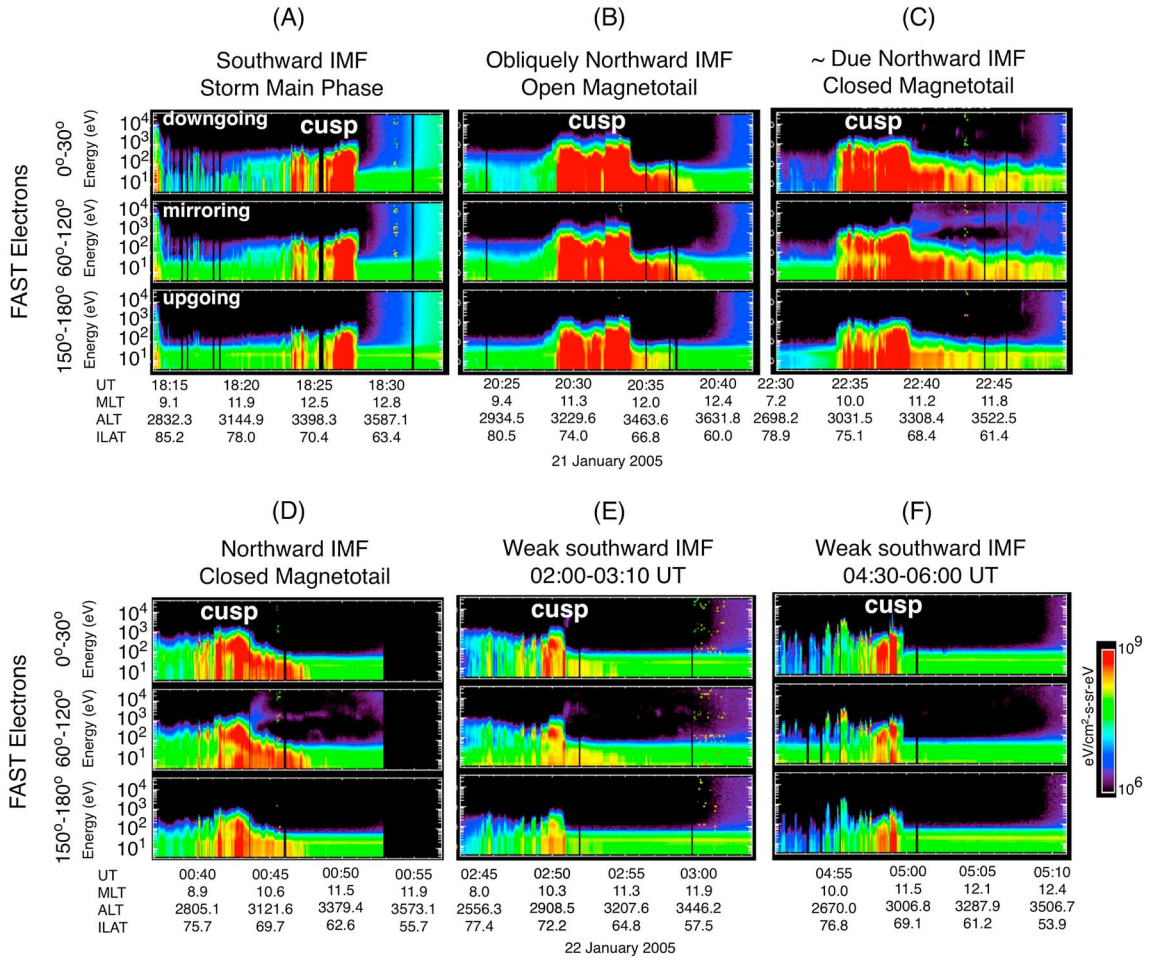

Figure 8. The electron flux in the cusp region was observed by the FAST satellite at ~3000 km altitude every 2.2 h during the 21–22 January 2005 magnetic storm. In addition to the typical region of dense magnetosheath-energy electrons in the cusp, (b–d) there is an additional region of softer energy electrons immediately equatorward only during northward IMF conditions. It was absent in the southward IMF interval before the (a) solar filament arrival and disappeared rapidly when the IMF again (e, f) turned southward. Locally mirroring keV electrons appear in the same region as the soft electrons, more faintly, and only at the equatorward edge of the cusp.

In the MHD + RCM simulation, maximum Joule heating rates reached ~20 mW/m^2 at 17:40 UT and 36 mW/m^2 at 20:00 UT, a bit lower than the values observed by DMSP F15. No spikes to 100 mW/m^2 were produced in the simulation near the times indicated. By 21:00 UT, Joule heating rates dropped below 20 mW/m^2 in agreement with the DMSP Poynting flux estimates and by 22:00 UT below 10 mW/m^2. Unfortunately, DMSP F15 was not near the cusp when the simulation predicts the highest Joule heating rates between 18:47 UT and 19:00 UT.

5.2.2. Localized Upwelling of the Neutral Atmosphere Near the Cusps

The 21 January 2005 magnetic storm had an anomalously high level of efficiency for converting energy from the merging electric field into thermospheric expansion as indicated by orbit-averaged densities measured by the CHAMP and GRACE satellites over the years 2002–2005 [*Lühr et al.*, 2004; *Liu et al.*, 2005a, 2011]. The merging electric field $E_m = V_{sw}\, B_T \sin^2(\theta/2)$, where V_{sw} is the solar wind velocity, $B_T = \mathrm{sqrt}(B_y^2 + B_z^2)$ is the transverse component of the IMF in GSM coordinates, and θ is the IMF clock angle. E_m remains significant even after the IMF turns northward during the 21 January 2005 storm because the magnitude of the IMF B_y for a time is comparable to the IMF B_z. In addition, during this storm, the solar wind dynamic pressure reached the highest values observed in the 2002–2005 interval, likely amplifying both the precipitation into the atmosphere as well as the Joule heating in the cusp region.

Both intense Joule heating [cf. *Crowley et al.*, 1996, 2010] and soft electron precipitation [cf. *Schlegel et al.*, 2005; *Liu et al.*, 2005a; *Clemmons et al.*, 2008; *Sadler et al.*, 2012] are thought to contribute to these dayside thermospheric density enhancements reported near the cusp region [*Lühr et al.*, 2004; *Rother et al.*, 2007].

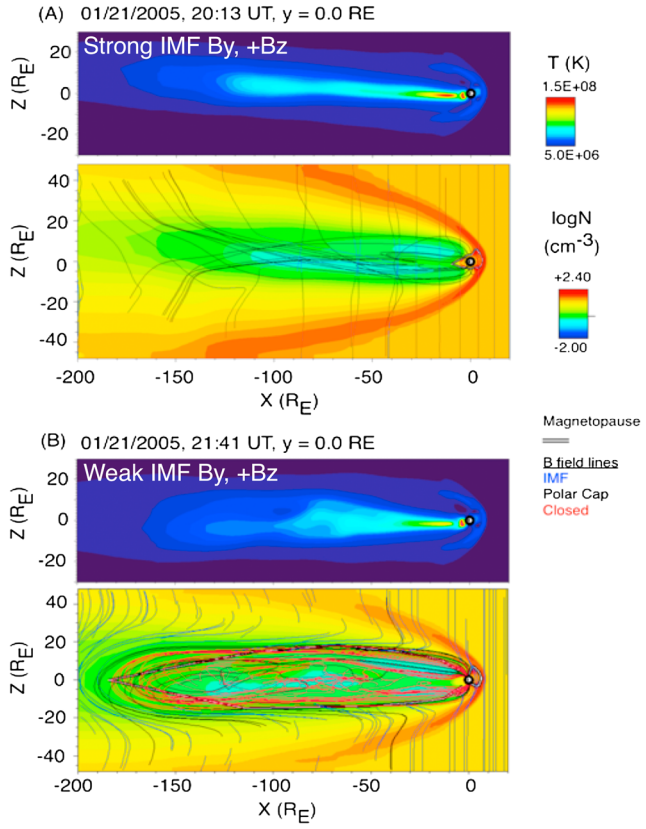

Figure 9. The changes in the topology of the magnetotail in the MHD + RCM simulation are shown at (a) 20:13 UT during obliquely northward IMF and (b) 21:41 UT just after the IMF turned more purely northward. Temperatures and densities are in agreement with typical values during cold dense plasma sheets in the magnetotail. (Note that green in the color bar is ~ 1 cm^{-3} and light blue is ~0.1 cm^{-3}). A warmer dense plasma sheet develops in Figure 9a with peak temperatures beyond 10 R_E of 14 keV. Cooler dense plasma sheets develop in the closed magnetotail at Figure 9b reaching values beyond 10 R_E of 9 keV. Temperatures in a cold dense plasma sheet are typically < 1 keV in the midtail region. (The color bar goes from 13 keV (red) to ~430 eV (dark blue).)

Since Joule heating occurs in the *E* and *F*1 regions, low in the thermosphere, effects transmitted to higher altitudes by changes in atmospheric scale height are expected to be weaker than changes due to direct high-altitude energy inputs from soft electron precipitation. The electron precipitation heats the ambient electrons, increasing their scale height. The upwelling electrons drag ions along through the ambipolar electric field that develops. The momentum in the upflowing ions is imparted to the neutral gas, creating a localized expansion of the high-altitude neutral atmosphere. The expansion of the thermosphere in the vicinity of the cusps also contributes to high-altitude pressure gradients that drive disturbance thermospheric meridional wind and transient wind surges.

In addition to an hour-long impulse of intense Joule heating, an expanded region of soft electron precipitation is observed by the FAST satellite during the northward IMF portion of the solar filament, shown in Figure 8. The plots give tens of eV to 30 keV electron fluxes in three pitch angle ranges that cover downward, locally mirroring, and upward directions. The cusp region electron precipitation at magnetosheath energies is labeled at the top of each panel. A region of soft electron precipitation equatorward of the ionospheric projection of the cusp develops during the extended northward IMF interval of the filament (see Figures 8b–8d). This region of soft electron precipitation does not exist during the southward IMF conditions in Figure 8a and disappears rapidly as the IMF turns southward again in Figures 8e and 8f. This same region of soft electron precipitation is visible in DMSP F13, F15, and F16 observations dawnward and duskward of the FAST observations. This expanded region of soft electron precipitaton is most likely a key factor in the extremely efficient expansion of the neutral atmosphere with respect to the strength of the merging electric field reported by *Liu et al.* [2011].

5.3. Effects of the Changing Topology of the Magnetotail

A distinctive change in the topology of the magnetotail occurs in the simulation marking the transition from obliquely to purely northward IMF, warm to cooler superdense plasma sheets, and high to low Joule heating rates. Figure 9 illustrates this distinctive topological change. In the figure, closed magnetic field lines are red, open field lines are black, and the IMF is blue. Prior to the first interval beginning at ~19:00 UT, an open magnetotail formed in the simulation from poleward-of-cusp reconnection under obliquely northward IMF conditions. By 20:08 UT, densities in the open midtail reached values on the order of 1 cm^{-3} (green) and temperatures 2–3 keV (light blue). Closer to Earth, temperatures climbed to 14 keV (red). Figure 9a shows an example at 20:13 UT of temperature and density panels respectively taken from the MHD + RCM simulation during this obliquely northward IMF interval. These high temperatures are consistent with the relatively warmer superdense plasma observed at geosynchronous orbit during this interval.

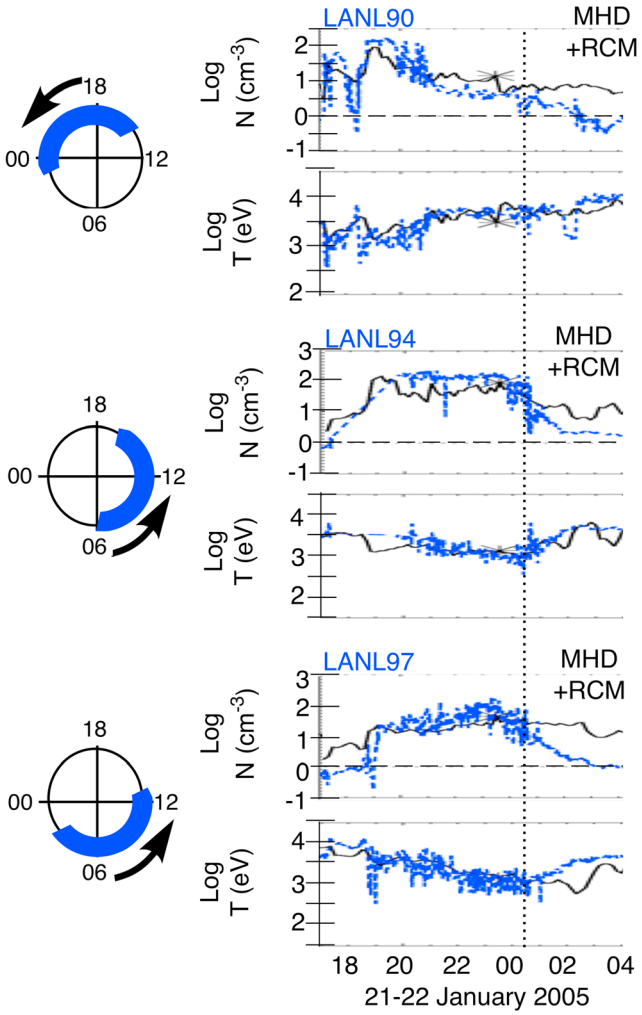

Figure 10. Log density (cm^{-3}) and log temperatures (eV) from the MHD + RCM simulation are given along each of three LANL satellite orbit tracks (black lines) compared to the observed densities and temperatures at these same locations (blue dots).

As the IMF turned more purely northward at 21:40 UT, the magnetotail in the simulation closed (meaning both ends of magnetic field lines were connected to the Earth) and stretched out to over 150 Earth radii in length. At this same time, the observed b2i boundary in the dusk-midnight local time sector (Figure 3j), which marks the transition from dipolar to stretched magnetic field lines [*Newell et al.*, 1998], moved to its lowest latitude position. In the simulation, plasma densities (shown, for example, in Figure 9b at 21:41 UT) remained near 1 cm^{-3} (green) in the midtail region. However, temperatures cooled. By 22:20 UT (not shown), the magnetotail decreased in length to ~60 R_E, magnetotail stretching decreased, and the LANL satellites reentered the plasma sheet to again observe a unusually dense but cooler population. In the simulation, densities in the midtail region, reached 1–10 cm^{-3} (green to yellow) and temperatures cooled even further. These densities and temperatures are consistent with typical observed values of 1 cm^{-3} and < 1 keV (1.16×10^7 K) in this region [cf. *Terasawa et al.*, 1997].

5.4. Development of the Cold Dense Plasma Sheet

The MHD + RCM simulation is compared with observations to explore the development of the CDPS and its local time characteristics. This is particularly important because the dense populations of the LLBL are on closed field lines and thus form part of the dayside plasma sheet. The compression of the magnetosphere places dense LLBL populations at the nose of the magnetosphere and along the flanks into close proximity with the inner magnetosphere introducing the potential for changes in the plasma wave environment or the ring current source populations. To validate the simulation, Figure 10 compares the density and temperature (black lines) along three LANL satellite paths in the MHD + RCM simulation to observed densities and temperatures (blue dots). In general, there is close agreement during the interval of primary interest from 17:00 UT on 21 January to 00:40 UT on 22 January.

The simulation allows us to place the LANL and TC-1 satellite observations into a global context that includes the relationship to important plasma boundaries and regions. To orient the reader, Figure 11 shows a typical plot of log plasma number density in the $Z_{GSM} = 0$ plane from the simulation with these boundaries and regions identified. Magnetosheath/solar wind plasma captured as a result of double poleward-of-cusp reconnection is seen as a narrow region of high-density plasma within the magnetopause near noon. This plasma subsequently populates the much thicker boundary layers at the dawn and dusk flanks. The CDPS fills from the flanks inward on the nightside. On the dayside, a pseudo plasmaspheric drainage plume is seen in the simulation as convection pulls out plasma from the model inner boundary at $L \sim 2.5$ R_E. Drainage plumes are regions of cold plasma that develop as enhanced convection strips away the outer layers of the plasmasphere and sweeps them sunward (cf. review by *Lemaire* [2000], observations of global structure by

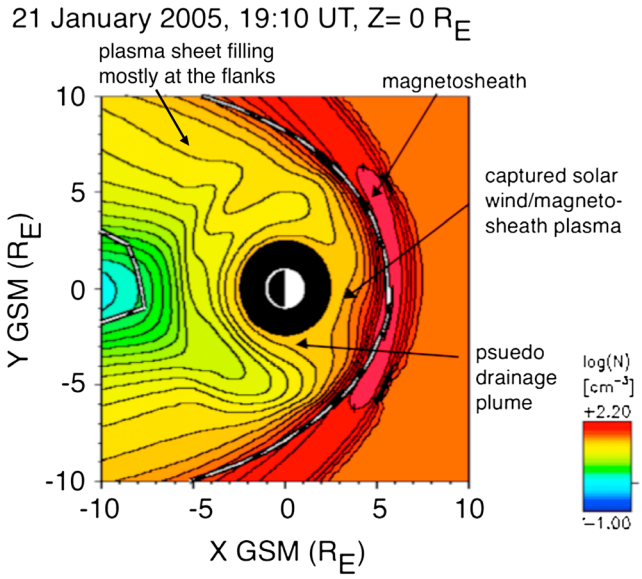

Figure 11. Identification of plasma populations is shown in a typical *XY* cross section of log N from the MHD + RCM simulation to aid in placing satellite observations into global context.

Goldstein et al. [2004], and discussion of characteristics at geosynchronous orbit by *Borovsky and Denton* [2008]). As noted by *Borovsky et al.* [2008], this process in the MHD model is insufficient to create a realistic plasmasphere, which requires field-aligned ionospheric outflow at all latitudes into the corotating inner magnetosphere. However, it does provide information on the location of plasmaspheric structures that are driven by convection.

In Figure 12, cross sections of log *N* from the simulation are given at the top with the locations of LANL satellites projected into the equatorial plane indicated by colored dots. The particular color associated with each satellite appears in the legend on the right side of the figure. Below these cross sections, LANL densities, temperatures, and the associated magnetic local times are plotted in four different magnetic local time sectors. The observations are color coded to identify the satellite providing them. In each of these magnetic local time sectors, the times for which cross sections from the simulation are displayed above are marked by vertical dashed lines.

In the dayside local time sector, both LANL 1994-084 (purple) and LANL 097A (orange) are in the magnetosheath observing densities near 100 cm^{-3} and temperature ~ 1–2 keV until just after 00 UT on 22 January. As the solar wind dynamic pressure decreases at the trailing edge of the solar filament, the LANL satellites observe the magnetosheath, then the LLBL, and finally the dayside plasma sheet as the magnetosphere expands outward sweeping over them. After 02 UT, the IMF has rotated intermittently southward again and the dayside plasma sheet returns to values near and below 1 cm^{-3} and temperatures of 5–10 keV.

In the dawn sector (03–09 h MLT), LANL-097A (orange) sees the temperature rise and the density drop abruptly at the shock arrival at ~17:11 UT and then again at the time of the filament arrival near 18:45 UT. These are likely brief excursions into the lobes as indicated by the low densities and high temperatures relative to the plasma sheet. As LANL-097A (orange) approaches the dawn flank and enters the LLBL at 19:00 UT, the density rises to 20–30 cm^{-3} and the temperature reaches 6–7 keV. LANL-097A continues into the much thinner prenoon LLBL by 22:00 UT where densities fluctuate from tens to 100 cm^{-3}. The temperature drops from 6–7 keV to 1–2 keV as 097A enters the magnetosheath near ~23 UT and ~9 MLT. At this same time (just after 22:00 UT), LANL-02A (green) is just entering the dawn sector from the postmidnight magnetotail. At this location, densities rise from 2 cm^{-3} to 5 cm^{-3} and temperatures cool to 4–5 keV. After 02:00 UT, as the IMF turns southward, the plasma sheet densities observed by LANL-02A drop below 2 cm^{-3}. At the same time, LANL-01A (blue) is closer to midnight in the dawn sector and sees similar densities but higher temperatures more typical of the nightside magnetotail.

In the dusk sector (15–21 h MLT), LANL 1990-095 (red) is mostly in the magnetosheath until just before 20:00 UT. In agreement with LANL-097A, magnetosheath densities reach 100 cm^{-3} and temperatures are 1–2 keV. At 20:00 UT, 095 enters the LLBL and observes densities that fluctuate from tens of cm^{-3} up to magnetosheath values, then enters the duskside CDPS with densities of 3–6 cm^{-3} and temperatures of 4–5 keV. Near 02:00 UT, LANL 1994-084 (purple) observes the drop in densities to < 2 cm^{-3} and increase in temperature back to more normal plasma sheet values on the duskside after the return of southward IMF.

In the night sector (21–03 h MLT), LANL-02A (green) is on the postmidnight side of the magnetotail, while LANL-01A (blue) and LANL 1990-095 (red) are on the premidnight side. As the CDPS forms, the densities increase more rapidly on the premidnight side in agreement with the simulation. Densities at LANL-01A at

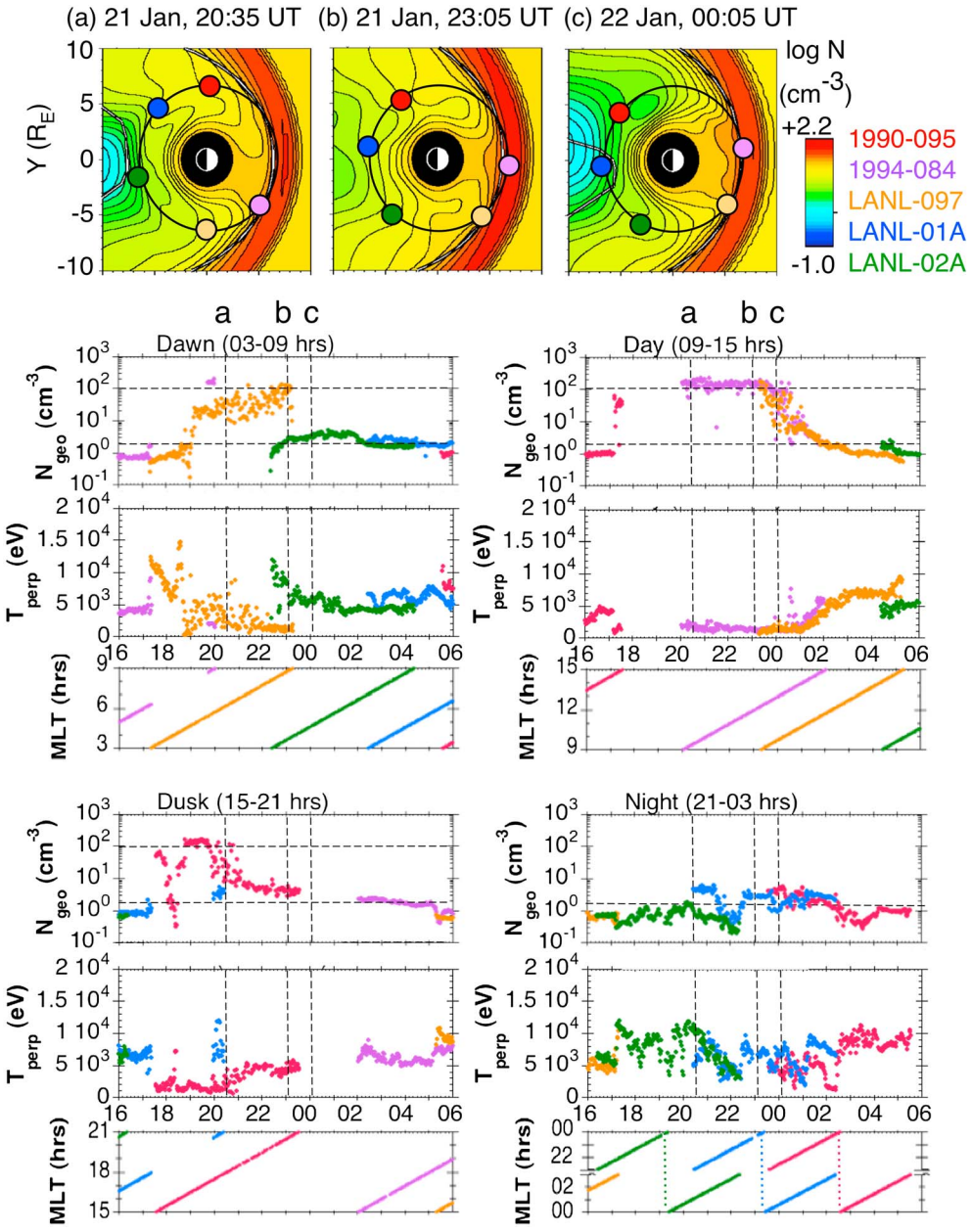

Figure 12. Characterizations of the density and temperature of the cold dense plasma sheet and its evolution at all local times are given by the LANL geosynchronous satellites. The cross sections in log *N* at the top from the MHD + RCM simulation place the positions of the LANL satellites into the global context. The satellites are identified in these cross sections and in the plots of density and temperature by the color coding at the upper right.

premidnight increase to superdense values ($>2\,cm^{-3}$) near 20 UT, drop to low values as the satellite enters the lobes at 21:40 UT, and then remain at superdense values until 02:00 UT when the satellite moves into the dawn MLT sector. LANL 1990-095 in the premidnight sector also sees the cold superdense plasma sheet and then the recovery of the density to more typical values at 02 UT. The temperature of the WDPS prior to 21:40 UT under obliquely northward IMF has a tendency to be warmer than that of the CDPS under more due northward IMF conditions.

The Double Star TC-1 satellite was also passing through the magnetosheath, LLBL, and plasma sheet during this time. TC-1 was launched into an equatorial elliptical $1.09 \times 13.4\ R_E$ orbit at 28.5° inclination in 2004. Figure 13 is a summary plot of TC-1 observations. At the top of the figure, equatorial plane cross sections of

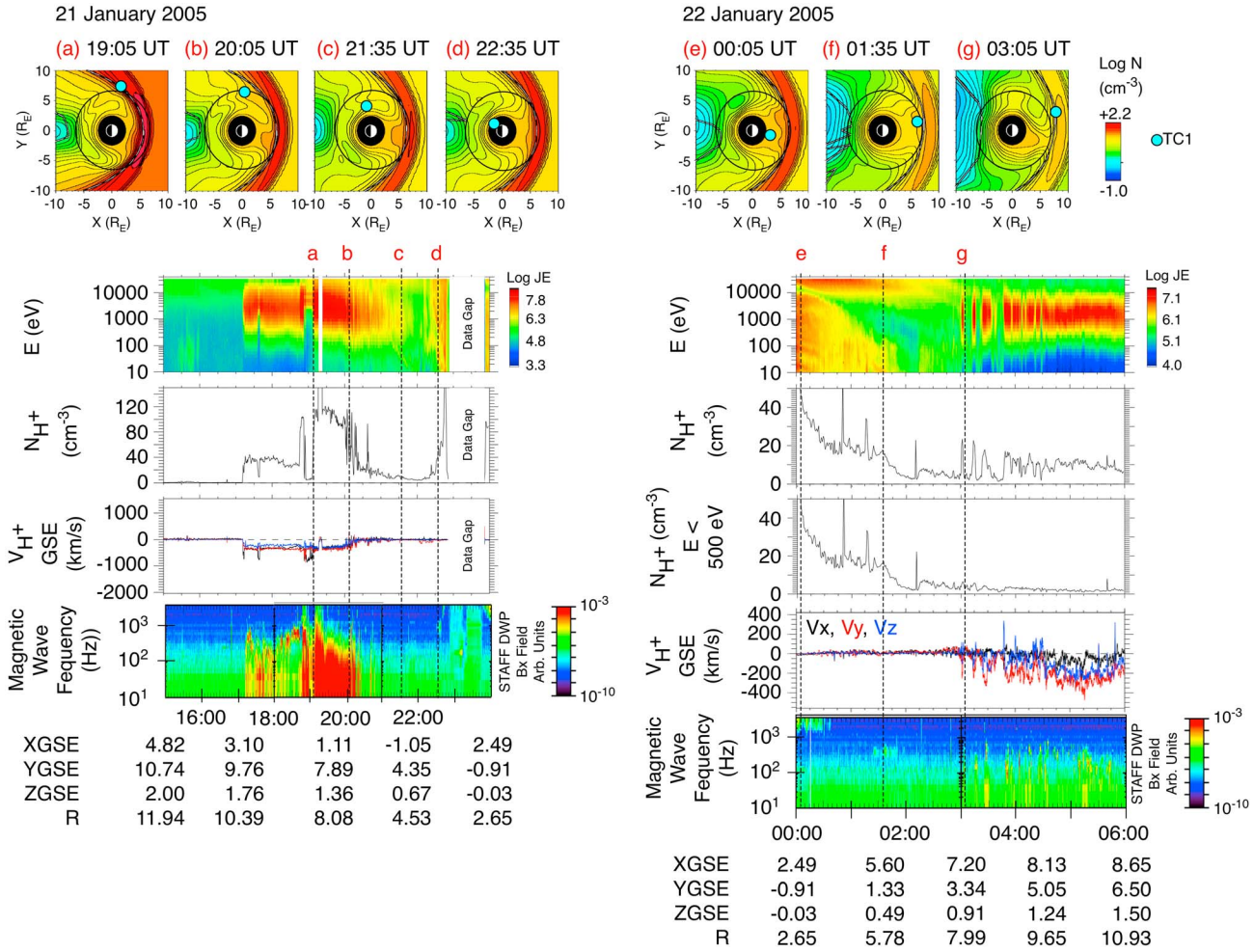

Figure 13. Observations are displayed of the entry of magnetosheath plasma, the dawn and dusk cold dense plasma sheet, and the drainage plume by Double Star TC-1 on 21 January from 15:00 to 24:00 UT (left column) and 22 January from 00:00 to 06:00 UT (right column). The (a–g) cross sections in log *N* at the top place the position of TC-1 (blue dot) into the global context provided by the MHD + RCM simulation. These times are indicated by vertical lines on the TC-1 summary plots. The top panel gives energy flux (JE) in keV/(sec cm^2 sr keV) over the range of 5 eV/q–32 keV/q. The second panel gives density integrated over this same energy range. In the right column, an additional panel is given showing the density integrated only below 500 eV. The next panel in each column gives the three components of H^+ velocity. The final panel gives the dynamic spectra of wave magnetic fields (color bar) plotted as frequency versus time from 10 Hz to 4 kHz.

log *N* from the simulation are used to place the location of TC-1 (blue dot) into global context. Since TC-1 orbits relatively close to the equatorial plane, we map its position onto the $Z = 0$ plane in the simulation for ease in comparison to LANL observations discussed previously. The times of the cross sections are indicated by dashed lines on the TC-1 summary plots labeled a–d for 21 January 15:00–24:00 UT (left column) and labeled e–g for 22 January 00:00–06:00 UT (right column). The top panel in each column displays ion energy fluxes (keV cm^{-2} s^{-1} sr^{-1} keV^{-1}) in the color bar versus energy and time in UT provided by the Hot Ion Analyzer (HIA) instrument on TC-1. HIA is an ion spectrometer that measures the 3-D distributions of the ions in the energy range from 5 eV/q to 32 keV/q without mass discrimination [*Reme et al.*, 2005]. A time of a data gap near perigee is indicated late on 21 January 2005. The second panel in both columns gives the ion density integrated over this full energy range. In the right column, a panel showing the number density contributed by ions with energy below 500 eV is also included. The next panel in both columns gives the three components of the H^+ velocity observed by TC-1. The final panel gives the dynamic spectra of wave magnetic fields (color bar) plotted as frequency versus time from 10 Hz to 4 kHz observed by the Spatio-Temporal Analysis of Field Fluctuations and the Digital Wave-Processing experiments [cf. *Cornilleau-Wehrlin et al.*, 2005].

Double Star TC-1 observed densities in the magnetosheath just after the shock (at ~17:10 UT) of 40 cm^{-3}. When the solar filament arrived near 18:45 UT and compressed the magnetosphere, TC-1 entered the solar wind. At 19:05 UT (cross section a), TC-1 reentered at 8.54 R_E to find a hotter, denser magnetosheath. Both simulations (with and without the RCM) show the bow shock nose at a little under 8.0 R_E at this time. In agreement with LANL satellites, densities at TC-1 in the magnetosheath increased to ~100 cm^{-3} after the arrival of the solar filament ultimately reaching 130 cm^{-3} [*Dandouras et al.*, 2009]. Plasma flows in the magnetosheath were ~ 650 km/s.

At 20:05 UT (cross section b), TC-1 observed a region of magnetosheath-like plasma but flowing at speeds approaching magnetospheric values consistent with magnetosheath capture by double lobe reconnection. This is the dayside LLBL. In agreement with LANL observations, ion densities in the LLBL fluctuated between 10 and 100 cm^{-3}. At 21:35 UT (cross section c), TC-1 crossed through the duskside CDPS and observed densities of 10–20 cm^{-3} at geosynchronous orbit in agreement with LANL satellites, dropping to 3.5–10 cm^{-3} on the nightside at smaller radial distances. At 22:35 UT (cross section d), TC-1 moved to radial distances near and inside the inner boundary of the MHD simulation on the nightside and found energy-dispersed ions with lower energies appearing at lower invariant latitudes.

Just after 00 UT on 22 January (cross section e), TC-1 reentered the model domain on the dawnside to observe energy-banded ions extending from 10 eV to 10 keV clearly separated in energy from the ring current ions, which start at 20 keV. Six energy bands were observed in this energy range. These ions appear to be a higher-altitude signature of an entirely new phenomenon, first reported in association with the 29–31 October 2003 superstorm in FAST and DMSP satellite data [*Cattell et al.*, 2004; *Kozyra et al.*, 2004; *Huang et al.*, 2005b; *Colpitts et al.*, 2012].

Though TC-1 cannot resolve ion species, observations on FAST demonstrate that H^+, O^+, and He^+ in the bands are at constant energy not constant velocity, so they cannot be understood in terms of velocity dispersion effects alone. When these warm ion bands are seen on FAST, they are coincident with VLF electromagnetic emissions that are observed in discrete frequency bands between 75 and 2000 Hz separated by 60–200 Hz [*Colpitts et al.*, 2012]. As these authors point out, the close coincidence between the frequency-banded waves and the energy-banded ions suggests that the ions may be the source of the waves. If the waves are generated at harmonics of the proton gyrofrequency, the inferred source region would be ~4000 km, which is above the location of FAST and below the altitude of the TC-1. TC-1 at this time is 0.02 R_E below the equatorial plane at a radial distance of ~2.7 R_E (dipole L ~ 3.5). On 21 January, these frequency-banded emissions were first observed by DEMETER [*Parrot et al.*, 2006] near 20:10 UT at altitude ~ 710 km, MLT ~ 9.7 h, and L ~ 2.9-3.7 (IL ~ 54–58.7). This time coincides with the arrival of the cold dense plasma sheet in the inner magnetosphere. On TC-1, plasma waves above 1 kHz were observed at the location of the energy-banded ions on the dawnside near 00 UT on 22 January but no similar wave signature was seen earlier on the duskside in association with the energy-dispersed ions near 22:35 UT on 21 January providing evidence that there are differences either in the mechanisms that produced these two different examples of energy-banded ions or in their interaction with the ambient plasma and wave environment at the two locations.

The warm banded ions encountered by TC-1 on the dawnside so far have been observed only during strong magnetic storms. In fact, they have been seen in every intense magnetic storm observed by the FAST satellite. *Colpitts et al.* [2012] suggest that the presence of these ions and associated VLF emissions implies a change in the geospace environment under extreme driving. Why these ions are present during the moderate 21–22 January 2005 storm is an interesting open question. Their appearance is consistent with the variety of other unusual phenomena typical of more extreme events that were also generated during this moderate storm.

At 00:25 UT on 22 January, a burst of low-energy ions appeared with energy and intensity increasing until 01:15 and then decreasing again. At geosynchronous orbit, LANL satellites observe a layer of ionospheric ions with similar characteristics adjacent to, and just inside, the magnetopause as the magnetosphere expands outward. Both LANL satellites and TC-1 then enter a region of plasmaspheric material associated with the drainage plume. Though no plasmaspheric model is included in the SWMF configuration, the location of the observed plasmaspheric material is consistent with the location of a pseudo drainage plume in the simulation that forms as plasma at the inner boundary of the MHD model is drawn out by plasma pressure gradients and participates in convection. TC-1 continues to move outward and then reencounters the magnetosheath plasma. At 03 UT (cross section g), TC-1 is moving in and out of the magnetosheath while traveling along the magnetopause in the simulation.

To summarize, LANL satellites and TC-1 witness the formation of the WDPS and CDPS and are able to characterize the associated changes in density and temperature at all local times. These satellites also confirmed the rapid return of the plasma sheet to hot, low-density conditions when southward IMF returned. Observations of the plasma sheet, LLBL, and magnetosheath agree well between LANL and TC-1 and are consistent with the simulation. Densities in the magnetosheath during the filament passage are near 100 cm^{-3} and temperatures are relatively hot for this region reaching 2 keV. The plasma sheet fills from the flanks inward. On the nightside in the magnetotail, the WDPS and CDPS reach densities of 5–6 cm^{-3}. In a narrow region on the dayside just inside the magnetopause and in broader regions on the duskside and dawnside, magnetospheric densities reach from tens of cm^{-3} to near magnetosheath values (~100 cm^{-3}). High densities (tens of cm^{-3}) and low temperatures (2–5 keV) on the dawn and dusk flanks as well as on the dayside are consistent with statistical studies of the dayside LLBL [cf. *Hasegawa et al.*, 2004]. Since the LLBL is closed during the double high-latitude reconnection that forms the WDPS/CDPS, these cold high-density regions are part of the dayside plasma sheet.

In the MHD + RCM simulation, the geosynchronous plasma sheet in a cold dense state is approximately a factor 2–5 times denser at dawn and dusk than at midnight. This can be compared to the factor of ~ 6 increase from the nightside to the dayside in observed densities at larger radial distances by the Time History of Events and Macroscale Interactions during Substorms satellites during a similar event [*Øieroset et al.*, 2008]. It is also similar to the evening and morning CDPS peaks seen during superstorms in the statistical study of *Liemohn et al.* [2008]. The width of the subsolar LLBL an hour after the IMF turned northward is ~2 R_E in the simulation. This can be compared to other observed events, which had thicknesses of 0.9 R_E in the subsolar region observed 25 min after northward turning [*Øieroset et al.*, 2008] and 5 R_E inside the magnetopause on the dawn flank [*Sauvaud et al.*, 1997]. The LLBL is observed to increase in thickness during northward IMF conditions.

5.5. Magnetotail Stretching

Despite the lower temperatures of the CDPS, its high densities at dawn and dusk are sufficient to stretch out the magnetic field lines that bring plasma into the nightside plasma sheet from both flanks. This stretching results from diamagnetic effects and is a surprising feature of the 21 January event. It is not known how frequently CDPS intervals achieve densities large enough to produce this effect.

The underlying physics of the diamagnetic field depletion can be described from both microscopic and macroscopic perspectives [cf. *Lühr et al.*, 2003]. In the microscopic view, charged particles gyrating about magnetic field lines generate a magnetic moment opposite in direction to the background magnetic field. The strength of an individual particle's magnetic moment varies directly with its perpendicular energy and inversely with the background magnetic field magnitude. Thus, for a cold plasma, the magnetic moment of the individual particles can be small. The diamagnetic effect requires collective effects in the plasma due to gradients in density, temperature, or magnetic field strength which generate current loops [*Engelhardt*, 2005]. The strength of the current in the loops varies with the density and temperature of the plasma. Since the plasma is confined close to the equatorial plane, where the field is largely in the B_z direction, the magnetic field depletion reduces the B_z component relative to other components stretching out the magnetic field line.

In the macroscopic view represented in MHD, pressure gradients in the plasma produce currents that are perpendicular to both the pressure gradients and to the background magnetic field. These currents reduce the background magnetic field in the high-pressure regions of the plasma. Of course, if the temperature is constant through a region, the pressure gradients correspond to plasma density gradients. The final view of diamagnetism given by *Lühr et al.* [2003] considers quasi-stationary plasma in the limit where magnetic tension can be neglected. In this case, the sum of magnetic and plasma pressure is approximately constant. If the plasma pressure increases, the magnetic pressure must decrease. The increase in plasma pressure can be achieved either by an increase in density (as for a CDPS) or in temperature (as for a typical hot tenuous plasma sheet during southward IMF conditions).

The diamagnetic effect was graphically demonstrated during the ion release experiments on the Active Magnetospheric Particle Tracer Explorers Ion Release Module mission. The magnetic field within the cloud of plasma generated by the chemical release vanished and only reappeared when the high densities in the cloud dissipated [e.g., *Lühr et al.*, 1986a, 1986b].

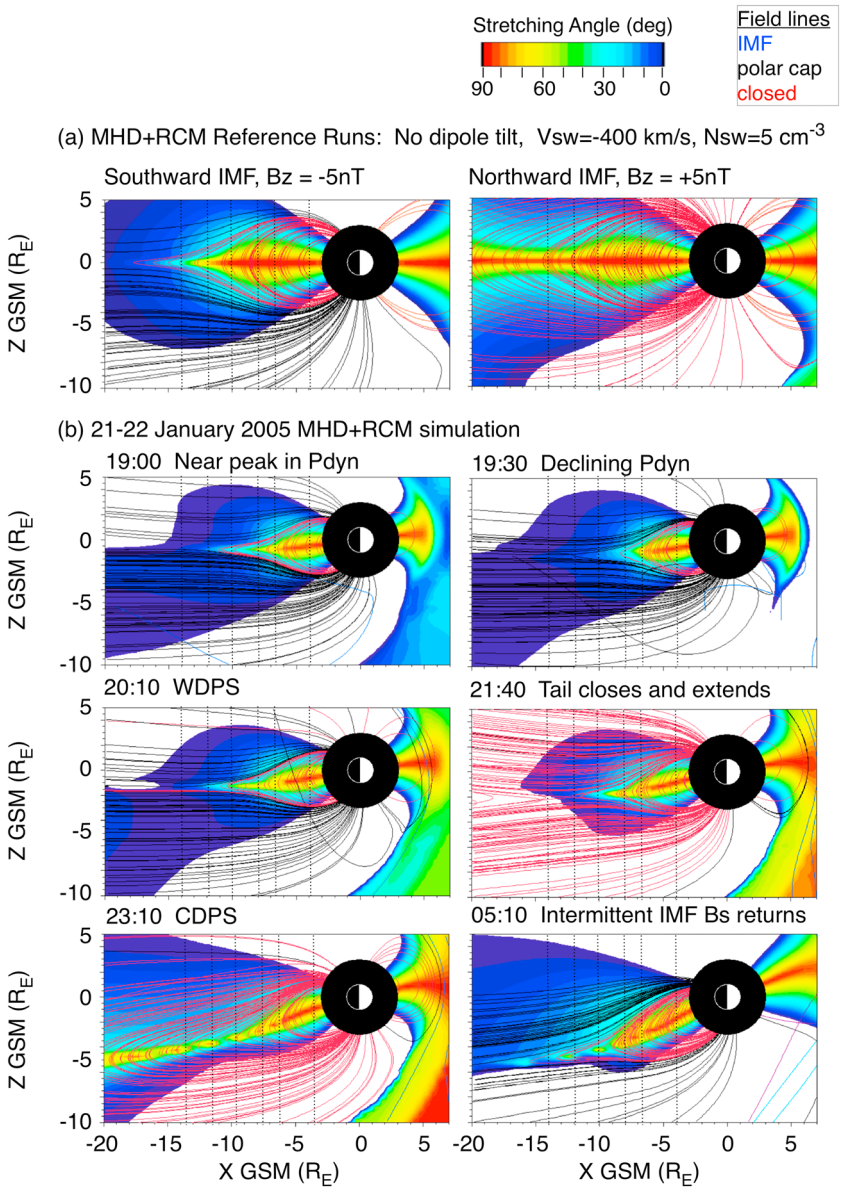

Figure 14. *XZ* cross sections of the magnetic field stretching angle at $Y = 0$ are displayed from (a) northward and southward IMF steady state reference models and (b) the time accurate MHD + RCM simulation of the 21–22 January 2005 magnetic storm. Only positive stretching angles associated with closed magnetic field lines are displayed. Dipolar field lines have stretching angles near 90° in the plane of symmetry through the equatorial region. The stretching angle decreases moving along the field line away from the equatorial region. In the stretched field of the various storm phases, the stretching angle decreases more steeply away from the 90° plane as compared to the much slower decrease along dipolar field lines (see, for example, the northward reference model in Figure 14a). The variations in the stretching angle during the storm at a range of magnetotail locations indicated by the dashed vertical lines are shown in Figure 15.

The MHD + RCM simulation predicts strong magnetotail stretching for more than 6 h associated with the WDPS/CDPS despite the low geomagnetic activity and northward IMF conditions. Figure 14b shows *XZ* cross sections of the magnetotail with color-coded magnetic field stretching angle and projected magnetic field lines superimposed to give the reader a feel for how the changes in the magnetic field configuration relate to the distribution of stretching angles. The stretching angle is given by $\theta_{\text{stretch}} = \arctan(B_z/(B_x^2 + B_y^2)^{1/2})$ with the field components in GSM coordinates [cf. *Borovsky and Denton*, 2010]. The cross sections displayed are taken at five different times during the northward IMF interval associated with the solar filament, including the peak of the dynamic pressure, the time of declining pressure following the peak, the interval of the WDPS,

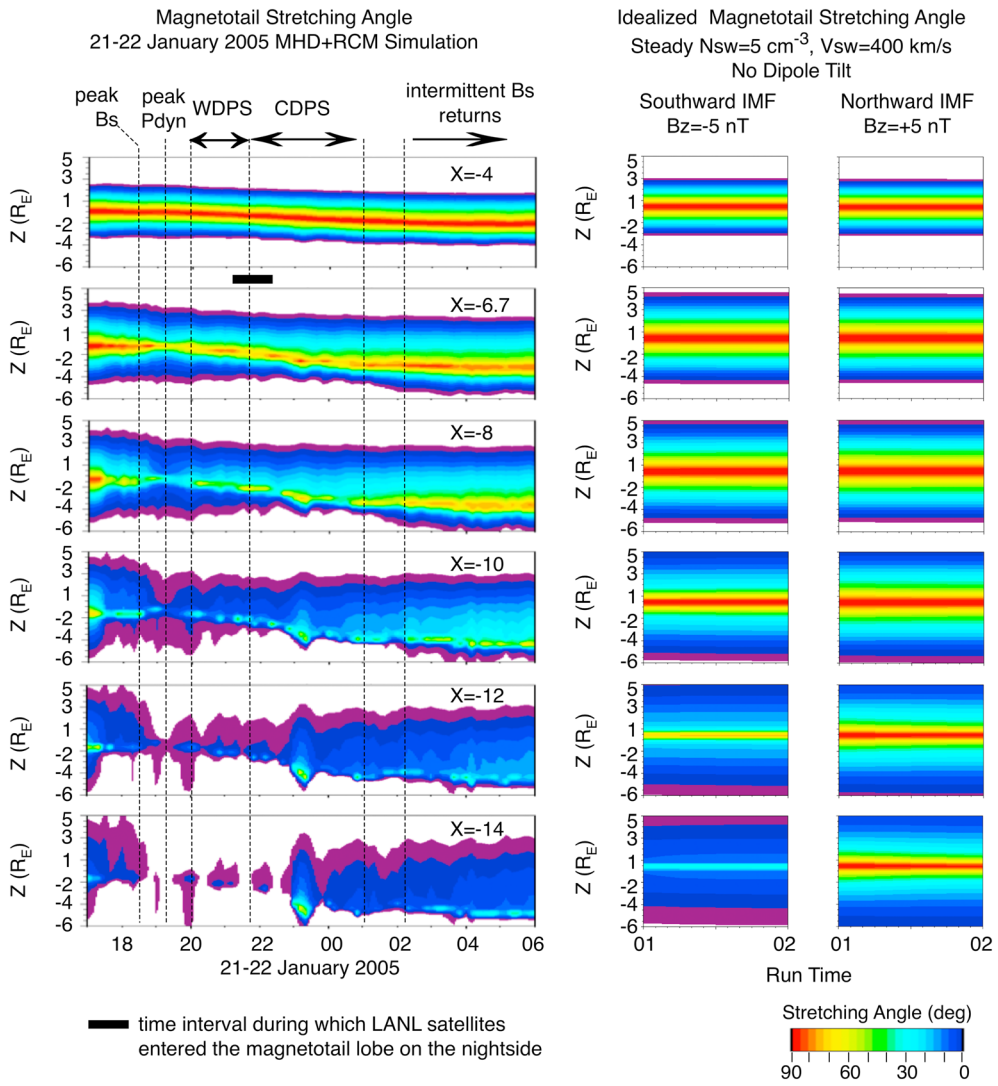

Figure 15. The variations in the magnetic field stretching angle with *Z* at selected locations along the *X* axis as a function of time are displayed from the BATS-R-US + RCM simulation of the 21–22 January 2005 magnetic storm in the left column. The middle and right columns give the stretching angle from reference BATS-R-US + RCM of steady state southward and northward IMF configurations of the magnetic field to show an idealized variation of the stretching angle along the Z-axis under steady state conditions and zero dipole tilt for comparison. Only positive stretching angles associated with closed magnetic field lines are displayed. Magnetotail stretching angles near 90° in the equatorial plane indicate a dipolar configuration; while those near 0° a highly stretched magnetotail configuration.

the lobe encounter, and the CDPS. The sixth cross section is taken from the interval of intermittent southward IMF late in the storm. For comparison purposes, Figure 14a shows the stretching angle from BATS-R-US + RCM steady state reference models of the magnetosphere under GSM northward (IMF $B_z = +5$nT) and southward (IMF $B_z = -5$ nT) IMF conditions, nominal solar wind density (5 cm^{-3}) and speed (400 km/s) and zero dipole tilt.

For a dipole field, the stretching angle is 90° in the magnetic equator, decreasing with latitude away from the equator. Such a condition is also seen in both reference models in Figure 14a. For a field stretched by diamagnetic currents in the equatorial region, the stretching angle is still 90° near the apex of the field line, but the decrease with latitude away from that point is more severe. Such strong stretching is evident in the very low values of the stretching angle away from the field line apex in all of the intervals illustrated in Figure 14b.

In the reference models which contain no dipole tilt, the equatorial plane is aligned with the $Z = 0$ plane. In the inner regions, the magnetic field lines are quite dipolar in both cases. In contrast, on 21–22 January 2005, the plane of 90° stretching angle becomes significantly tilted with respect to the $Z = 0$ plane. Due to the

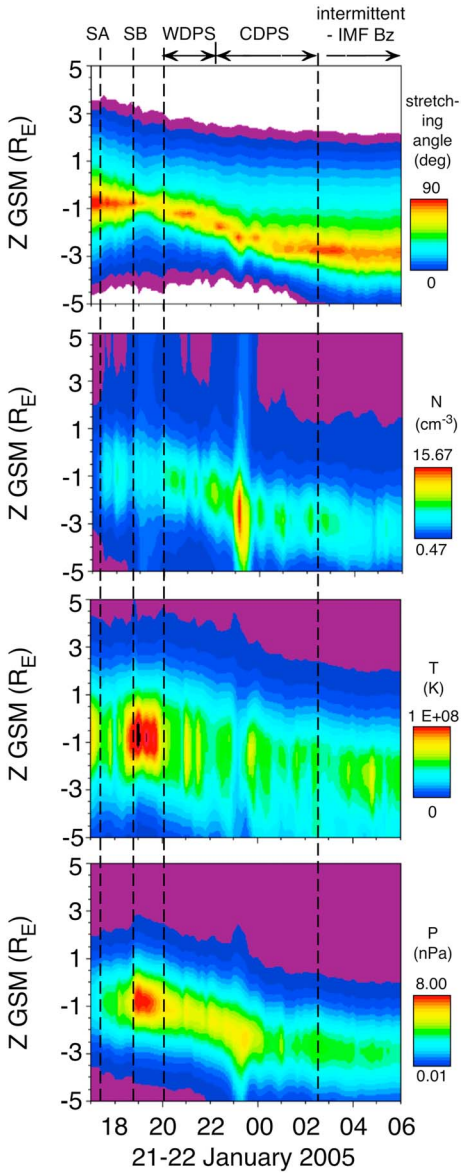

Figure 16. The time evolution of magnetic field stretching angle at midnight MLT, $X = -6.7\ R_E$, and Z spanning $\pm 5 R_E$ is reproduce here along with corresponding plots of the plasma sheet density, temperature, and pressure generated in the same way. As in Figure 3, vertical dashed lines labeled SA and SB mark the initial shock arrival and the leading edge of the high dynamic pressure associated with the solar filament material. The time intervals of the WDPS/CDPS and of the return of intermittent southward IMF are labeled and delineated by vertical dashed lines. The high densities and low temperatures of the WDPS/CDPS appear in sharp contrast to the low densities and high temperatures of the plasma sheet in response to the high dynamic pressures at the leading edge of the solar filament material. However, both intervals produce high dynamic pressures in the plasma sheet and corresponding decreases in the magnetic field stretching angle particularly evident in the intervals 19:10–20:00 UT and 21:30–22:00 UT.

dipole tilt and the effects of solar wind conditions, the magnetic field configuration diverges significantly from a dipole off the equatorial plane.

Figure 15 shows the variation in the magnetic field stretching angle with time at a range of locations ($X = -4.0$, -6.7, -8.0, -10.0, -12.0, and -14.0) in the magnetotail at midnight MLT. At each of these locations (marked by dotted lines in Figure 14), the stretching angle is extracted along the vertical from $Z = 5\ R_E$ to $-10\ R_E$ in order to identify the tilted equatorial plane, the maximum value of the stretching angle which occurs in this plane, and the decrease in the stretching angle away from the equator. These 1-D plots are placed side by side in Figure 15 to create a time history of the changes in the field line configuration. The fact that the maximum value of the stretching angle is less than 90° in these panels is indicative of a "guide field" component, i.e., a nonzero azimuthal field component in the region where the radial component reverses. In these situations, there is no place along the field line where the field lies entirely in the GSM Z direction. Though some degree of magnetotail stretching is evident throughout most of the 21–22 January event despite the dominantly northward IMF conditions, the largest deviations from a dipolar configuration deep within the inner magnetosphere at geosynchronous orbit are seen during two intervals—the first containing the largest dynamic pressures of the solar filament (between 19:10 and 20:00 UT) and the second the increase in stretching as the magnetotail transitions from open to closed driving the change from WDPS to CDPS states of the plasma sheet (between 21:30 and 22:10 UT).

Time histories of plasma density, temperature, and pressure were created in the same manner as described above and compared to the magnetic field stretching angle at geosynchronous orbit in Figure 16 to explore the diamagnetic effects of the WDPS/CDPS. The high plasma sheet densities of the WDPS/CDPS are seen from 20:00 UT to ~03:00 UT the next day consistent with observations by the LANL satellites. Lower densities were found at the time of the solar filament arrival before the WDPS formed and densities dropped again following the CDPS as the IMF turned intermittently southward. High plasma sheet temperatures were associated with the peak in dynamic pressure of the solar filament but dropped to much lower values in the WDPS/CDPS interval (with slightly warmer values during the WDPS than the CDPS). Temperatures began to increase again with the return of southward IMF. The plasma pressures (fourth panel) are directly related to the diamagnetic changes observed in the magnetic field. The large plasma pressures (minimum in the stretching angle) during the solar filament arrival at ~19:10–20:00 UT resulted from the high temperatures despite the low densities in the plasma sheet. However, the cold temperatures and high densities of the WDPS/CDPS also resulted in significant plasma sheet pressures contributing

to changes in the magnetic field configuration. During this time, significant stretching of the geosynchronous equatorial magnetic field appeared along with large deviations from a typical northward IMF configuration at locations off the equatorial plane.

In comparison with these results, *Du et al.* [2008] reported two intervals of strong magnetotail stretching in Geotail observations between 18:51 UT and 20:10 UT, both times within the stretching interval in the simulation associated with the highest dynamic pressures in the solar filament. They roughly identify the first interval of magnetotail stretching with energy storage and the second interval with the release of this stored energy during northward IMF conditions, though they give no specific mechanisms that would accomplish this storage and release scenario.

A recent study of 63 superdense plasma sheet intervals at geosynchronous orbit demonstrated a close correspondence between their appearance during corotating interaction regions as observed by the LANL satellites and increases in magnetotail stretching to a superposed average of 37° observed by five GOES satellites [*Borovsky and Denton*, 2010]. As was demonstrated above, the portion of the field line being sampled depends on the tilt of the magnetic equatorial plane in response to solar wind conditions as well as seasonal variations in the dipole tilt angle. Since the geosynchronous orbit is tilted relative to the magnetic equatorial plane, GOES samples the magnetic field as much as 3 R_E below the $Z=0$ plane on the nightside. The decrease in the stretching angle with distance above or below the equatorial plane evident in both the 21–22 January event and the reference northward and southward IMF cases is consistent with the relatively small stretching angles reported above at geosynchronous orbit, which were compared to typical stretching angles in this region. The superdense ion plasma sheets had superposed average density of ~1.17 cm^{-3} and temperature of 8–10 keV. The reader is reminded that the *superdense* plasma sheets studied by *Borovsky and Denton* [2010] are different than the cold dense plasma sheets (CDPSs) that occur during northward IMF conditions, which are the subject of the present study. The close association between the superdense plasma sheet intervals and strong magnetotail stretching implies that diamagnetic effects associated with the high ion pressures were responsible. The strong stretching during the moderate corotating interaction region-driven storms considered by *Borovsky and Denton* [2010] made on average a 25% contribution to the *Dst* index. The similarity in the stretching between the superdense plasma sheets and the stretching associated with the WDPS/CDPS in the present study implies that magnetotail currents may also contribute to a delay in the recovery of the *SYM-H* index during 21–22 January.

6. Connected Effects Throughout Geospace

Observational evidence that the strong magnetotail stretching predicted by the simulation actually occurred can be found in the increased intensity and the persistent expansion of particle precipitation regions during the same time. Evidence for the increased disruption in ring current shielding during the filament impact and the strong Joule heating that followed in the simulation is provided by the observed unusual electrodynamics of the equatorial ionosphere. Consistency and timing arguments that combine simulation results with the observations identify key coupling processes described below.

6.1. Enhanced Precipitation

As the solar filament arrived at the magnetopause, the low-latitude edge of the auroral oval expanded equatorward to ~55° MLAT and remained expanded for the 6 h of the solar filament passage under northward IMF conditions. Additionally, the peak in ring current precipitation continued to move equatorward and the fluxes to intensify well into this same northward IMF interval.

In the next two sections, we examine how variations in the diffuse aurora and the large-scale 30–2500 keV proton precipitation zones are related to intervals of high dynamic pressure and strong magnetotail stretching on 21 January. As seen in Figure 15, there were two minima in magnetotail stretching angle—one near 19:00 UT at the time of maximum solar wind dynamic pressure and the other after 21:00 UT during the transition between the WDPS open and the CDPS closed magnetotail configurations. By this second interval of magnetotail stretching, the solar wind dynamic pressure had decreased significantly from its peak value, which argues against magnetospheric compression as the dominant source of this later interval of strong magnetotail stretching. During both intervals, the IMF was largely northward. The question arises of whether diamagnetic stretching by the WDPS/CDPS during northward IMF plays a role in the behavior of large-scale precipitation regions.

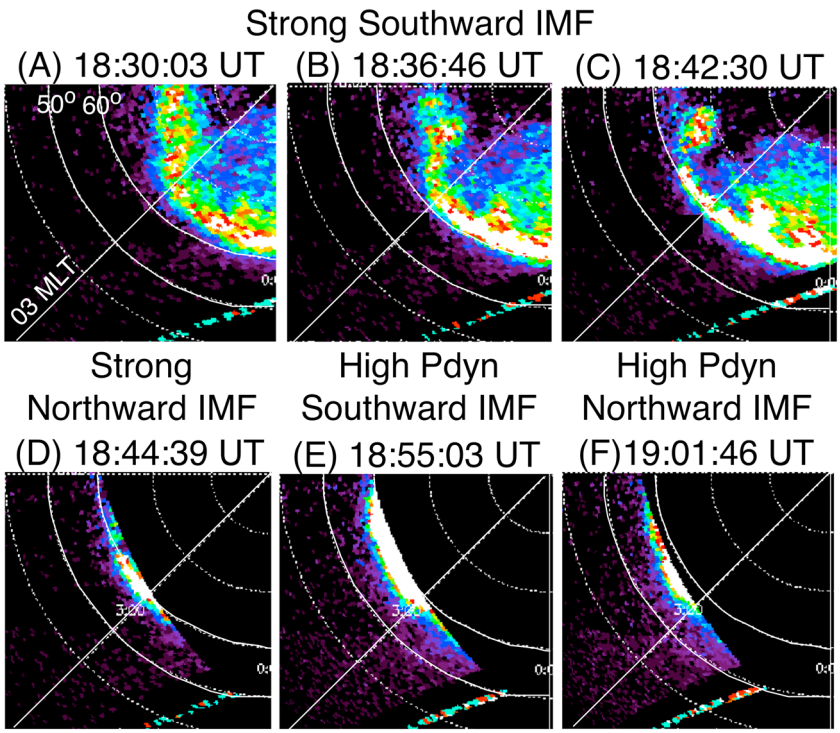

Figure 17. These images of the 00–06 MLT sector from the IMAGE SI13 channel show that the equatorward edge of the auroral oval expanded to ~55° MLAT in association with the arrival of the high dynamic pressure of the solar filament and not with the strong southward IMF in the ICME sheath. The equatorward edge of both the proton and electron auroral ovals remained at these low MLATs for 6 h as the solar filament passed by the Earth.

When the magnetotail fields become stretched, nonadiabatic particle motions are important. Changes to the first adiabatic invariant, μ, result when the minimum magnetic field line curvature near the equatorial plane becomes comparable to the particle gyroradius. This is called field line curvature (FLC) scattering [*Birmingham*, 1984; *Delcourt et al.*, 1994; *Anderson et al.*, 1997; *Young et al.*, 2002, 2008]. The earthward extent of FLC scattering moves to lower radial distances for increasing proton energy, increasing magnetic activity given by *Kp*, and increasing ion mass at a fixed energy [*Anderson et al.*, 1997]. The transition between isotropic and anisotropic proton precipitation observed on satellites in low-Earth orbit on the nightside has been demonstrated to define the earthward extent of large-scale FLC scattering regions [cf. *Sergeev et al.*, 1993].

It is generally accepted that the equatorward edge of the proton diffuse aurora marks the transition between stretched and dipolar magnetic field lines. Scattering of electrons by this same process contributes to the diffuse electron aurora [*Sergeev and Malkov*, 1988] but, in addition, electron interactions with plasma waves at high altitudes can dominate the scattering over certain energy ranges and local time sectors. These wave-electron interactions can also be modified by magnetotail stretching in ways that enhance precipitation in the presence of stretched magnetic field lines [*Ni et al.*, 2011]. As a result, the location in magnetic latitude of the equatorward edges of both the electron and proton auroral ovals is thought to provide visual indicators of the degree of magnetotail stretching [*Weiss et al.*, 1997].

Analogously, large zones of ion precipitation at ring current and radiation belt energies ($>$30 keV), which move inward and increase in intensity during magnetic activity, are attributed to FLC scattering [*Sergeev et al.*, 1983, 1997; *Newell et al.*, 1998]. These large scale regions are separated mostly by energy range from the proton auroral precipitation also thought to result from FLC scattering. However, the lower energy auroral protons scatter farther tailward in the stretched fields of the central plasma sheet. FLC scattering of protons and oxygen ions at ring current and radiation belt energies continues to much lower *L* values, and thus, precipitation zones move deeper into the midlatitude region equatorward of the auroral oval [cf. *Anderson et al.*, 1997]. Integrated global precipitation created by FLC scattering is thought to be an important loss for the ring current during magnetic storms [*Kozyra et al.*, 1998; *Ebihara et al.*, 2011] but has not yet been observationally characterized well partly due to difficulties in separating auroral from ring current precipitation.

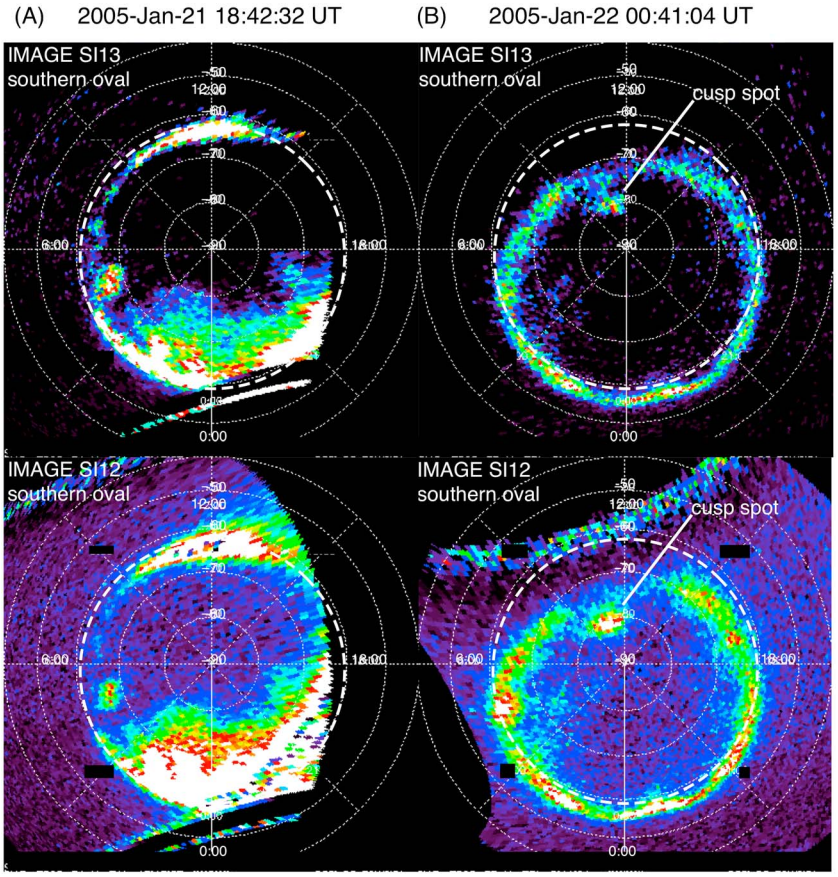

Figure 18. Images of the expanded auroral oval observed by the FUV (top) SI-13 imager and the (bottom) SI-12 imager on the IMAGE satellite are shown. On the left side is an image taken on 21 January 2005 at 18:42 UT during southward IMF in the sheath region of the ICME. On the right is an image on 22 January 2005 at 00:41:04 UT after the IMF had been dominantly northward for more than 5 h. The cusp spot is a signature of northward IMF conditions. For comparison, the yellow dashed line gives the equatorward edge of the diffuse auroral oval during the storm-time peak in southward IMF at 18:36 UT.

6.1.1. Diffuse Aurora

On 21 January, the Imager for Magnetopause-to-Aurora Global Exploration (IMAGE) satellite observed the auroral oval expand rapidly equatorward as the leading edge of the solar filament struck the magnetosphere. Figure 17 shows images of the auroral oval from the SI13 channel of the far ultraviolet (FUV) instrument in the Southern Hemisphere dawn sector. Figures 17a–17c were taken prior to the arrival of the solar filament during the strongest IMF B_z of the storm. The equatorward edge of the auroral zone was located at ~60° MLAT under these conditions. The imaging sequence was terminating so only the lowest latitude edge of the auroral oval was captured between 18:44 and 19:03 UT. These partial images contribute important information on the timing of the auroral oval expansion. Figure 17d was taken during a short interval of strong northward IMF prior to the filament arrival. The equatorward edge was still at ~60° MLAT. Figure 17e was taken just after the arrival of the solar filament during a short interval of southward IMF at its leading edge. Immediately, the lowest latitude edge of the diffuse aurora expanded equatorward to 55°. During Figure 17f, dynamic pressures were near peak values but the IMF had turned weakly northward. However, the equatorward edge remained at 55°. These observations suggest that the initial expansion of the auroral oval was due to the high dynamic pressure in the solar filament, which compressed the magnetotail into a strongly stretched configuration. Over the course of the next 6 h and despite the change to northward IMF conditions and the decrease in dynamic pressure, the equatorward edge remained at these low magnetic latitudes. During this time, auroral activity was weak as indicated by the *AL* index in Figure 3.

Figure 18 compares the auroral ovals observed by the IMAGE satellite in UV emissions produced by precipitating auroral electrons (top) and auroral protons (bottom) at (a) the time of strongest southward IMF during the

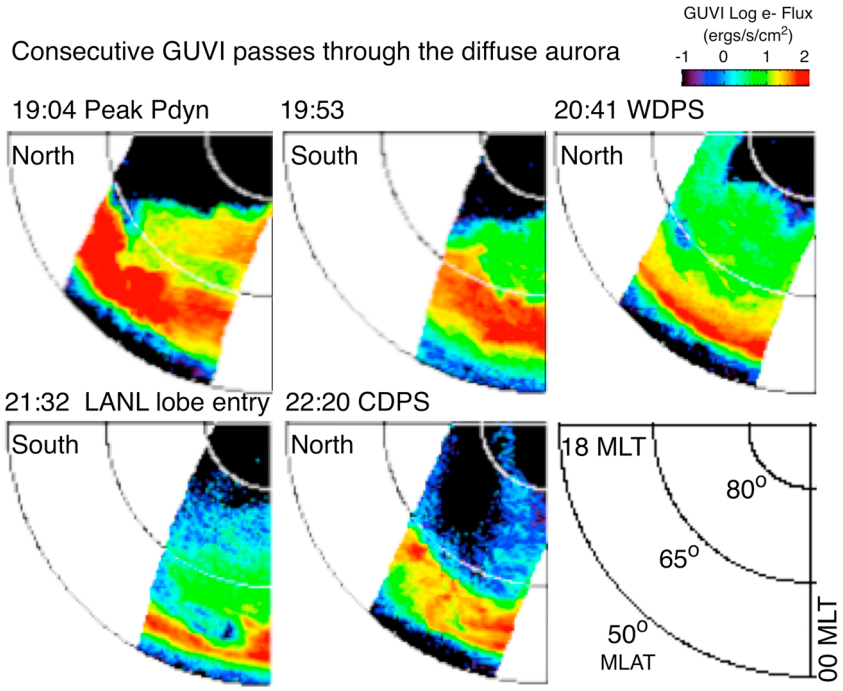

Figure 19. The 18–24 h local time sector is extracted from GUVI maps of the average flux of precipitating electrons to more easily compare the movement of the equatorward boundary of the auroral oval over this interval. The edge of strongest electron fluxes moves to the lowest magnetic latitudes during the two intervals of peak magnetotail stretching (1) at 19:04 UT during the peak dynamic pressures of the solar filament material and (2) at 21:32 when the IMF rotated more purely northward, the magnetotail closed stretching out to $> 150\ R_E$ and the nightside LANL geosynchronous satellites entered the magnetotail lobe.

storm main phase and (b) 6 h later during strongly northward IMF conditions. During this long interval of northward IMF, the equatorward edge of the diffuse auroral oval remained expanded to MLAT ~ 55°.

To separate out the effects of the high solar wind dynamic pressure from those of the CDPS in producing the magnetotail stretching, Figure 19 examines the changes in the equatorward boundary of the electron fluxes in the Global Ultraviolet Imager (GUVI) images during consecutive passes through the diffuse auroral region near midnight. In Figure 19, the dusk-to-midnight local time sector is extracted from electron flux maps. These are then laid side by side so the location of the near-midnight equatorward boundary can be easily compared between images. The edge of strongest (red) electron fluxes moves to the lowest magnetic latitudes during passes centered at 19:04 UT and 21:30 UT. The first excursion of the electron fluxes to their lowest MLAT extent coincides with the arrival of the solar filament and the associated peak in solar wind dynamic pressure. The second coincides with the appearance of the WDPS/CDPS at geosynchronous orbit after the solar wind dynamic pressure had already significantly decreased. This provides evidence that both the high dynamic pressures in the solar wind and then later the WDPS/CDPS contributed to the magnetotail stretching and the equatorward movements of the diffuse aurora.

6.1.2. High-Energy Proton Precipitation Zones

Figure 20-1 presents 3 h global maps of 30–2500 keV proton precipitation during the 21–22 January 2005 magnetic storm. The time at the top of each map is the center of the time interval. These global proton precipitation maps were generated by combining observations from the Medium Energy Proton and Electron Detectors (MEPED) on board three NOAA POES satellites, NOAA-15, 16, and 17. The NOAA POES satellites are in Sun-synchronous circular orbits at ~850 km altitude. Figure 20-2 illustrates the invariant latitudes and magnetic local times covered by each of the satellites in January 2005. The global maps combine observations from four of the MEPED proton energy channels: 30–80 keV, 80–240 keV, 240–800 keV, and 800–2500 keV measuring at 10° to the vertical which is well within the loss cone above 50° *IL*. The observations were sorted into 1° corrected magnetic latitude (CML) and 8 min magnetic local time (MLT) bins. Interpolations were used to fill in missing MLT data within each CML interval. More details about the techniques used to construct the global maps are given in *Fang et al.* [2007].

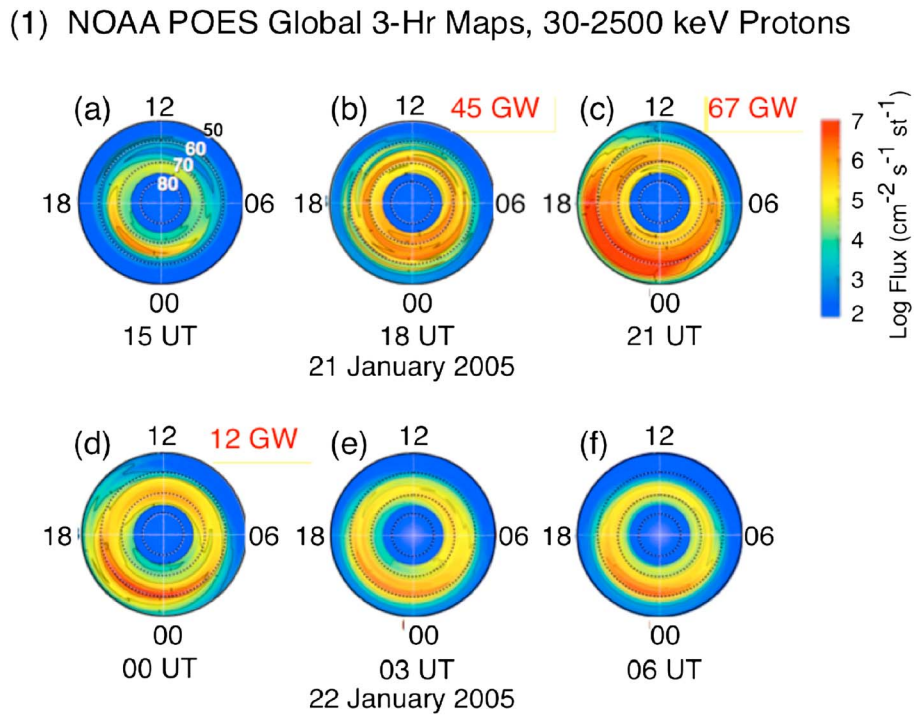

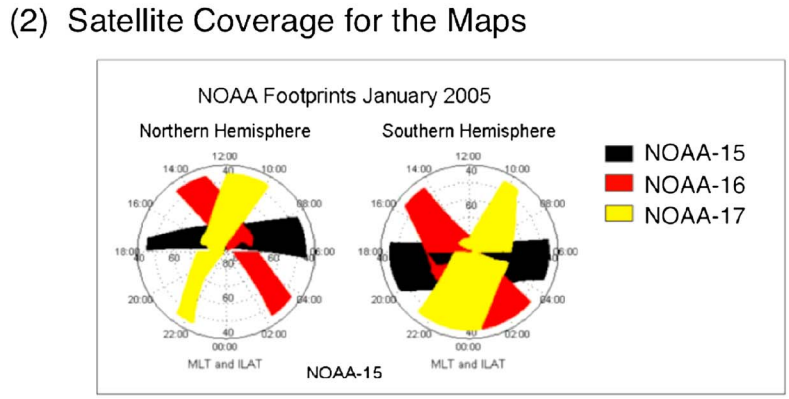

Figure 20. (a) Three hour maps of 30–2500 keV proton precipitation observed by the NOAA-15, 16, and 17 satellites are given at selected times throughout the 21–22 January 2005 magnetic storm. (b) The coverage of the NOAA POES satellites is shown. The maximum proton energy input at 21:00 UT occurs during the northward IMF interval of the solar filament. Proton precipitation intensifies and moves equatorward during this interval compared to the time of the ICME sheath region in which strong southward IMF drove the storm development.

Figure 20-1a shows proton precipitation prior to the start of the magnetic storm from 13:30 to 16:30 UT. The peak of the ring current proton precipitation in the map is located at ~64° MLAT (dipole *L* value ~ 5.2) and at ~22 h MLT. This agrees well with the location of the ring current pressure peak in the MHD + RCM simulation prior to the storm onset. Figure 20-1b covers the time interval 16:30–19:30 UT including the shock hit, storm onset, the ICME sheath passage, and the interval of peak dynamic pressure in the leading portion of the solar filament. The total energy flux of precipitating protons is 45 GW. There are two spatial peaks in the subauroral proton precipitation both within the interval 55°–63° MLAT (dipole *L* ~ 3.0–4.9). Figure 20-1c covers 19:30–22:30 UT which includes both the warm and cooler superdense plasma sheets. Despite the northward IMF conditions at this time, the peak of the proton precipitation moves deeper into the inner magnetosphere between Figures 20-1b and 20-1c reaching an equatorward extent of at least 50° MLAT.

This same inward motion is also found by following the location of peaks in proton precipitation on individual orbits of NOAA POES. The most equatorward penetration of precipitating protons was observed on NOAA-17

at 21.6 MLT near 21:53 UT and on NOAA-16 at 2.3 MLT near 20:41 UT, both in the Northern Hemisphere. These are both at the time of maximum magnetotail stretching associated with the development of the WDPS/CDPS.

Maximum $>$ 30 keV proton precipitation was observed near the time when the solar wind dynamic pressure was largest. After that, the proton precipitation decreases roughly in accordance with the pressure. The auroral proton precipitation at 0.1–20 keV had roughly the same time evolution. The most important feature is that intense precipitation continued and even intensified after the IMF turns northward. Peak fluxes appeared at 20–21 UT on all three satellites confirming the unusual timing of the storm maximum during the northward IMF interval of the ICME.

The total energy flux in precipitating 30–2500 keV protons for Figure 20-1c is 67 GW or 4.2×10^{26} keV/s. This is under predominantly northward IMF conditions. *SYM-H** at 21:00 UT in Figure 3e is ~ -120 nT, which corresponds to a total ring current energy content of 3.0×10^{31} keV using the Dessler-Parker-Sckopke relation [*Dessler and Parker*, 1959; *Sckopke*, 1966]. If this integrated precipitation loss was entirely from the ring current, it would deplete the ring current energy in less than 20 h. As a point of comparison, precipitation losses during the 8–9 February 1986 superstorm with min *Dst* ~ -300 nT reached estimated values near 1×10^{27} keV/s or 160 GW in the early recovery phase just after the peak of the storm [*Kozyra et al.*, 1998].

In Figure 20-1d (22:30–01:30 UT), the proton precipitation zone still extends to 50° MLAT but the precipitating flux is considerably weaker. The total energy flux in precipitating protons has dropped to 12 GW. These observations placed in a global context using the MHD + RCM simulation indicate that magnetotail stretching caused by the WDPS/CDPS is a likely cause for the equatorward motion of the large-scale proton precipitation zones.

There is a remarkable correspondence between the regions of strong ionospheric electric fields on the nightside in the simulation and the observed location and extent of 30–2500 keV proton precipitation zones in Figure 20. Figure 21 compares a 3 h map of the proton precipitation centered at 21:00 UT to the ionospheric electric field (Figure 21b), the polar cap potential pattern (Figure 21c), and the Joule dissipation (Figure 21d) from the simulation at this same time. The right column is from the MHD-only simulation and the left column from the MHD + RCM simulation. A comparison between the columns shows that the strong electric fields across the nightside are produced by the ring current. They are not present in the MHD-only run.

These ionospheric electric fields from the MHD + RCM simulation are produced by partial closure of the ring current-associated region 2 FACs through the region of low conductance equatorward of the electron auroral oval on the duskside [cf. *Ridley and Liemohn*, 2002]. The agreement between the location of these strong electric fields and the location of the proton precipitation is particularly interesting given that no information from the NOAA POES observations was used as input to the global models.

The potential distribution from the MHD + RCM simulation (Figure 21c, left) shows a single lobe cell driven by antiparallel poleward-of-cusp reconnection during weak northward IMF conditions with large IMF B_y component as described in *Reiff and Burch* [1985]. Superimposed on this cell is a secondary negative potential peak spanning from the equatorward edge of the auroral oval to subauroral latitudes associated with the partial ring current closure. The simulation agrees closely with average characteristics of the observed ring current-associated potential peak and westward convection described in *Foster and Vo* [2002] termed a subauroral polarization stream (SAPS). SAPS potentials typically span the subauroral region from the nightside to the early morning sector for all *Kp* values greater than 4. On 21 January at 21:00 UT, *Kp* was 7^+ falling from a *Kp* of 8 in the previous 3 h interval. In agreement with observations, the simulated SAPS convection (perpendicular to the electric fields) spans the equatorward gradient in the potential pattern. The bottom plots (Figure 21d on the left for the MHD + RCM run and on the right for the MHD-only run) shows the Joule dissipation. The SAPS electric fields are associated with a broad in local time premidnight region of weak Joule dissipation.

NOAA POES also observes energetic neutral atoms (ENAs) at ring current energies in a belt encircling the Earth at low-altitude in the equatorial region (not shown). This belt is referred to as the Storm Time Equatorial Belt (STEB) [*Søraas et al.*, 2002, 2003]. The ENA flux directly reflects the number of ring current protons along the line of sight in the equatorial plane. As a consequence, the extent in local time and the intensity of the ENA fluxes supply important information about the ring current and its development [cf. *Søraas and Sørbø*, 2013] that is not masked by other current systems or dynamic pressure variations as

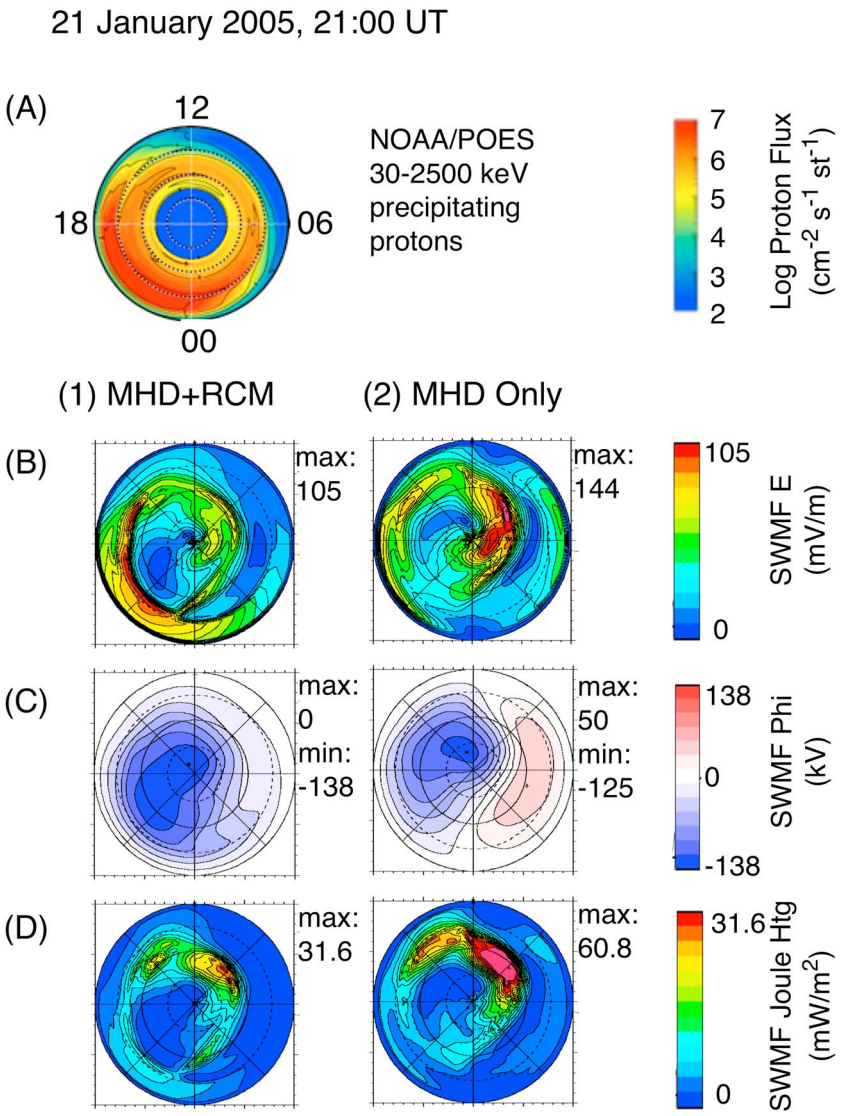

Figure 21. (a) Comparison is made between the global pattern of proton precipitation derived by combining observations of NOAA-15, 16, and 17 over a 3 h interval centered at 21:00 UT on 21 January 2005 and signatures of the ring current electrodynamics in the (1) MHD + RCM simulation and (2) MHD-only simulation. The simulation outputs include the (b) ionospheric electric field, (c) the electric potential pattern (Phi), and (d) the Joule heating rate. Electric fields and the potential pattern are seen in the dusk to postmidnight sector at low latitudes in the MHD + RCM simulation that result from the closure of the partial ring current. These same signatures are not seen in the MHD-only simulation, which did not generate a significant ring current. The location of the ring current signatures in the ionospheric electrodynamics is in close agreement with the location of the observed ring current precipitation during northward IMF conditions.

occurs when the *Dst* index is used to monitor ring current behavior. On 21 January 2005, ENA fluxes from the STEB were observed by NOAA-15, NOAA-16, and NOAA-17. The injection into the ring current starts at around 17:10, and there is a larger increase around 18:45–21:00 UT when the large pressure pulse hits the magnetosphere confirming the unusual timing of the ring current maximum fluxes (storm maximum) during the northward IMF interval of the ICME.

6.2. Coupling to the Equatorial Ionosphere

The effects of the solar filament reached all the way into the equatorial ionosphere triggering a brief equatorial superfountain at first impact and later a distortion of the equatorial ionization anomaly (EIA). To understand the linkages with the solar filament, the basic workings of the equatorial ionosphere are described first and then the observations during the storm presented.

6.2.1. The Equatorial Superfountain

During quiet times, because magnetic field lines are horizontal at the equator, eastward electric fields that result from the normal neutral wind dynamo produce upward $E \times B$ drifts there, raising the $F2$ layer to higher altitudes. The uplifted plasma then slips down along slanted magnetic field lines to higher latitudes on either side of the equator under the influence of gravity and pressure gradients forming the EIA—two crests of enhanced ionization one on either side of the magnetic equator near ±20° MLAT. Under disturbed conditions, magnetospheric electric fields (called prompt penetration electric fields) can leak into the equatorial region [cf. *Jaggi and Wolf*, 1973; *Kelley et al.*, 1979; *Spiro et al.*, 1988; *Fejer and Scherliess*, 1995], overwhelming these dynamo fields and amplifying the normal equatorial fountain. Only during superstorms (typically $Dst < -240$ nT) are prompt penetration electric fields strong enough to lift the equatorial $F2$ layer to altitudes of 800–1000 km before the ring current is able to reestablish shielding. Upward drifts can reach more than 1 km/s, total electron content can increase by more than 350% on the dayside, and EIA crests can move poleward as far as 30°–40° from the magnetic equator [*Greenspan et al.*, 1991; *Basu et al.*, 2001; *Huang et al.*, 2005a; *Tsurutani et al.*, 2004; *Mannucci et al.*, 2005; *Basu et al.*, 2007; *Tsurutani et al.*, 2007, 2008; *Astafyeva*, 2009]. Eastward prompt penetration electric fields and upward ion drifts are further strengthened just after sunset by the gradients in ionospheric conductance there. After dusk, photoionization is insufficient to replenish the ionospheric density below the rising $F2$ layer and a deep hole forms in which the ionospheric density can drop by several orders of magnitude from its normal level [cf. *Greenspan et al.*, 1991; *Lu et al.*, 2013]. The DMSP satellite at 840 km altitude actually moves under the $F2$ peak and observes a steep dropout in density at the location of the superfountain in the dusk sector.

The magnetic storm of 21 Jan 2005 produced an array of complex signatures in the equatorial region described by *Zong et al.* [2010] with the Digisonde Global Ionospheric Observatory, *Santos et al.* [2012] in the South American sector, and *Sahai et al.* [2011] in the Latin American sector and global total electron content maps. Between ~17:10 UT and 1845 UT under dominantly southward IMF conditions, enhanced upward ion drifts with an average magnitude of ~67 m/s lifted the ionosphere at Jicamarca, Peru, near the equator from 350 km to 620 km [*Zong et al.*, 2010]. At 19:00 UT, the IMF rotated northward and the $F2$ layer dropped to 515 km altitude at ~120 m/s. The upward drifts increased the height of the $F2$ layer (h_mF_2) and decreased the density at the peak (N_mF_2) at observations sites near the magnetic equator [*Zong et al.*, 2010; *Sahai et al.*, 2011; *Santos et al.*, 2012]. The density decrease was due to the movement of ionization away from the equator in an enhanced equatorial fountain.

Despite the modest size of the 21 January storm, a superfountain developed in the dusk sector in concert with a brief region of southward IMF on the leading edge of the solar filament. Observations along the DMSP F15 satellite track at 834 km altitude are shown in Figure 22. Vertical ion drifts reached nearly 1 km/s centered at the magnetic equator just before 21 h MLT and a deep density trough developed in the same location. Since the penetration of magnetospheric electric fields to low latitudes is driven by variations in the effectiveness of ring current shielding (see review by *Wolf et al.* [2007]), this is an indicator that the ring current shielding properties were significantly modified by the initial impact of the solar filament. The strong southward IMF lasted only about 10 min from ~18:50 to 19:00 UT. Consistent with this, upward ion drifts and associated density dropouts were not seen in transits of the equatorial ionosphere immediately preceding or following this time. Interestingly enough, no response of the equatorial drifts at local times near noon was reported in the dayside observations at Jicamarca [*Zong et al.*, 2010; *Sahai et al.*, 2011; *Santos et al.*, 2012].

To place these local views into more global context, Figure 22 (top) gives total electron content (TEC) produced by the Jet Propulsion Laboratory (JPL) in the time interval 18:45–19:00 UT with Jicamarca indicated by a white star on the west coast of South America. The TEC maps were produced with the Global Ionospheric Maps (GIM) software [*Mannucci et al.*, 1998, 1999] on the basis of ground-based GPS sites and GPS satellite data. On the lower left, an expanded view near dusk is provided including the location of DMSP F15. The deep but short-lived density depletion seen by F15 appears in the TEC map as a rather weak localized decrease in TEC near the magnetic equator intersected on its westward edge by the DMSP satellite.

The ring current shielding properties were calculated by the MHD + RCM simulation during the storm development. Under steady but disturbed conditions, the ring current shields the inner magnetosphere

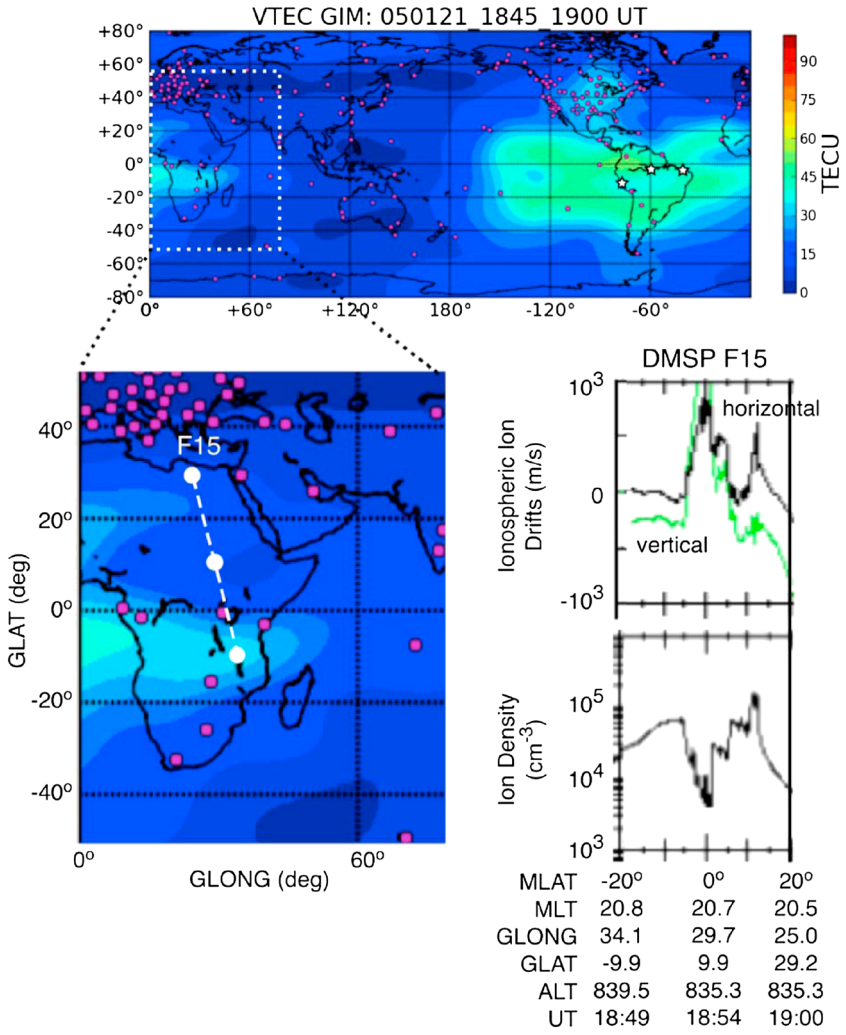

Figure 22. The DMSP F15 satellite, flying near 850 km altitude, crossed the equatorial ionosphere just as the solar filament material hit the front side of the magnetosphere upstream of the Earth. F15 observed rapid (1000 m/s) upward ion drifts and a deep hole in the ionosphere where densities dropped by 2 orders of magnitude from ~1×10^5 cm^{-3} near the edges to ~3×10^3 cm^{-3} in the center. These are characteristic signatures seen when F15 slices through an ionospheric superfountain. However, superfountains appear almost exclusively during intense magnetic storms when strong solar wind electric fields penetrate all the way into the equatorial ionosphere. The 21 January storm was relatively moderate with minimum *SYM-H* ~ −100 nT.

from the full effect of the dawn-dusk magnetospheric convection electric field. But conditions are rarely steady. As the strength of the southward IMF and the convection electric field both increase, the shielding layer provided by the ring current responds by moving earthward. This response time is dependent on the drift time of the ring current particles. During this reconfiguration, the convection electric field is temporarily undershielded and a transient dawn-dusk electric field penetrates into the inner magnetosphere at times all the way to the equator. This PPEF is eastward on the dayside causing upward plasma drifts and westward on the nightside starting at around 21 h MLT [*Fejer and Scherliess*, 1995, 1997] causing downward drifts in the equatorial ionosphere. When the IMF turns northward after an interval of southward IMF, the shielding layer, which was previously configured to shield out a stronger convection electric field, must reconfigure to cancel out a weaker field and temporarily overshields the inner magnetosphere. As a result, a transient dusk-to-dawn electric field penetrates into the equatorial ionosphere from high latitudes and produces downward vertical plasma drifts on the dayside, upward on the nightside. This tendency for overshielding electric fields to occur only when strong northward IMF follows a period of southward IMF and not after a quiet interval was seen in DMSP data [*Huang et al.*, 2010].

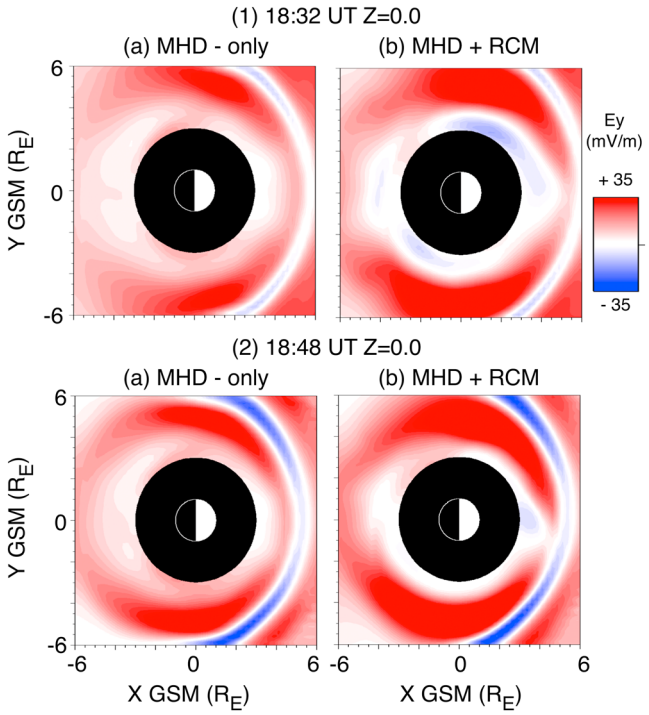

Figure 23. The distributions of Ey in the equatorial plane are shown from the MHD-only (left column) and MHD + RCM (right column) simulations at (1) the time of strongest southward IMF (positive solar wind E_y) and (2) the time of impact with the leading edge of the solar filament also under southward IMF conditions. No significant ring current is present in the MHD-only simulation so a significant amount of the dawn-dusk electric field penetrates through to the inner boundary of the model. In the MHD + RCM simulation, the E_y is partially shielded from the inner magnetosphere by the ring current at 18:32 UT but this partial shielding is disrupted again at the time of the filament impact at 18:48 UT, which creates strong penetration electric fields in the dusk sector (2b).

Figure 23 displays the distributions of E_y in the equatorial plane from the MHD-only (left column) and MHD + RCM (right column) simulations at (1) the time of strongest IMF B_z and (2) the time of impact with the leading edge of the solar filament. The MHD-only simulation produced essentially no ring current, and thus, the shielding of the inner regions was very poor at both times. In the MHD + RCM simulation at the time of maximum IMF B_z (b1), a significant amount of shielding by the ring current had already developed. This shielding was disrupted at the time of the filament impact (b2) allowing regions of $+E_y$ to penetrate to the inner boundary of the model, mapping presumably into the equatorial ionosphere most strongly in the dusk sector. This is consistent with the brief appearance of an ionospheric superfountain at the equator in the dusk sector observed by DMSP F15 at the time of the filament impact.

It has recently been noted that the ability of the ring current to shield out magnetospheric electric fields from the inner magnetosphere and ionosphere is effected by magnetotail stretching [*Fejer et al.*, 1990; *Sazykin*, 2000; *Garner et al.*, 2004]. In simulations, *Maruyama et al.* [2007] found that both the magnitude and duration of the prompt penetration electric field are correlated with magnetotail stretching. The stretching contributes a dusk-to-dawn induction electric field that partially cancels the dawn-to-dusk convection electric field and prevents the shielding layer from moving sufficiently earthward to reestablish shielding. Unlike in these past studies of undershielding, strong magnetotail stretching occurred in the present event but was associated with *northward* IMF, which may have prolonged the interval of overshielding electric fields.

6.2.2. Amplification of the Equatorial Ionization Anomaly

Sahai et al. [2011] and *Santos et al.* [2012] report an unusual development of the EIA on 21 January. In the Latin American sector starting at 20 UT, the height of the peak density in the *F*2 layer (h_mF_2) increased at middle to low latitudes but decreased closer to the magnetic equator. In the South American sector at Fortaleza, Peru, upward drifts of ~50 m/s, starting at 21:30 UT (18:30 LT), raised the *F*2 peak from 300 to 500 km. The upward ion drifts were attributed to an eastward prompt penetration electric field due to strong auroral activity during northward IMF conditions by *Santos et al.* [2012] and to the effects of equatorward winds resulting from Joule heating or possibly a prompt penetration electric field by *Sahai et al.* [2011]. At the equator, downward plasma drifts in response to the westward ionospheric electric field decreased h_mF_2 near Manaus, Brazil [*Sahai et al.*, 2011], but create no significant response at Jicamarca, Peru [*Santos et al.*, 2012].

We investigate the anomalous EIA crest development by placing it into a more global context taking into account conditions throughout geospace. Figure 24 compares TEC observations of the EIA crests on 21 January to those during the 3 days prior at the same UT. The daily *AP* value is given to the right of each map to indicate the level of magnetic activity on each of these days. Though magnetic disturbances on

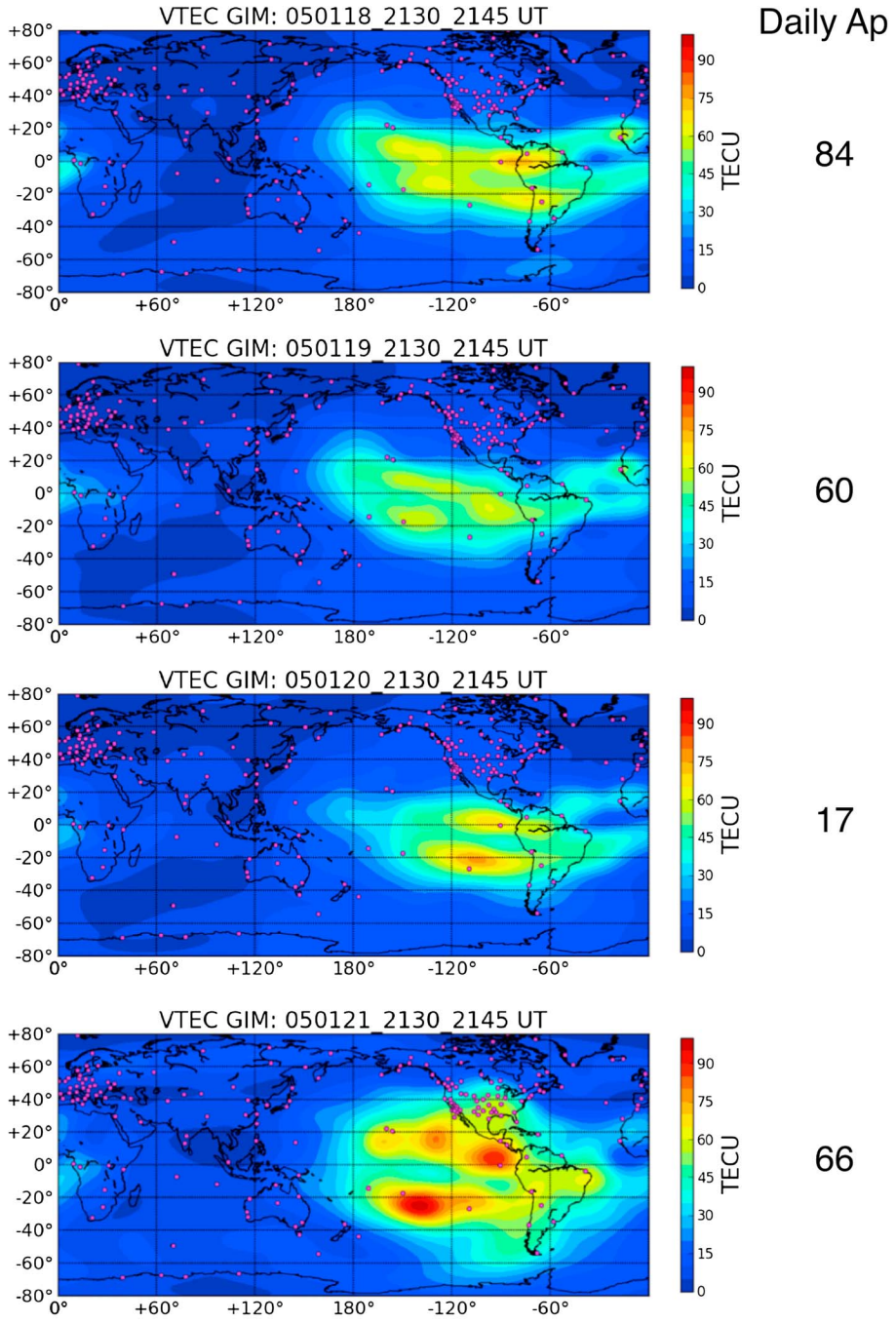

Figure 24. Comparison of the structure of the equatorial ionization anomaly on 21 January 2005 to that on the previous three days. Despite equal or higher levels of magnetic activity on 18 and 19 January, the EIA crests do not exhibit similar behavior to that on 21 January.

18–19 January are comparable to or greater than those on 21 January, the equatorial ionization anomaly does not exhibit the same intensification on those days. The unusual distortion of the EIA occurs during the interval of high dynamic pressure associated with the solar filament and not on other days with similar levels of magnetic disturbance.

To explore the processes responsible for this unusual configuration, additional background information is needed to understand the equatorial dynamics associated with the stormtime disturbance dynamo [cf. *Blanc and Richmond*, 1980; *Scherliess and Fejer*, 1997; *Fejer and Emmert*, 2003], which differ markedly from those of

the PPEF described in the last section. As neutral winds are enhanced by energy inputs during the storm, they blow across magnetic field lines and produce dynamo electric fields that are westward on the dayside and eastward on the nightside—opposite to PPEFs. Timescales for their development are much longer than the nearly instantaneous changes driven by PPEFs.

The thermospheric density responds to high-latitude energy inputs with a delay time of 3–6 h [*Hedin et al.*, 1981]. The statistical delay in the neutral atmosphere response to high-latitude energy inputs near the equatorial region is 3.5–4 h [*Sutton et al.*, 2009], which is consistent with the response of the equatorial electric field to the disturbance dynamo [*Blanc and Richmond*, 1980]. However, neutral wind surges can transmit high-latitude disturbances to the equatorial ionosphere in 1–2 h [*Fuller-Rowell et al.*, 2002]. This is consistent with the time delay between the spike in Joule heating shown in Figure 3g and the start of the changes in the EIA crests.

Equatorward winds push ionization upward along slanted magnetic field lines at middle and low latitudes increasing h_mF_2 and producing an increase in ionospheric density due to the decrease in collisional losses at these higher altitudes [cf. *Lu et al.*, 2012, 2013 and references therein]. Conversely, *poleward* neutral winds push ionization down slanted magnetic field lines increasing collisional losses because of the higher atmospheric densities and thus eroding the ionosphere. However, these neutral wind surges have no effect on the h_mF_2 at the equator since the field lines there are horizontal. Any changes in the h_mF_2 at the equator are due to disturbance electric fields. At off-equatorial latitudes, vertical drifts due to disturbance dynamo electric fields or PPEFs will amplify or oppose the drifts due to neutral winds depending on their relative directions. In the present case, westward electric field due to the disturbance dynamo or an overshielding PPEF or some combination of the two is consistent with the downward movement of h_mF_2 at the equator. An upward movement of h_mF_2 at midlatitudes in response to a disturbance equatorward wind surge is needed to overcome the downward drift produced by the westward electric field and amplify the EIA crests.

Evidence for such an equatorward wind surge is shown in Figure 25 from a TIMEGCM simulation of the thermospheric response to the 21 January 2005 magnetic storm with high-latitude potential patterns, Joule heating rates, and auroral power given by the AMIE procedure. The TIMEGCM [*Roble and Ridley*, 1994; *Roble*, 1995] is a global model of the mesosphere-thermosphere-ionosphere system, extending from ~30 km to about 500 ~ 800 km altitude (depending on solar activity). It has a nominal resolution of $5° \times 5°$ in latitude and longitude and one-half scale height in the vertical, with a total of 49 constant pressure levels. The model incorporates aeronomical, dynamical, and electrodynamical processes that are appropriate for these regions. The lower boundary of the TIMEGCM is specified by climatological tides based on the Global Scale Wave Model (GSWM) [*Hagan and Forbes*, 2002, 2003]. In addition, daily averaged observations from the National Centers for Environmental Predictions (NCEP) analysis are used to represent other longer wavelength atmospheric forcing. The upper boundary inputs to the model include the solar UV and EUV fluxes, energetic particle precipitation, and ionospheric electric fields. The AMIE cross-polar cap potential and Joule heating rates are shown in Figures 3f and 3g, respectively. The magnitude of the total Joule heating rate is consistent with a similar calculation presented in *Sahai et al.* [2011].

In Figure 25, a comparison is given between (1) the timing and development of a neutral wind surge in the simulation powered by the observed spike in Joule heating and (2) the intensification of the equatorial ionization anomaly (EIA) seen in TEC at the same time. Heating of the neutral atmosphere in a localized region on the dayside (1a and 1b) in the simulation, creates a neutral wind surge (1c) that reaches the equator from both hemispheres by 20:00 UT (1d). Equatorward winds from the Southern Hemisphere cross over the equator and become poleward winds in the Northern Hemisphere by 22:00 UT (1f). With a small time delay but by 23:00 UT, strong poleward winds also develop in the Southern Hemisphere (1g). The timing and location of the heating and wind surges are consistent with the features in the development of the EIA seen in vertical TEC (VTEC) observations. A region of enhanced VTEC localized over North America at midlatitudes (2a) develops in association with the initial localized temperature increase in the neutral atmosphere due to Joule heating. As the neutral wind surges reached the equator from both northern and southern high-latitude regions, ionization in the EIA crests is pushed up slanted field lines, increasing the density (2b). Densities reached maximum values in the crests by 21:40 UT (2c). The density in the EIA crest in the Northern Hemisphere began to decrease as equatorward winds in the Southern Hemisphere crossed the equator and became poleward winds in the Northern Hemisphere. Plasma is now blown down slanted field lines to lower altitudes where losses are greater (2d) and the densities in the northern

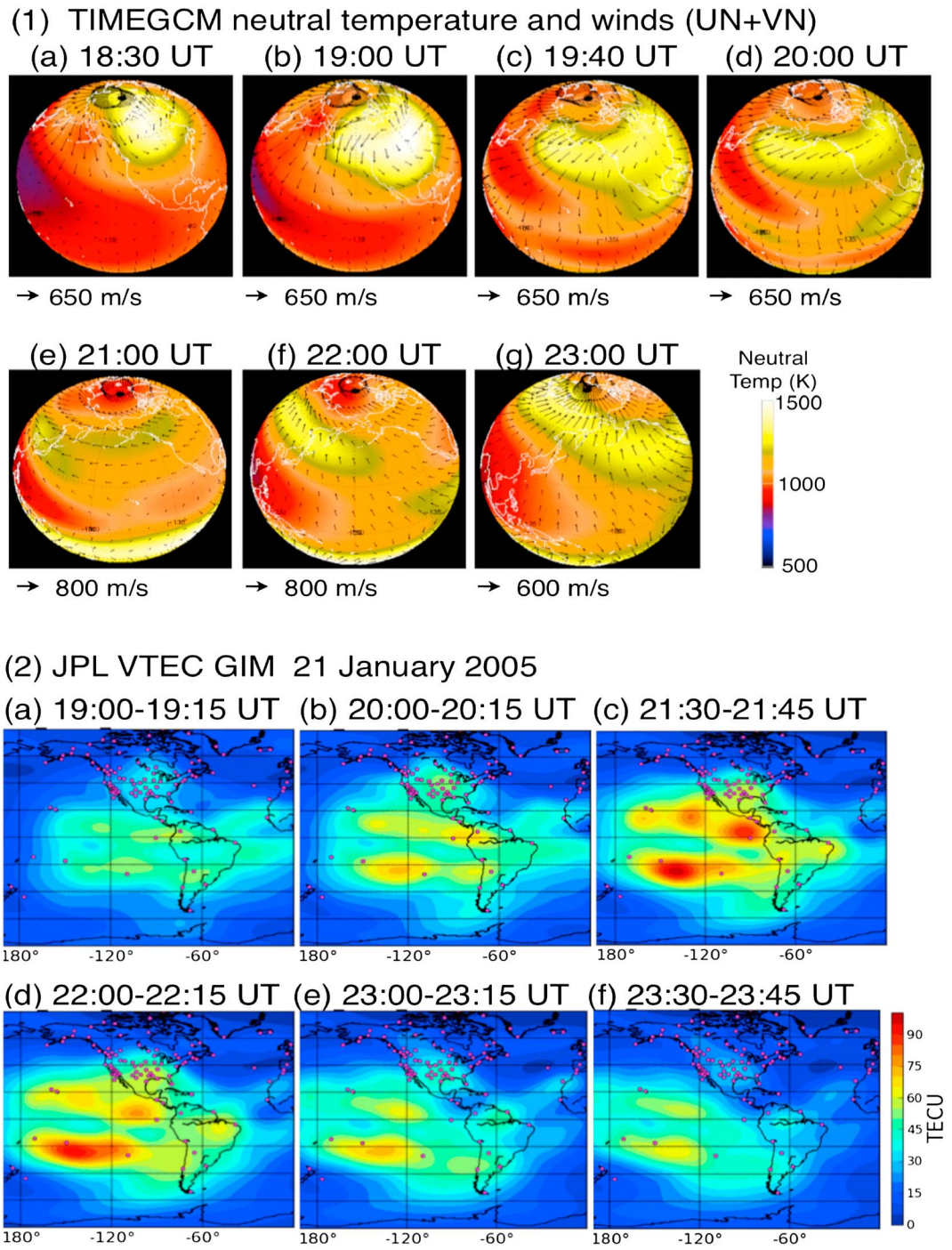

Figure 25. A comparison is given between (1) an equatorward neutral wind surge (1a–1e) driven by a spike in Joule heating shown in neutral temperature and winds from the TIMEGCM model and (2) anomalous development of the equatorial ionization anomaly crests shown in global JPL TEC maps as the wind surge reaches the equator (2b and 2c). The neutral wind drives plasma up slanted field lines to higher altitudes where loss rates are diminished increasing the density in the crests. The equatorward wind passes over the equator and become poleward wind in the opposite hemisphere (1f and 1g) driving plasma down slanted field lines and decreasing the density in the crests (2d–2f). See text for more details.

EIA crest began to decrease. By 23:00 UT, strong poleward winds in the Southern Hemisphere caused the density of the southern EIA crest to drop some time after the density decrease in the northern crest (2e). By 23:30 UT, the EIA reconfigured to a state resembling that during active conditions in the days prior to the filament arrival (2f).

Although the solar filament material did not arrive in geospace until 18:45 UT, we propose that it influenced the production of all three of the Joule heating peaks. The momentum of the massive solar filament as it traveled through the background heliosphere almost certainly played a key part in sustaining the high velocity of the ICME. High velocities at 1 AU are necessary for producing the unusually strong IP shock at the leading edge of the ICME. The movement of the solar filament forward through the magnetic flux rope also would have increased the compression of the ICME sheath region, intensifying the southward IMF. These structures drove the first two peaks in the Joule dissipation prior to the arrival of the solar filament. Conditions at the leading edge of the solar filament produced the third peak.

7. Summary and Conclusions

The 21 January 2005 magnetic storm is a complex event which exhibited an array of unusual features compared to other storms of similar size. The major question that began the investigation is why does a storm of this modest size contain geospace phenomena seen most usually during superstorms? What are the differences in the space environment over other moderate storms that make this storm behave in some ways like a superstorm and in others ways like a moderate event? What do these departures from what we expect (and normally observe) tell us about the way the geospace system works?

In this paper, we focused on the most direct effects of the dense solar filament on the geospace environment and the consequences in connected regions. Each of these effects can be linked to the exceptional dynamic pressure of the filament or to the capture of solar filament material directly into the magnetosphere. In all cases, the effects are strongly dependent on the orientation of the IMF at the time and on the past history of the solar wind driving. Most importantly, the solar filament arrived after a significant ring current, driven by the southward IMF in the ICME sheath, had already formed.

1. The initial solar filament impact under southward IMF conditions produced a brief (10–15 min) equatorial superfountain in the dusk sector identified on the basis of strong upward ion drifts approaching 1 km/s at 835 km altitude spatially coincident with more than an order of magnitude drop in ionospheric density observed by DMSP F15. At the same time, the disruption in the ring current shielding reached its maximum in the MHD + RCM simulation in the dusk sector. No signature of this intensification in prompt penetration electric fields was observed at ground-based stations closer to noon MLT, which implies that gradient in electrical conductance near dusk was an important factor. Superfountains occur during only the most intense magnetic storms and are surprising in a more moderate event like the 21 January 2005 storm. Equally surprising is the development and decay of a superfountain on timescales of tens of minutes.
2. Under northward IMF conditions, the exceptionally dense solar filament material was captured directly into the magnetosphere to form a cold dense plasma sheet (CDPS). When the filament engulfed the magnetosphere, the density in the magnetosheath rose to ~130 cm^{-3} and the temperature to 1–2 keV. At this point, the IMF rotated northward and double high-latitude reconnection converted magnetosheath flux tubes filled with solar filament plasma directly into magnetospheric flux tubes, capturing the filament material into the magnetosphere and forming a CDPS. Both the simulation and observations indicate that within 1 h the plasma sheet densities reaching 6 cm^{-3} at midnight in geosynchronous orbit, tens of cm^{-3} at dawn and dusk, and tens to 100 cm^{-3} in the low latitude boundary layer (LLBL) near noon. The double high-latitude capture process produced a closed LLBL so the tens of cm^{-3} plasmas on the dayside are essentially part of the plasma sheet. The simulation, which included the drift physics of the inner magnetosphere, reproduced the characteristics and timing of the CDPS remarkably well based on a comparison with observations by the LANL geosynchronous satellites and Double Star TC-1. These simulations expand upon earlier investigations into the formation of the CDPS by including a fully coupled inner magnetosphere module.
3. The characteristics of the CDPS and the topology of the magnetotail during northward IMF depend on the strength of the IMF B_y component. Initially, the IMF B_y was large and the magnetotail was open. When the IMF rotated to purely northward, the magnetotail closed, stretched out to over 150 R_E in length, and then snapped back to ~ 60 R_E for the remainder of the ICME. Correlated with these topological changes, the temperature of the CDPS transitioned from warmer to cooler. These plasma sheet states were labeled WDPS and CDPS, respectively, to emphasis this change in temperature.

4. Two intervals of strong magnetotail stretching developed in the simulation. The first was a response to the arrival of the high dynamic pressures in the solar filament. The stretching diminished as the pressures decreased from peak values. However, simultaneous with the appearance of the WDPS/CDPS at geosynchronous orbit, a second interval of strong magnetotail stretching developed. Magnetotail stretching is generally associated with magnetic activity. However, in this case, the *AL* index indicated a low level of magnetic activity. Despite being cold, the high filament densities produced sufficient pressure to inflate the low-latitude boundary layer as a result of diamagnetism and supply stretched flux tubes to the magnetotail plasma sheet from both flanks.
5. The stretched magnetotail was accompanied by an expanded diffuse auroral region in both ions and electrons that persisted throughout the 6 h of the filament passage, and by an intensification and equatorward movement of 30–2500 keV proton precipitation zones. Both of these phenomena have been associated with magnetotail stretching through the magnetic field line curvature (FLC) scattering of energetic ions and electrons. Two intervals of strong magnetotail stretching in the simulation were correlated with equatorward movements of the boundary of auroral precipitation. The first, observed by IMAGE FUV, corresponded closely with the onset of the high solar wind dynamic pressures in the filament. However, images of the auroral oval from TIMED GUVI, and measurements of precipitating high-energy ions and electrons during passes of the NOAA satellites indicate a second equatorward excursion of the auroral and high-energy precipitation, respectively, at the time of peak magnetotail stretching by the WDPS/CDPS in the simulation.
6. The location of the observed intense proton precipitation coincided remarkably well with the location of the magnetospheric ring current pressure peak in the MHD + RCM simulation identified by the associated potential drop, electric fields, and Joule dissipation in the ionosphere.
7. A broad region of soft electron precipitation was observed equatorward of the cusp and from the dawn to the dusk sector by the FAST and DMSP satellites during the northward IMF interval of the solar filament. The processes responsible for this extended region of precipitation are not investigated here. However, it very likely played a role in the anomalous expansion of the neutral atmosphere observed by the CHAMP and GRACE satellites during this storm [*Sadler et al.*, 2012].
8. Joule heating rates in the cusp region were amplified to superstorm levels by the strong IMF B_y, high dynamic pressure, and fast solar wind speeds. The strong IMF B_y and high dynamic pressures at the leading edge of the filament in combination with fast solar wind flows (near 900 km/s) drove exceptionally strong Joule heating rates (reaching up to 174 mW/m^2) in and around the cusp regions.
9. Lastly, an intensification of the equatorial ionization crests appeared during this period that was not seen previously in a similarly active 2 day period just before the 21 January event. The timing suggests that an equatorward neutral wind surge in response to the extreme impulsive Joule heating events in the cusp was a significant driver of the equatorial electrodynamics, pushing ions up slanted magnetic field lines to higher altitude and decreasing recombination losses. The simultaneous downward drifts observed at the magnetic equator occurred during a persistent interval of overshielding prompt penetration electric fields in the MHD + RCM simulation associated with magnetotail stretching during northward IMF. This raises questions about the role of magnetotail stretching by cold superdense plasma sheets in maintaining ring current overshielding. In this interval, the relative contributions of disturbance dynamo and overshielding prompt penetration electric fields are still an open issue.

These phenomena provide insights into some of the ways that high dynamic pressure amplifies geomagnetic disturbances. Remarkably all these features, closely coupled to each other and to the solar filament, occurred during a dominantly northward IMF interval, normally associated with magnetic quieting. Evidence suggests that some of the largest and most damaging geospace disturbances including the Carrington event of 1859 [*Tsurutani et al.*, 2003; *Manchester et al.*, 2006; *Li et al.*, 2006] and the 4–5 August 1972 event [*Vaisbert and Zastenker*, 1976; *d'Uston et al.*, 1977], which disrupted a major communications system in the United States [*Boteler and van Beek*, 1999], also contained dense plasma traveling directly behind the ICME sheath region toward Earth.

References

Anderson, B. J., R. B. Decker, and N. P. Paschalidis (1997), Onset of nonadiabatic particle motion in the near-Earth magnetotail, *J. Geophys. Res.*, *102*(A8), 17,553–17,569, doi:10.1029/97JA00798.

Astafyeva, E. (2009), Effects of strong IMF B_z southward events on the equatorial and mid-latitude ionosphere, *Ann. Geophys.*, *27*, 1175–1187.

Bame, S. J., et al. (1993), Magnetospheric plasma analyzer for spacecraft with constrained resources, *Rev. Sci. Instrum.*, *64*, 1026.

Basu, S., K. M. Groves, H.-C. Yeh, S.-Y. Su, F. J. Rich, P. J. Sultan, and M. J. Keskinen (2001), Response of the equatorial ionosphere in the South Atlantic region to the great magnetic storm of July 15, 2000, *Geophys. Res. Lett.*, *28*, 3577–3580, doi:10.1029/2001GL013259.

Acknowledgments

The authors would like to thank the sources of funding for this study: NASA grants NAG5-10297 and NAG-10850, NNX10AQ34G, NNX09AI04G, and NSF grants ATM-0090165 and ATM 0903596. A portion of this research was performed at the Jet Propulsion Laboratory, California Institute of Technology under contract with NASA. The work at NCAR was supported in part by the NASA USPI-GOCE project under subcontract 1549222 and by the NASA Heliophysics Guest Investigators program under grant NNH09AK621. NCAR is sponsored by the National Science Foundation. Helpful discussions with A. F. Nagy and G. Rostoker are gratefully acknowledged. The authors would also like to thank all of their data providers. Simulations used in this work are available through the Community Coordinated Modeling Center's run archive at http://ccmc.gsfc.nasa.gov/results/index.php under the identifiers Derek_Andeweg_111608_1 and Derek Andeweg_111608_2, and runs with outputs at a 1 min cadence (Derek_Andeweg_111608_1a and Derek Andeweg_111608_2a) are also available on request. Special thanks is given to the developers of the VISBARD visualization software, the CSEM team for use of the SWMF global models, and the developers of the Virtual Modeling Repository (VMR). The ACE, TIMED GUVI, IMAGE HENA, IMAGE FUV, NOAA, LANL MPA, and FAST satellite observations used in this analysis were freely available through OMNIWeb (http://omniweb.gsfc.nasa.gov), CDAWeb (http://cdaweb.gsfc.nasa.gov/cdaweb/), and NASA's Heliophysics Virtual Observatories (http://hpde.gsfc.nasa.gov/hpde_data_access.html). Reprocessed ACE solar wind parameters during intervals of high background radiation during the 21–22 January 2005 storm were provided by Ruth Skoug (LANL) and Heather Elliott (SwRI). Primary access to the DMSP SSJ data was through the APL DMSP data server at http://sd-www.jhuapl.edu/Aurora/spectrogram/index.html, and to the DMSP SSIES data through a data server at the University of Texas at Dallas at http://cindispace.utdallas.edu/DMSP/. Double Star-1 data were accessed through the Double Star Science Data Center at http://www.rssd.esa.int/index.php?project=DOUBLESTAR&page=data_ring and Cluster satellite data through the Cluster Active Archive at http://caa.estec.esa.int/caa/home.xml.

Alan Rodger thanks the reviewers for their assistance in evaluating this paper.

Basu, S., S.-Y. Su, F. J. Rich, K. M. Groves, E. MacKenzie, C. Coker, Y. Sahai, P. R. Fagundes, and F. Becker-Guedes (2007), Response of the equatorial ionosphere at dusk to penetration electric fields during intense magnetic storms, *J. Geophys. Res.*, *12*, A08308, doi:10.1029/2006JA012192.
Bell, J. T., M. S. Gussenhoven, and E. G. Mullen (1997), Super storms, *J. Geophys. Res.*, *102*(A7), 14,189–14,198, doi:10.1029/96JA03759.
Birmingham, T. J. (1984), Pitch angle diffusion in the Jovian magnetodisc, *J. Geophys. Res.*, *89*(A5), 2699–2707, doi:10.1029/JA089iA05p02699.
Blanc, M., and A. D. Richmond (1980), The ionospheric disturbance dynamo, *J. Geophys. Res.*, *85*(A4), 1669–1686, doi:10.1029/JA085iA04p01669.
Borovsky, J. E., and M. H. Denton (2008), A statistical look at plasmaspheric drainage plumes, *J. Geophys. Res.*, *113*, A09221, doi:10.1029/2007JA012994.
Borovsky, J. E., and M. H. Denton (2010), Magnetic field at geosynchronous orbit during high-speed stream-driven storms: Connections to the solar wind, the plasma sheet, and the outer electron radiation belt, *J. Geophys. Res.*, *115*, A08217, doi:10.1029/2009JA015116.
Borovsky, J. E., M. F. Thomsen, and D. J. McComas (1997), The superdense plasma sheet: Plasmaspheric origin, solar wind origin, or ionospheric origin?, *J. Geophys. Res.*, *102*(A10), 22,089–22,097, doi:10.1029/96JA02469.
Borovsky, J. E., M. F. Thomsen, and R. C. Elphic (1998), The driving of the plasma sheet by the solar wind, *J. Geophys. Res.*, *103*(A8), 17,617–17,639, doi:10.1029/97JA02986.
Borovsky, J. E., M. Hesse, J. Birn, and M. M. Kuznetsova (2008), What determines the reconnection rate at the dayside magnetosphere?, *J. Geophys. Res.*, *113*, A07210, doi:10.1029/2007JA012645.
Boteler, D. H., and G. J. van Beek (1999), August 4, 1972 revisited: A new look at the geomagnetic disturbance that caused the L4 cable system outage, *Geophys. Res. Lett.*, *26*(5), 577–580, doi:10.1029/1999GL900035.
Burch, J. L. (2000), Image mission overview, *Space Sci. Rev.*, *91*, 1–14.
Burton, R. K., R. L. McPherron, and C. T. Russell (1975), An empirical relationship between interplanetary conditions and *Dst*, *J. Geophys. Res.*, *80*, 4204, doi:10.1029/JA080i031p04204.
Carlson, C. W., R. F. Pfaff, and J. G. Watzin (1998), The Fast Auroral SnapshoT (FAST) mission, *Geophys. Res. Lett.*, *25*(12), 2013–2016, doi:10.1029/98GL01592.
Carlson, C. W., J. P. McFadden, P. Turin, D. W. Curtis, and A. Magoncelli (2001), The electrons and ion plasma experiment for FAST, *Space Sci. Rev.*, *98*, 33–66.
Cattell, C. A., M. F. Thomsen, J. Kozyra, B. Lavraud, J. Borovsky, and J. Dombeck (2004), Energized banded ions during large geomagnetic storms: Comparisons of observations at geosynchronous and low altitudes, Rep. COSPAR-04-A-02925, Comm. on Space Res, Paris, France.
Christensen, A. B., et al. (2003), Initial observations with the Global Ultraviolet Imager (GUVI) in the NASA TIMED satellite mission, *J. Geophys. Res.*, *108*(A12), 1451, doi:10.1029/2003JA009918.
Clemmons, J. H., J. H. Hecht, D. R. Salem, and D. J. Strickland (2008), Thermospheric density in the Earth's magnetic cusp as observed by the Streak mission, *Geophys. Res. Lett.*, *35*, L24103, doi:10.1029/2008GL035972.
Clilverd, M. A., C. J. Rodger, and T. Ulich (2006), The importance of atmospheric precipitation in storm-time relativistic electron flux drop outs, *Geophys. Res. Lett.*, *33*, L01102, doi:10.1029/2005GL024661.
Clilverd, M. A., C. J. Rodger, R. M. Millan, J. G. Sample, M. Kokorowski, M. P. McCarthy, T. Ulich, T. Raita, A. J. Kavanagh, and E. Spanswick (2007), Energetic particle precipitation into the middle atmosphere triggered by a coronal mass ejection, *J. Geophys. Res.*, *112*, A12206, doi:10.1029/2007JA012395.
Colpitts, C. A., C. A. Cattell, J. U. Kozyra, and M. Parrot (2012), Satellite observations of banded VLF emissions in conjunction with energy-banded ions during very large geomagnetic storms, *J. Geophys. Res.*, *117*, A10211, doi:10.1029/2011JA017329.
Cornilleau-Wehrlin, N., et al. (2005), The STAFF-DWP wave instrument on the DSP equatorial spacecraft: description and first results, *Ann. Geophys.*, *23*, 2785–2801.
Crowley, G., J. Schoendorf, R. G. Roble, and F. A. Marcos (1996), Cellular structures in the high-latitude thermosphere, *J. Geophys. Res.*, *101*(A1), 211–223, doi:10.1029/95JA02584.
Crowley, G., D. J. Knipp, K. A. Drake, J. Lei, E. Sutton, and H. Lühr (2010), Thermospheric density enhancements in the dayside cusp region during strong B_y conditions, *Geophys. Res. Lett.*, *37*, L07110, doi:10.1029/2009GL042143.
Dandouras, I. S., H. Reme, J. Cao, and P. Escoubet (2009), Magnetospheric response to the 2005 and 2006 extreme solar events as observed by the Cluster and Double Star spacecraft, *Adv. Space Res.*, *43*, 618–623.
De Zeeuw, D. L., T. I. Gombosi, C. P. T. Groth, K. G. Powell, and Q. F. Stout (2000), An adaptive MHD method for global space weather simulations, *IEEE Trans. Plasma Sci.*, *28*, 1956–1965.
De Zeeuw, D. L., S. Sazykin, R. A. Wolf, T. I. Gombosi, A. J. Ridley, and G. Tóth (2004), Coupling of a global MHD code and an inner magnetospheric model: Initial results, *J. Geophys. Res.*, *109*, A12219, doi:10.1029/2003JA010366.
Delcourt, D. C., R. F. Martin Jr., and F. Alem (1994), A simple model of magnetic moment scattering in a field reversal, *Geophys. Res. Lett.*, *21*(14), 1543–1546, doi:10.1029/94GL01291.
Dessler, A. J., and E. N. Parker (1959), Hydromagnetic theory of geomagnetic storms, *J. Geophys. Res.*, *64*, 2239, doi:10.1029/JZ064i012p02239.
Du, A. M., B. T. Tsurutani, and W. Sun (2008), Anomalous geomagnetic storm of 21–22 January 2005: A storm main phase during northward IMFs, *J. Geophys. Res.*, *113*, A10214, doi:10.1029/2008JA013284.
Du, A. M., W. Sun, B. T. Tsurutani, R. N. Boroyev, and A. V. Moiseyev (2011), Observations of dawn-dusk aligned polar cap aurora during the substorms of January 21, 2005, *Planet. Space Sci.*, doi:10.1016/j.pss.2011.06.021.
d'Uston, C., et al. (1977), Energetic properties of interplanetary plasma at the Earth's orbit following the August 4, 1972 flare, *Solar Phys.*, *51*, 217.
Ebihara, Y., M.-C. Fok, T. J. Immel, and P. C. Brandt (2011), Rapid decay of storm time ring current due to pitch angle scattering in curved field line, *J. Geophys. Res.*, *116*, A03218, doi:10.1029/2010JA016000.
Echer, E., W. D. Gonzalez, and B. T. Tsurutani (2008), Interplanetary conditions leading to superintense geomagnetic storms ($Dst < -250$ nT) during solar cycle 23, *Geophys. Res. Lett.*, *35*, L06S03, doi:10.1029/2007GL031755.
Elkington, S. R., M. K. Hudson, and A. A. Chan (2003), Resonant acceleration and diffusion of outer zone electrons in an asymmetric geomagnetic field, *J. Geophys. Res.*, *108*(A3), 1116, doi:10.1029/2001JA009202.
Engelhardt, W. (2005), Is a plasma diamagnetic?, *Physics Essays*, *18*(4), arXiv:physics/0510139v2 [physics.plasm-ph].
Escoubet, C. P., M. Fehringer, and M. Goldstein (2001), The Cluster mission, *Ann. Geophys.*, *19*, 1197.
Evans, D. S., and M. S. Greer (2000), *NOAA Technical Memorandum OAR SEC-93*, Boulder, Colo.
Fang, X., M. W. Liemohn, J. U. Kozyra, D. S. Evans, A. D. DeJong, and B. A. Emery (2007), Global 30–240 keV proton precipitation in the 17–18 April 2002 geomagnetic storms: 1. Patterns, *J. Geophys. Res.*, *112*, A05301, doi:10.1029/2006JA011867.
Fejer, B. G., and J. T. Emmert (2003), Low-latitude ionospheric disturbance electric field effects during the recovery phase of the 19–21 October 1998 magnetic storm, *J. Geophys. Res.*, *108*(A12), 1240, doi:10.1029/2001JA000188.
Fejer, B. G., and L. Scherliess (1995), Time dependent response of equatorial ionospheric electric fields to magnetospheric disturbances, *Geophys. Res. Lett.*, *22*, 851–854, doi:10.1029/95GL00390.

Fejer, B. G., and L. Scherliess (1997), Empirical models of storm time equatorial zonal electric fields, *J. Geophys. Res.*, *102*(A11), 24,047–24,056, doi:10.1029/97JA02164.
Fejer, B. G., R. W. Spiro, R. A. Wolf, and J. C. Foster (1990), Latitudinal variation of perturbation electric fields during magnetically disturbed periods: 1986 SUNDIAL observations and model results, *Ann. Geophys.*, *8*(6), 441–454.
Foster, J. C., and H. B. Vo (2002), Average characteristics and activity dependence of the subauroral polarization stream, *J. Geophys. Res.*, *107*(A12), 1475, doi:10.1029/2002JA009409.
Foullon, C., et al. (2007), Multi-spacecraft study of the 21 January 2005 ICME: Evidence of current sheet substructure near the periphery of a strongly expanding fast magnetic cloud, *Solar Phys.*, *244*, 139–165.
Fujimoto, M., T. Mukai, A. Matsuoka, Y. Saito, H. Hayakawa, S. Kokubun, and R. P. Lepping (2000), Multi-point observations of cold-dense plasma sheet and its relation with tail-LLBL, *Adv. Space Res.*, *25*(7/8), 1607–1616.
Fujimoto, M., T. Mukai, and S. Kokubun (2002), Cold-dense plasma sheet and hot-dense ions in the inner magnetosphere, *Adv. Space Res.*, *30*(10), 2279–2288.
Fujimoto, M., T. Mukai, and S. Kokubun (2005), The structure of the plasma sheet under northward IMF, in *Frontiers in Magnetospheric Plasma Physics – Celebrating 10 Years of Geotail Operation*, *COSPAR Colloquia Series*, vol. 16, pp. 19–27, Elsevier Ltd., London, U. K.
Fuller-Rowell, T. J., and D. S. Evans (1987), Height-integrated Pedersen and Hall conductivity patterns inferred from the TIROS-NOAA satellite data, *J. Geophys. Res.*, *92*(A7), 7606–7618, doi:10.1029/JA092iA07p07606.
Fuller-Rowell, T. J., G. H. Millward, A. D. Richmond, and M. V. Codrescu (2002), Storm-time changes in the upper atmosphere at low latitudes, *J. Atmos. Sol. Terr. Phys.*, *64*, 1383–1391.
Garner, T. W., R. A. Wolf, R. W. Spiro, W. J. Burke, B. G. Fejer, S. Sazykin, J. L. Roeder, and M. R. Hairston (2004), Magnetospheric electric fields and plasma sheet injection to low L-shells during the 4–5 June 1991 magnetic storm: Comparison between the Rice Convection Model and observations, *J. Geophys. Res.*, *109*, A02214, doi:10.1029/2003JA010208.
Gary, J. B., R. A. Heelis, and J. P. Thayer (1995), Summary of field aligned Poynting flux observations from DE2, *Geophys. Res. Lett.*, *22*(14), 1861–1864, doi:10.1029/95GL00570.
Gloeckler, G., et al. (1998), Investigation of the composition of solar and interstellar matter using solar wind and pickup ion measurements with SWICS and SWIMS on the ACE spacecraft, *Space Sci. Rev.*, *86*, 497.
Goldstein, J., B. R. Sandel, M. F. Thonsen, M. Spasojevic, and P. H. Reiff (2004), Simultaneous remote sensing and in situ observations of plasmaspheric drainage plumes, *J. Geophys. Res.*, *109*, A03202, doi:10.1029/2003JA010281.
Gombosi, T. I., G. Tóth, D. L. De Zeeuw, K. C. Hansen, K. Kabin, and K. G. Powell (2002), Semirelativistic magnetohydrodynamics and physics based convergence acceleration, *J. Comput. Phys.*, *177*, 176–205.
Gonzalez, W. D., and E. Echer (2005), A study on the peak *Dst* and peak negative B_z relationship during intense geomagnetic storms, *Geophys. Res. Lett.*, *32*, L18103, doi:10.1029/2005GL023486.
Gonzalez, W. D., et al. (1994), What is a geomagnetic storm?, *J. Geophys. Res.*, *99*(A4), 5771–5792, doi:10.1029/93JA02867.
Greenspan, M. E., C. E. Rasmussen, W. J. Burke, and M. A. Abdu (1991), Equatorial density depletions observed at 840 km during the Great Magnetic Storm of March 1989, *J. Geophys. Res.*, *96*, 13,931–13,942, doi:10.1029/91JA01264.
Hagan, M. E., and J. M. Forbes (2002), Migrating and nonmigrating diurnal tides in the middle and upper atmosphere excited by tropospheric latent heat release, *J. Geophys. Res.*, *107*(D24), 4754, doi:10.1029/2001JD001236.
Hagan, M. E., and J. M. Forbes (2003), Migrating and nonmigrating semidiurnal tides in the upper atmosphere excited by tropospheric latent heat release, *J. Geophys. Res.*, *108*(A2), 1062, doi:10.1029/2002JA009466.
Hairston, M. R., R. A. Heelis, and F. J. Rich (1998), Analysis of the ionospheric cross polar cap potential drop using DMSP data during the National Space Weather Program study period, *J. Geophys. Res.*, *103*(A11), 26,337–26,347, doi:10.1029/97JA03241.
Hardy, D. A., L. K. Schmidt, M. S. Gussenhoven, F. J. Marshall, H. C. Yeh, T. L. Shumaker, A. Huber, and J. Pantazis (1984), Precipitating electron and ion detectors (SSJ/4) for block 5D/Flights 4–10 DMSP satellites: Calibration and data presentation, Tech. Rep., AFGL-TR-84-0317, Air Force Geophys. Lab., Hanscom Air Force Base, Mass.
Hasegawa, H., M. Fujimoto, Y. Saito, and T. Mukai (2004), Dense and stagnant ions in the low-latitude boundary region under northward interplanetary magnetic field, *Geophys. Res. Lett.*, *31*, L06802, doi:10.1029/2003GL019120.
Hedin, A. E., N. W. Spencer, H. G. Mayr, and H. S. Porter (1981), Semiempirical modeling of thermospheric magnetic storms, *J. Geophys. Res.*, *86*(A5), 3515–3518, doi:10.1029/JA086iA05p03515.
Huang, C.-S., J. C. Foster, and M. C. Kelley (2005a), Long-duration penetration of the interplanetary electric field to the low latitude ionosphere during the main phase of magnetic storms, *J. Geophys. Res.*, *110*, A11309, doi:10.1029/2005JA011202.
Huang, C. Y., W. J. Burke, and C. S. Lin (2005b), Ion precipitation in the dawn sector during geomagnetic storms, *J. Geophys. Res.*, *110*, A11213, doi:10.1029/2005JA011116.
Huang, C.-S., F. J. Rich, and W. J. Burke (2010), Storm time electric fields in the equatorial ionosphere observed near the dusk meridian, *J. Geophys. Res.*, *115*, A08313, doi:10.1029/2009JA015150.
Hudson, M. K., S. R. Elkington, J. G. Lyon, and C. C. Goodrich (2000), Increase in relativistic electron flux in the inner magnetosphere: ULF wave mode structure, *Adv. Space Res.*, *25*, 2327–2337.
Imber, S. M., S. E. Milan, and B. Hubert (2006), The auroral and ionospheric flow signatures of dual lobe reconnection, *Ann. Geophys.*, *24*, 3115–3129.
Iyemori, T. (1990), Storm-time magnetospheric currents inferred from mid-latitude geomagnetic field variations, *J. Geomagn. Geoelectr.*, *42*, 1249–1265.
Jaggi, R. K., and R. A. Wolf (1973), Self-consistent calculation of the motion of a sheet of ions in the magnetosphere, *J. Geophys. Res.*, *78*(16), 2852–2866, doi:10.1029/JA078i016p02852.
Janhunen, P., and M. Palmroth (2001), Some observational phenomena are well reproduced by our global MHD while others are not: Remarks on what, why, and how, *Adv. Space Res.*, *28*(12), 1685–1691.
Kamide, Y., and S.-I. Akasofu (1983), Notes on the auroral electrojet indices, *Rev. Geophys. Space Phys.*, *27*(7), 1647–1656.
Kamide, Y., and G. Rostoker (2004), What is the physical meaning of the *AE* index?, *Eos Trans. AGU*, *85*(19), 188–192, doi:10.1029/2004EO190010.
Katus, R. M., and M. W. Liemohn (2013), Similarities and differences in low- to middle-latitude geomagnetic indices, *J. Geophys. Res. Space Physics*, *118*, 5149–5156, doi:10.1002/jgra.50501.
Kelley, M. C., B. G. Fejer, and C. A. Gonzales (1979), An explanation for anomalous ionospheric electric fields associated with a northward turning of the interplanetary magnetic field, *Geophys. Res. Lett.*, *6*(4), 301–304, doi:10.1029/GL006i004p00301.
Knipp, D., S. Eriksson, L. Kilcommons, G. Crowley, J. Lei, M. Hairston, and K. Drake (2011), Extreme Poynting flux in the dayside thermosphere: Examples and statistics, *Geophys. Res. Lett.*, *38*, L16102, doi:10.1029/2011GL048302.
Kokorowski, M., et al. (2008), Magnetospheric electric field variations caused by storm-time shock fronts, *Adv. Space Res.*, *42*, 181–191.

Kozyra, J. U., M.-C. Fok, E. R. Sanchez, D. S. Evans, D. C. Hamilton, and A. F. Nagy (1998), The role of precipitation losses in producing the rapid early recovery phase of the great magnetic storm of February 1986, *J. Geophys. Res.*, *103*(A4), 6801–6814, doi:10.1029/97JA03330.

Kozyra, J. U., et al. (2004), Coupling processes in the inner magnetosphere associated with midlatitude red auroras during superstorms, *Eos Trans. AGU*, 85(47), Fall Meet. Suppl., Abstract SM12B-03.

Kozyra, J. U., W. B. Manchester IV, C. P. Escoubet, S. T. Lepri, M. W. Liemohn, W. D. Gonzalez, M. W. Thomsen, and B. T. Tsurutani (2013), Earth's collision with a solar filament on 21 January 2005: Overview, *J. Geophys. Res. Space Physics*, *118*, 5967–5978, doi:10.1002/jgra.50567.

Langel, R. A., and R. H. Estes (1985), Large-scale, near-field magnetic fields from external sources and the corresponding induced internal field, *J. Geophys. Res.*, *90*, 2487–2494, doi:10.1029/JB090iB03p02487.

Laundal, K. M., and N. Østgaard (2008), Persistent global proton aurora caused by high solar wind dynamic pressure, *J. Geophys. Res.*, *113*, A08231, doi:10.1029/2008JA013147.

Lavraud, B., et al. (2005), Characteristics of the magnetosheath electron boundary layer under northward IMF: Implications for high-latitude reconnection, *J. Geophys. Res.*, *110*, A06209, doi:10.1029/2004JA010808.

Lavraud, B., M. F. Thomsen, B. Lefebvre, S. J. Schwartz, K. Seki, T. D. Phan, Y. L. Wang, A. Fazakerley, H. Re'me, and A. Balogh (2006), Evidence for newly closed magnetosheath field lines at the dayside magnetopause under northward IMF, *J. Geophys. Res.*, *111*, A05211, doi:10.1029/2005JA011266.

Lemaire, J. F. (2000), The formation plasmaspheric plumes, *Phys. Chem. Earth, Part C*, *25*, 9–17.

Li, W., J. Raeder, J. Dorelli, M. Øieroset, and T. D. Phan (2005), Plasma sheet formation during long period of northward IMF, *Geophys. Res. Lett.*, *32*, L12S08, doi:10.1029/2004GL021524.

Li, W., J. Raeder, M. F. Thomsen, and B. Lavraud (2008), Solar wind plasma entry into the magnetosphere under northward IMF conditions, *J. Geophys. Res.*, *113*, A04204, doi:10.1029/2007JA012604.

Li, W., D. Knipp, J. Lei, and J. Raeder (2011), The relation between dayside local Poynting flux enhancement and cusp reconnection, *J. Geophys. Res.*, *116*, A08301, doi:10.1029/2011JA016566.

Li, X., et al. (2006), Modeling of 1–2 September 1859 super magnetic storm, *Adv. Space Res.*, *38*, 273–279.

Liemohn, M. W., J.-C. Zhang, M. F. Thomsen, J. E. Borovsky, J. U. Kozyra, and R. Ilie (2008), Plasma properties of superstorms at geosynchronous orbit: How different are they?, *Geophys. Res. Lett.*, *35*, L06S06, doi:10.1029/2005JA011202.

Liou, K., P. T. Newell, J.-H. Shue, C.-I. Meng, Y. Miyashita, H. Kojima, and H. Matsumoto (2007), "Compression aurora": Particle precipitation driven by long-duration high solar wind ram pressure, *J. Geophys. Res.*, *112*, A11216, doi:10.1029/2007JA012443.

Liu, H., H. Lühr, V. Henize, and W. Köhler (2005a), Global distribution of the thermospheric total mass density derived from CHAMP, *J. Geophys. Res.*, *110*, A04301, doi:10.1029/2004JA010741.

Liu, R., S.-Y. Ma, and H. Lühr (2011), Predicting storm-time thermospheric mass density variations at CHAMP and GRACE altitudes, *Ann. Geophys.*, *29*, 443–453.

Liu, Z. X., C. P. Escoubet, Z. Pu, H. Laakso, J. K. Shi, C. Shen, and M. Hapgood (2005b), The Double Star mission, *Ann. Geophys.*, *23*, 2707–2712.

Lu, G., A. D. Richmond, B. A. Emery, and R. G. Roble (1995), Magnetosphere-ionosphere-thermosphere coupling: Effect of neutral winds on Joule heating and field-aligned current, *J. Geophys. Res.*, *100*(A10), 19,643–19,659, doi:10.1029/95JA00766.

Lu, G., et al. (1996), High-latitude ionospheric electrodynamics as determined by the AMIE procedure for the conjunctive SUNDIAL/ATLAS-1/GEM period of March 28–29, 1992, *J. Geophys. Res.*, *101*(A12), 26,697–26,718, doi:10.1029/96JA00513.

Lu, G., L. Goncharenko, M. J. Nicolls, A. Maute, A. Coster, and L. J. Paxton (2012), Ionospheric and thermospheric variations associated with prompt penetration electric fields, *J. Geophys. Res.*, *117*, A08312, doi:10.1029/2012JA017769.

Lu, G., J. D. Huba, and C. Valladares (2013), Modeling ionospheric super-fountain effect based on the coupled TIMEGCM-SAMI3, *J. Geophys. Res. Space Physics*, *118*, 2527–2535, doi:10.1002/jgra.50256.

Lühr, H., et al. (1986a), In situ magnetic field measurements during AMPTE solar wind Li^+ releases, *J. Geophys. Res.*, *91*(A2), 1261–1270, doi:10.1029/JA091iA02p01261.

Lühr, H., D. Southwood, N. Klocker, M. Dunlop, W. Mier-Jedrzejowicz, R. Rijnbeek, M. Six, B. Häusler, and M. Acuna (1986b), In-situ magnetic field observations of AMPTE's artificial comet, *Nature*, *320*, 708–711.

Lühr, H., M. Rother, S. Maus, W. Mai, and D. Cooke (2003), The diamagnetic effect of the equatorial Appleton anomaly: Its characteristics and impact on geomagnetic field modeling, *Geophys. Res. Lett.*, *30*(17), 1906, doi:10.1029/2003GL017407.

Lühr, H., M. Rother, W. Köhler, P. Ritter, and L. Grunwaldt (2004), Thermospheric up-welling in the cusp region: Evidence from CHAMP observations, *Geophys. Res. Lett.*, *31*, L06805, doi:10.1029/2003GL019314.

Mac-Mahon, R. M., and W. D. Gonzalez (1997), Energetics during the main phase of geomagnetic superstorms, *J. Geophys. Res.*, *102*(A7), 14,199–14,207, doi:10.1029/97JA01151.

Manchester, W. B., IV, et al. (2006), Modeling the Sun-to-Earth propagation of a very fast CME, *Adv. Space Res.*, *38*, 253–262.

Manchester, W. B., IV, J. U. Kozyra, S. T. Lepri, and B. Lavraud (2014), Simulation of magnetic cloud erosion during propagation, *J. Geophys. Res. Space Physics*, doi:10.1002/2014JA019882, in press.

Mannucci, A., B. Wilson, D. Yuan, C. Ho, U. Lindqwister, and T. Runge (1998), A global mapping technique for GPS-derived ionospheric total electron content measurements, *Radio Sci.*, *33*, 565–582, doi:10.1029/97RS02707.

Mannucci, A. J., B. Iijima, L. Sparks, X. Q. Pi, B. Wilson, and U. Lindqwister (1999), Assessment of global TEC mapping using a three-dimensional electron density model, *J. Atmos. Sol. Terr. Phys.*, *61*, 1227–1236, doi:10.1016/S1364-6826(99)00053-X.

Mannucci, A. J., B. T. Tsurutani, B. A. Iijima, A. Komjathy, A. Saito, W. D. Gonzalez, F. L. Guarnieri, J. U. Kozyra, and R. Skoug (2005), Dayside global ionospheric response to the major interplanetary events of October 29–30, 2003 Halloween Storms, *Geophys. Res. Lett.*, *32*, L12S02, doi:10.1029/2004GL021467.

Maruyama, N., et al. (2007), Modeling storm-time electrodynamics of the low-latitude ionosphere-thermosphere system: Can long lasting disturbance electric fields be accounted for?, *J. Atmos. Sol. Terr. Phys.*, *69*, 1182–1199.

McPherron, R. L. (1997), The role of substorms in the generation of magnetic storms, in *Magnetic Storms*, *Geophys. Monogr. Ser.*, vol. 98, edited by B. T. Tsurutani et al., p. 131, AGU, Washington, D. C.

Mende, S. B., et al. (2000), Far ultraviolet imaging from the IMAGE spacecraft, 3, Spectral imaging of Lyman alpha and OI 135.6 nm, *Space Sci. Rev.*, *91*, 287–318.

Mitchell, D. G., et al. (2000), High Energy Neutral Atom (HEN A) Imager for the IM AGE Mission, *Space Sci. Rev.*, *91*, 67–112.

Miyashita, Y., et al. (2005), Geotail observations of signatures in the near-Earth magnetotail for the extremely intense substorms of the 30 October 2003 storm, *J. Geophys. Res.*, *110*, A09S25, doi:10.1029/2005JA011070.

Munoz, P. R., A. C.-L. Chian, R. A. Miranda, and M. Yamada (2010), in *Solar and Stellar Variability: Impact on Earth and Planets*, *Proc. IAU Symp. No. 264*, edited by A. G. Kosovichev, A. H. Andrei, and J.-P. Rozelot, pp. 369–372, International Astronomical Union, Cambridge Univ. Press, Cambridge, U. K.

Newell, P. T., and C.-I. Meng (1994), Ionospheric projections of magnetospheric regions under low and high solar wind pressure conditions, *J. Geophys. Res.*, *99*(A1), 273–286, doi:10.1029/93JA02273.
Newell, P. T., et al. (1998), Characterizing the state of the magnetosphere: Testing the ion precipitation maxima latitude (b2i) and the ion isotropy boundary, *J. Geophys. Res.*, *103*, 4739–4745, doi:10.1029/97JA03622.
Ni, B., R. M. Thorne, Y. Y. Shprits, K. G. Orlova, and N. P. Meredith (2011), Chorus-driven resonant scattering of diffuse auroral electrons in nondipolar magnetic fields, *J. Geophys. Res.*, *116*, A06225, doi:10.1029/2011JA016453.
Nishino, M., T. Terasawa, and M. Hoshino (2002), Increase of the tail plasma content during the northward interplanetary magnetic field intervals: Case studies, *J. Geophys. Res.*, *107*, doi:10.1029/2002JA0009268.
O'Brien, T. P., and R. L. McPherron (2000), Evidence against an independent solar wind density driver of the terrestrial ring current, *Geophys. Res. Lett.*, *27*(23), 3797–3799, doi:10.1029/2000GL012125.
Øieroset, M., J. Raeder, T. D. Phan, S. Wing, J. P. McFadden, W. Li, M. Fujimoto, H. Re`me, and A. Balogh (2005), Global cooling and densification of the plasma sheet during an extended period of purely northward IMF on October 22–24, 2003, *Geophys. Res. Lett.*, *32*, L12S07, doi:10.1029/2004GL021523.
Øieroset, M., T. D. Phan, V. Angelopoulos, J. P. Eastwood, J. McFadden, D. Larson, C. W. Carlson, K.-H. Glassmeier, M. Fujimoto, and J. Raeder (2008), THEMIS multi-spacecraft observations of magnetosheath plasma penetration deep into the dayside low latitude magnetosphere for northward and strong B_y IMF, *Geophys. Res. Lett.*, *35*, L17S11, doi:10.1029/2008GL033661.
Palmroth, M., T. V. Laitinen, and T. I. Pulkkinen (2006), Magnetopause energy and mass transfer: Results from a global MHD simulation, *Ann. Geophys.*, *24*, 3467.
Park, K. S., T. Ogino, and R. J. Walker (2006), On the importance of antiparallel reconnection when the dipole tilt and IMF B_y are nonzero, *J. Geophys. Res.*, *111*, A05202, doi:10.1029/2004JA010972.
Parrot, M., A. Buzzi, O. Santolík, J. J. Berthelier, J. A. Sauvaud, and J. P. Lebreton (2006), New observations of electromagnetic harmonic ELF emissions in the ionosphere by the DEMETER satellite during large magnetic storms, *J. Geophys. Res.*, *111*, A08301, doi:10.1029/2005JA011583.
Paxton, L. J., et al. (1999), Global ultraviolet imager (GUVI): Measuring composition and energy inputs for the NASA Thermosphere Ionosphere Mesosphere Energetics and Dynamics (TIMED) mission, *Proc. SPIE Int. Soc. Opt. Eng.*, *3756*, 256–276.
Paxton, L. J., et al. (2004), GUVI: A hyperspectral imager for geospace, in *Instruments, Science, and Methods for Geospace and Planetary Remote Sensing, Proc. SPIE*, vol. 5660, edited by C. A. Nardell et al., pp. 228–240, doi:10.1117/12.579171.
Paznukhov, V. V., B. W. Reinisch, P. Song, X. Huang, T. W. Bullett, and O. Veliz (2007), Formation of an F3 layer in the equatorial ionosphere: A result from strong IMF changes, *J. Atmos. Sol. Terr. Phys.*, *69*, 1292–1304.
Peterson, T. C., P. A. Stott, and S. Herring (Eds.) (2012), Explaining extreme events of 2011 from a climate perspective, *Bull. Am. Meteorol. Soc.*, *93*, 1041–1067.
Peterson, T. C., M. P. Hoerling, P. A. Stott, and S. Herring (Eds.) (2013), Explaining extreme events of 2012 from a climate perspective, *Bull. Am. Meteorol. Soc.*, *94*(9), S1–S74.
Phan, T. D., R. P. Lin, S. A. Fuselier, and M. Fujimoto (2000), Wind observations of mixed magnetosheath-plasma sheet ions deep inside the magnetosphere, *J. Geophys. Res.*, *105*, 5497–5505, doi:10.1029/1999JA900455.
Pohjolainen, S., et al. (2007), *Solar Phys.*, *244*, 167–188.
Potapov, A. S., and T. N. Polyushkina (2010), Experimental evidence for direct penetration of ULF waves from the solar wind and their possible effect on acceleration of radiation belt electrons, *Geomagn. Aeron.*, *50*(8), 950–957.
Powell, K., P. Roe, T. Linde, T. Gombosi, and D. D. Zeeuw (1999), A solution-adaptive upwind scheme for ideal magnetohydrodynamics, *J. Comput. Phys.*, *154*, 284–309.
Rae, I. J., et al. (2010), Comparison of the open-closed separatrix in a global magnetospheric simulation with observations: The role of the ring current, *J. Geophys. Res.*, *115*, A08216, doi:10.1029/2009JA015068.
Raeder, J., R. J. Walker, and M. Ashour-Abdalla (1995), The structure of the distant geomagnetic tail during long periods of northward IMF, *Geophys. Res. Lett.*, *22*(4), 349–352, doi:10.1029/94GL03380.
Raeder, J., J. Berchem, M. Ashour-Abdalla, L. A. Frank, W. R. Paterson, K. L. Ackerson, R. P. Lepping, S. Kokubun, T. Yamamoto, and S. A. Slavin (1997), Boundary layer formation in the magnetotail: Geotail observations and comparisons with a global MHD model, *Geophys. Res. Lett.*, *24*, 951–954, doi:10.1029/97GL00218.
Reiff, P. R., and J. L. Burch (1985), IMF By-dependent plasma flow and Birkeland currents in the dayside magnetosphere, 2. A global model for northward and southward IMF, *J. Geophys. Res.*, *90*(A2), 1595–1609.
Reme, H., et al. (2005), The HIA instrument on board the Tan Ce 1 Double Star near-equatorial spacecraft and its first results, *Ann. Geophys.*, *23*, 2757–2774.
Rentz, S., and H. Lühr (2008), Climatology of the cusp-related thermospheric mass density anomaly, as derived from CHAMP observations, *Ann. Geophys.*, *26*, 2807–2823.
Rich, F. J., and M. Hairston (1994), Large-scale convection patterns observed by DMSP, *J. Geophys. Res.*, *79*, 3827–3844, doi:10.1029/93JA03296.
Richmond, A. D., and Y. Kamide (1988), Mapping electrodynamic features of the high-latitude ionosphere from localized observations: Technique, *J. Geophys. Res.*, *93*, 5741–5759, doi:10.1029/JA093iA06p05741.
Ridley, A. J., and M. W. Liemohn (2002), A model-derived storm time asymmetric ring current driven electric field description, *J. Geophys. Res.*, *107*(A8), 1151, doi:10.1029/2001JA000051.
Ridley, A. J., T. I. Gombosi, and D. L. DeZeeuw (2004), Ionospheric control of the magnetosphere: Conductance, *Ann. Geophys.*, *22*, 567–584.
Roble, R. G. (1995), Energetics of the mesosphere and thermosphere, in *The Upper Mesosphere and Lower Thermosphere: A Review of Experiment and Theory, Geophys. Monogr. Ser.*, vol. 87, pp. 1–21, AGU, Washington, D. C.
Roble, R. G., and E. C. Ridley (1994), A thermosphere-ionosphere-mesosphere electrodynamics general circulation model (time-GCM): Equinox solar cycle minimum simulations (30–500 km), *Geophys. Res. Lett.*, *21*, 417–420, doi:10.1029/93GL03391.
Rosenqvist, L., H. Opgenoorth, S. Buchert, I. McCrea, O. Amm, and C. Lathuillere (2005), Extreme solar-terrestrial events of October 2003: High-latitude and Cluster observations of the large geomagnetic disturbances on 30 October, *J. Geophys. Res.*, *110*, A09S23, doi:10.1029/2004JA010927.
Rother, M., K. Schlegel, and H. Lühr (2007), CHAMP observation of intense kilometer-scale field-aligned currents, evidence for an ionospheric Alfven resonator, *Ann. Geophys.*, *25*, 1603–1615.
Russell, C. T., and R. L. McPherron (1973), Semiannual variation of geomagnetic activity, *J. Geophys. Res.*, *78*(1), 92–108, doi:10.1029/JA078i001p00092.
Sadler, F. B., M. Lessard, E. Lund, A. Otto, and H. Lühr (2012), Auroral precipitation/ion upwelling as a driver of neutral density enhancement in the cusp, *J. Atmos. Sol. Terr. Phys.*, *87–88*, 82–90.
Sahai, Y., et al. (2011), Studies of ionospheric F-region response in the Latin American sector during the geomagnetic storm of 21–22 January 2005, *Ann. Geophys.*, *29*, 919–929.

Santos, A. M., M. A. Abdu, J. H. A. Sobral, D. Koga, P. A. B. Nogueira, and C. M. N. Candido (2012), Strong longitudinal difference in ionospheric responses over Fortaleza (Brazil) and Jicamarca (Peru) during the January 2005 magnetic storm, dominated by northward IMF, *J. Geophys. Res.*, *117*, A08333, doi:10.1029/2012JA017604.

Sauvaud, J.-A., P. Koperski, T. Beutier, H. Barthe, C. Aoustin, J. J. Thocaven, J. Rouzaud, E. Penou, O. Vaisberg, and N. Borodkova (1997), The INTERBALL-Tail electron experiment: Initial results on the low-latitude boundary layer of the dawn magnetosphere, *Ann. Geophys.*, *15*, 587–595.

Sazykin, S. (2000), Theoretical studies of penetration of magnetospheric electric fields to the ionosphere, PhD thesis, Utah State Univ., Logan, Utah.

Scherliess, L., and B. G. Fejer (1997), Storm time dependence of equatorial disturbance dynamo zonal electric fields, *J. Geophys. Res.*, *102*(A11), 24,037–24,046, doi:10.1029/97JA02165.

Schlegel, K., H. Lühr, J.-P. St.-Maurice, G. Crowley, and C. Hackert (2005), Thermospheric density structures over the polar regions observed with CHAMP, *Ann. Geophys.*, *23*, 1659–1672.

Schulz, M., and L. J. Lanzerotti (1974), *Particle Diffusion in the Radiation Belts*, Springer, New York.

Sckopke, N. (1966), A general relation between the energy of trapped particles and the disturbance field near the Earth, *J. Geophys. Res.*, *71*(13), 3125–3130, doi:10.1029/JZ071i013p03125.

Sergeev, V. A., and M. V. Malkov (1988), Diagnostics of the magnetic configuration of the plasma layer from measurements of energetic electrons above the ionosphere, *Geomagn. Aeron.*, *28*, 549.

Sergeev, V. A., E. M. Sazhina, N. A. Tsyganenko, J. A. Lundblad, and F. Søraas (1983), Pitch-angle scattering of energetic protons in the magnetotail current sheet as the dominant source of their isotropic precipitation into the nightside ionosphere, *Planet. Space Sci.*, *31*, 1147–1155, doi:10.1016/0032-0633(83)90103-4.

Sergeev, V. A., M. V. Malkov, and K. Mursula (1993), Testing of the isotropic boundary algorithm method to evaluate the magnetic field configuration in the tail, *J. Geophys. Res.*, *98*, 7609–7620, doi:10.1029/92JA02587.

Sergeev, V. A., G. R. Bikkuzina, and P. T. Newell (1997), Dayside isotropic precipitation of energetic protons, *Ann. Geophys.*, *15*, 1233–1245.

Smith, J. P., M. F. Thomsen, J. E. Borovsky, and M. Collier (1999), Solar wind density as a driver for the ring current in mild storms, *Geophys. Res. Lett.*, *26*(13), 1797–1800, doi:10.1029/1999GL900341.

Song, P., and C. T. Russell (1992), Model of formation of the low-latitude boundary layer for strongly northward interplanetary magnetic field, *J. Geophys. Res.*, *97*, 1411–1420, doi:10.1029/91JA02377.

Søraas, F., and M. Sørbø (2013), Low altitude observations of ENA from the ring current and from the proton oval, *J. Atmos. Sol. Terr. Phys.*, *99*, 104–110, doi:10.1016/j.jastp.2012.10.003.

Søraas, F., K. Aarsnes, K. Oksavik, and D. S. Evans (2002), Ring current intensity estimated from low-altitude proton observations, *J. Geophys. Res.*, *107*(A7), 1149, doi:10.1029/2001JA000123.

Søraas, F., K. Oksavik, K. Aarsnes, D. S. Evans, and M. S. Greer (2003), Stormtime equatorial belt—An "image" of ring current behaviour, *Geophys. Res. Lett.*, *30*(2), 1052, doi:10.1029/2002GL015636.

Spiro, R. W., R. A. Wolf, and B. G. Fejer (1988), Penetration of high-latitude electric-field effects to low latitudes during SUNDIAL 1984, *Ann. Geophys.*, *6*(1), 39–50.

Stone, E. C., A. M. Frandsen, R. A. Mewaldt, E. R. Christian, D. Margolies, J. F. Omes, and F. Snow (1998), The Advanced Composition Explorer, *Space Sci. Rev.*, *86*, 1.

Sutton, E. K., J. M. Forbes, and D. J. Knipp (2009), Rapid response of the thermosphere to variations in Joule heating, *J. Geophys. Res.*, *114*, A04319, doi:10.1029/2008JA013667.

Terasawa, T., et al. (1997), Solar wind control of density and temperature in the near-Earth plasma sheet: WIND/GEOTAIL collaboration, *Geophys. Res., Lett.*, *24*(8), 935–938, doi:10.1029/96GL04018.

Thomsen, M. F., S. J. Bame, D. J. McComas, M. B. Moldwin, and K. R. Moore (1994), The magnetospheric lobe at geosynchronous orbit, *J. Geophys. Res.*, *99*(A9), 17,283–17,293, doi:10.1029/94JA00423.

Thomsen, M. F., E. Noveroske, J. E. Borovsky, and D. J. McComas (1997), Calculation of moments from measurements by the Los Alamos Magnetospheric Plasma Analyzer, Rep. LA-13,566-MS, Los Alamos Natl. Lab., Los Alamos, N. M.

Thomsen, M. F., J. E. Borovsky, R. M. Skoug, and C. W. Smith (2003), Delivery of cold, dense plasma sheet material into the near-Earth region, *J. Geophys. Res.*, *108*(A4), 1151, doi:10.1029/2002JA009544.

Toffoletto, F. R., S. Sazykin, R. W. Spiro, and R. A. Wolf (2003), Modeling the inner magnetosphere using the Rice Convection Model (review), *Space Sci. Rev.*, *107*, 175–196.

Tóth, G., et al. (2005), Space Weather Modeling Framework: A new tool for the space science community, *J. Geophys. Res.*, *110*, A12226., doi:10.1029/2005JA011126.

Tóth, G., et al. (2012), Adaptive numerical algorithms in space weather modeling, *J. Comput. Phys.*, *231*, 870–903.

Tsurutani, B. T., and R. P. Lin (1985), Acceleration of >47 keV ions and >2 keV electrons by interplanetary shocks at 1 AU, *J. Geophys. Res.*, *90*(A1), 1–11, doi:10.1029/JA090iA01p00001.

Tsurutani, B. T., W. D. Gonzalez, F. Tang, and Y. T. Lee (1992), Great magnetic storms, *Geophys. Res. Lett.*, *19*(73).

Tsurutani, B. T., W. D. Gonzalez, G. S. Lakhina, and S. Alex (2003), The extreme magnetic storm of 1–2 September 1859, *J. Geophys. Res.*, *108*(A7), 1268, doi:10.1029/2002JA009504.

Tsurutani, B., et al. (2004), Global dayside ionospheric uplift and enhancement associated with interplanetary electric fields, *J. Geophys. Res.*, *109*, A08302, doi:10.1029/2003JA010342.

Tsurutani, B. T., O. P. Verkhoglyadova, A. J. Mannucci, T. Araki, A. Sato, T. Tsuda, and K. Yumoto (2007), Oxygen ion uplift and satellite drag effects during the 30 October 2003 daytime superfountain event, *Ann. Geophys.*, *25*, 569–574.

Tsurutani, B. T., et al. (2008), Prompt penetration electric fields (PPEFs) and their ionospheric effects during the great magnetic storm of 30–31 October 2003, *J. Geophys. Res.*, *113*, A05311, doi:10.1029/2007JA012879.

Vaisbert, O. L., and G. N. Zastenker (1976), Solar wind and magnetosheath observations at Earth during August 1972, *Space Sci. Rev.*, *19*, 687–702.

Wanliss, J. A., and K. M. Showalter (2006), High-resolution global storm index: *Dst* versus *SYM-H*, *J. Geophys. Res.*, *111*, A02202, doi:10.1029/2005JA011034.

Weiss, L. A., M. F. Thomsen, G. D. Reeves, and D. J. McComas (1997), An examination of the Tsyganenko (T89a) field model using a database of two-satellite magnetic conjunctions, *J. Geophys. Res.*, *102*(A3), 4911–4918, doi:10.1029/96JA02876.

Welling, D. T., and A. J. Ridley (2010), Validation of SWMF magnetic field and plasma, *Space Weather*, *8*, S03002, doi:10.1029/2009SW000494.

Wolf, R. A. (1983), The quasi-static (slow-flow) region of the magnetosphere, in *Solar Terrestrial Physics*, edited by R. L. Carovillano and J. M. Forbes, pp. 303–368, Springer, New York.

Wolf, R. A., R. W. Spiro, S. Sazykin, and F. R. Toffoletto (2007), How the Earth's inner magnetosphere works: An evolving picture, *J. Atmos. Sol. Terr. Phys.*, *69*, 288–302.

Yamauchi, M., T. Iyemori, H. Frey, and M. Henderson (2006), Unusually quick development of a 4000 nT substorm during the initial 10 min of the 29 October 2003 magnetic storm, *J. Geophys. Res.*, *111*, A04217, doi:10.1029/2005JA011285.

Young, S. L., R. E. Denton, B. J. Anderson, and M. K. Hudson (2002), Empirical model for μ scattering caused by field line curvature in a realistic magnetosphere, *J. Geophys. Res.*, *107*(A6), 1069, doi:10.1029/2000JA000294.

Young, S. L., R. E. Denton, B. J. Anderson, and M. K. Hudson (2008), Magnetic field line curvature induced pitch angle diffusion in the inner magnetosphere, *J. Geophys. Res.*, *113*, A03210, doi:10.1029/2006JA012133.

Zhang, Y., L. J. Paxton, and Y. Zheng (2008), Interplanetary shock induced ring current auroras, *J. Geophys. Res.*, *113*, A01212, doi:10.1029/2007JA012554.

Zhou, X.-Y., and B. T. Tsurutani (1999), Rapid intensification and propagation of the dayside aurora: Large-scale interplanetary pressure pulses (fast shocks), *Geophys. Res. Lett.*, *26*, 1097–1100, doi:10.1029/1999GL900173.

Zhou, X.-Y., and B. T. Tsurutani (2003), Dawn and dusk auroras caused by gradual, intense solar wind ram pressure events, *J. Atmos. Sol. Terr. Phys.*, *66*, 153–160, doi:10.1016/j.jastp.2003.09.008.

Zhou, X.-Y., R. J. Strangeway, P. C. Anderson, D. G. Sibeck, B. T. Tsurutani, G. Haerendel, H. U. Frey, and J. K. Arballo (2003), Shock aurora: FAST and DMSP observations, *J. Geophys. Res.*, *108*(A4), 8019, doi:10.1029/2002JA009701.

Zong, Q.-G., B. W. Reinisch, P. Song, Y. Wei, and I. A. Galkin (2010), Dayside ionospheric response to the intense interplanetary shocks–solar wind discontinuities: Observations from the digisonde global ionospheric radio observatory, *J. Geophys. Res.*, *115*, A06304, doi:10.1029/2009JA014796.